El Cezeri
Journal of Science and Engineering
ISSN: 2148-3736

Research Article

Iterated Modified Tabu Search based Equitable Coloring for Scheduling Cricket World Cup Tournament

Venkatachalam M[1a], Praveena K[2b], Dafık Dafık[3c] Ismaıl Nacı Cangul[4d]
[1] PG and Research Department of Mathematics, Kongunadu Arts and Science College, Coimbatore, Tamil Nadu, India.
[2] Department of Computer Science, Dr. G. R. Damodaran College of Science, Coimbatore, Tamil Nadu, India.
[3] Combinatorics, Graph Theory and Network Topology (CGANT) Research Group, Department of Mathematics Education, University of Jember, Jember, Indonesia.
[4] Department of Mathematics, Faculty of Arts and Science, Bursa Uludag University, Gorukle 16059 Bursa/Turkey.

venkatmaths@kongunaducollege.ac.in

DOI : 10.31202/ecjse.1252238
Received: 17.02.2023 Accepted: 05.01.2024
How to cite this article:
Venkatachalam M, Praveena K, Dafık Dafık, Ismaıl Nacı Cangul, " Iterated Modified Tabu Search based Equitable Coloring for Scheduling Cricket World Cup Tournament", El-Cezeri Journal of Science and Engineering, Vol: 11, Iss:2, (2024), pp.(131-141).
ORCID: [a]0000-0001-5051-4104; [b]0000-0002-5527-7600. [c]0000-0003-0575-3039; [d]0000-0002-0700-5774

Abstract : In this article, an Iterated Modified Tabu Search (IMTS) approach is presented by improving certain aspects of general Tabu Search to enhance the approximation of the Equitable coloring problem (ECP) problem for a real-world problem of scheduling the ICC Cricket World Cup tournament. The proposed IMTS introduces new point generation mechanisms and parameter updating rules to achieve this objective of the tournament schedule. The IMTS algorithm defines different k-ECP instances and utilizes the search process to determine the optimal solution for an instance of k-ECP by estimating the minimum k-coloring value. An illustration of resolving the Cricket World Cup tournament scheduling problem using the proposed IMTS algorithm is provided. Also, an assessment of the IMTS is also performed on a commonly used benchmark instance. Both the results illustrate that the IMTS provided comparatively better solutions with high quality and computational efficiency.

Keywords : Computational Efficiency, Cricket World Cup, Equitable Coloring Problem, Iterated Modified Tabu Search, Scheduling Problem

1 Introduction

The Equitable Coloring Problem (ECP), a specialized variant of the general graph coloring problem, incorporates an essential equity constraint: the disparity in size between any two random color classes must not exceed one unit. Real-world problems like scheduling can be modelled as ECP for finding equitable chromatic number and resolved efficiently by avoiding incompatible allocation of tasks or timings. However, the additional condition of ECP makes it NP-hard problem and difficult to solve especially for problems with large-sized instances. Hence for solving the NP-complete problem and finding equitable chromatic number of large-sized graph, the heuristics and search algorithms have been introduced. Tabu Search algorithm emerges as a prominent choice, applied extensively for solving ECP to automatically compute the k-chromatic number. However, studies indicate that, the Tabu Search algorithm increases time complexity particularly when confronted for larger graphs.

Graphs are discrete structures containing vertices connected via edges which are employed in all domains as abstract models for analysis and illustration of real-world processes and problems [1], [2]. The relations between the entities in most domains like bonds between atoms and elements in chemistry, work scheduling, bonds in DNA, etc. are more effectively illustrated in the graphs [3]. This leads to active graph analysis tasks that can be formulated into problems and resolved using strategic techniques and algorithms. Among all the challenges, scheduling quandaries encompass a universal classification involving allocation predicaments, transcending domain boundaries and necessitating adept solutions. Graph coloring problem (GCP) [4] is one such method to formulate the scheduling problems based on graph theory. The fundamental aim of GCP lies in the allocation of colors to nodes within a graph, ensuring that neighboring nodes connected by an edge remain distinct in coloration. Programming system tasks and the arrangement of objects often exhibit seamless compatibility with the principles of the Graph Coloring Problem (GCP) [5]. Nonetheless, this approach encounters constraints when addressing specific scheduling complexities, such as the equitable distribution of workloads among workers or the appropriate allocation of time to clients. In these instances, the challenge lies in avoiding scenarios where a biased distribution emerges one worker burdened with an excessive workload while another is assigned significantly fewer tasks, owing to an uneven allocation strategy. To overcome these issues, the ECP [6] is formulated as a variant of GCP. An equitable k-coloring of an undirected graph are partitions of its nodes into k disjoint independent sets where the colors of two independent sets vary maximum by one. In simple terms, an equitable coloring with k colors is a conflict-free coloring with k colors, if it fulfills the equitable coloring conditions [7]. As a

variant of the GCP, the ECP apprehends defining a minimum k called as equitable chromatic number. Leveraging the framework of ECP, an abundance of challenges can be proficiently tackled using equitable scheduling strategies [8].

Round-robin sports tournament scheduling is one of the problems that can be resolved automatically using the ECP formulation. Round-robin sports timetables are pivotal in any multi-team tournament, including the World Cup Football tournaments and related domestic leagues, Olympic Games, Cricket World Cups and country-based cricket leagues especially the most popular Premier League Cricket tournaments and almost all multi-player and multi-team tournaments [9]. The round-robin scheduling includes n teams and constraint of all teams playing remaining teams precisely m times with a pre-determined number of rounds. Towards the end of the scheduled phases, the teams with higher points or most wins will advance to the next rounds. The two types of schedules in round robin are single round robins where two teams meet only once and double round robins where two teams meet twice before the end of the schedule. The major scheduling problem in these tournaments encompasses the traveling tournament problem and the availability of teams at specified times [10]. ECP conceptualizes round-robin scheduling as graph-based problems and tackles them using search-based algorithms.

However, ECP is a NP-complete problem (NP-hard and NP combined together) which renders its resolution more intricate. Many heuristic algorithms have been used to resolve ECP among which Tabu search is the most prevalent algorithm. In this paper, the ICC Cricket World Cup 2019 tournament scheduling problem is analysed and modeled as ECP. The Iterated Modified Tabu Search (IMTS) Algorithm is proposed, aiming to mitigate the time complexity associated with solving ECP. The proposed IMTS is an enhanced version of the Tabu search process whose new solution-generating process and updating of search parameters are improved to provide an efficient approximation. The subsequent sections are structured as follows: Section 2 provides a succinct overview of recent related research; Section 3 delineates the proposed approach for ECP resolution, while the Section 4 demonstrates its practical application in real-world scheduling scenarios. Section 5 presents the evaluation results, and finally, Section 6 encapsulates the conclusions drawn from the study.

2 Related Works

Due to its profound relevance across multiple studies, a multitude of research endeavours has been steadfastly directed towards the identification of efficient solutions for the ECP, with a parallel emphasis on their practical integration into real-world applications. Yan et al. [11] presented an innovative approach to equitable coloring of Cartesian products using balanced comprehensive manifold graphs. This approach utilizes the balancing factor to connect the graph based on the equity constraints of ECP. Bahiense et al. [12] offered a branch-and-cut approach for the ECP based on inter-programming representatives. This approach uses a primitive heuristic, splitting tactics and the first branch-and-cut strategy and enhances solutions for the ECP, exhibiting an improved average relative gap.

DSATUR, a pivotal graph colo‘ring algorithm devised by mathematician Daniel Brélaz and rooted in the principles of the greedy algorithm, stands as a cornerstone in this domain. Its extensive utilization for effectively addressing the challenges posed by the ECP underscores its significance. San Segundo [13] proposed a new DSATUR approach for precise vertex coloring problems by maximizing the saturation point to choose a new nominee vertex to color. Notably, it is one of the proficient solutions for any ECP approximation. Méndez-Díaz et al. [14] proposed a polyhedral approach associated with a 0,1-integer program design for ECP. Méndez-Díaz et al. [15] developed an exact DSatur-based algorithm with novel pruning procedures precisely developed from ECP constraints. Further expanding on this foundation, Méndez-Díaz et al. [16] also introduced an advanced pruning measure from equity constraints based on the popular DSATUR approach. This approach exploited arithmetical properties essential in equitable coloring and associated them with the methods of DSatur to provide an effective approximation. Though DSatur is widely recognized to provide better coloring than greedy algorithms, it falls short in comparison to the Recursive Largest First algorithm. This leads to the search for advanced DSatur and other algorithms for solving ECP.

Recent research has employed the heuristic algorithm for solving the NP-hard problem of the ECP. The profound and efficacious algorithm is the Tabu Search-based heuristic projected by Méndez-Díaz et al. [17] which uses a new local search criterion. This approach utilized the dynamic Tabu version of previous research to improve the ECP approximation. Wang et al. [18] proposed a hybrid Tabu search algorithm with feasible and infeasible searches for ECP. The process substitutes a possible local search where the search centers on the most applicable and practicable solutions and an infeasible local search where an organized exploration of solutions is acceptable by comforting the equity constraint. The hybrid Tabu search algorithm provided satisfactory performance on common benchmark instances.

Lai et al. [19] suggested a solution to the ECP using backtracking based iterated Tabu search in which the approximation of the ECP is performed with different fixed k values. The iterated Tabu search determines the k-coloring while the backtracking system adjusts k to an appropriate value and the binary search determines a good initial k value. The experimental analysis on common benchmark instances showed that this approach resulted in a better approximation of ECP than existing heuristic methods. Sun et al. [20] proposed a memetic search process that utilizes a backbone-based crossover operator, a 2-phase Tabu search strategy to resolve NP-hard ECP. Among the heuristic algorithms, the Tabu search based algorithms provide better colorings for ECP and also significantly reduce the complexity. However, as the scale of instances escalates to larger proportions,

these algorithms tend to exhibit heightened time complexities. Hence, this study acknowledges these challenges as focal research issues and introduces IMTS algorithm for overcoming those limitations in resolving the ECP effectively.

3 Iterated Modified Tabu Search Algorithm for the ECP

The proposed IMTS operates in a solution space where the equity conditions is fulfilled and only the conditions of graph coloring may be ignored. The k-ECP can be resolved by determining the solutions even after k+1 and continuing with k-1, k-2,... until the solution is found [21]. The iterative process of IMTS results to obtain optimal k-coloring with k∈ k*-1,k*-2,...,k*-m where k* has receiving the minimum number of equitable k* colors and m is a back tracking depth parameter such that m>1. The algorithm of the complete solution finding approach using IMTS is given as follows:

Algorithm 1 Proposed approach using IMTS algorithm for ECP

Require: Graph $G = (V, E)$, the number of colors k, the perturbation parameter β, the depth of tabu search α
Ensure: The best number of colors k^* and an equitable k^*-coloring solution s^*

k^r, s^r are initial k and s values determined by binary search (BS)
$(k^r, s^r) \leftarrow \mathrm{BS}(V, E, \alpha)$
Update best results $k^* \leftarrow k^r$, $k \leftarrow k^r$, $s^* \leftarrow s^r$
repeat
    if $k = k^* - 1$ or $k = 2$ **then**
        $k \leftarrow k^* - 1$
    else
        $k \leftarrow k - 1$
    end if
    Resolving equivalent k-ECP using IMTS, $s \leftarrow \mathrm{IMTS}(k, G, \alpha, \beta)$
    if $f(s) = 0$ **then**
        $k^* \leftarrow k$
        $s^* \leftarrow s$
    end if
until Time $T \geq T_{\max}$
return k^* and s^*

Algorithm 1 consists of three main processes: binary search to set an appropriate initial k value (k^r), backtracking mechanism to set k for IMTS and finally using IMTS for solving the k-ECP and updating k^*. The proposed IMTS approach for ECP terminates once the time reaches maximum limit even if the solution is not found. At this stage, the smallest number k^* obtained in the final step is considered as the approximate solution for the ECP.

For a given k-ECP, the IMTS initially searches the solution space where all possible k-classes assuring the equity constraint. Ω_k is the search space which is formulated as

$$\Omega_k = \{C : ||V_i| - |V_j|| \leq 1; i \neq j\} \tag{1}$$

where C is the k-classes denoted as $C = \{V_1, V_2, \cdots, V_k\}$ and $i \leq 1, j \leq k$ are the instances. The whole search space Ω is exploited by th e IMTS as given by

$$\Omega = \bigcup_{k=1}^{n} \Omega_k \tag{2}$$

In this equation, the k-classes of the search space guarantee the equity constraint but the coloring constraint is not guaranteed and might result in adjacent vertices getting the same color [22], [23]. Hence it becomes important to estimate the quality of the k-class solution candidate. For achieving this objective, the IMTS familiarizes an evaluation function $f\ (s))$ by totalling the sum of all conflicting edges in a k-class solution. Assigning $s = \{V_1, V_2, \cdots, V_k\}$ as the k-class equity in Ω, the evaluation function is given as.

$$f\ (s) = \Sigma_{V_i, V_j \in E} \delta\ (i, j) \tag{3}$$

where,

$$\delta\ (i, j) = \begin{cases} 1 & if\ E \in \{1, 2, \cdots, k\} \\ 0 & otherwise \end{cases} \tag{4}$$

The selected k-class solution is considered ideally equitable k-coloring satisfying both the equity and coloring constraints only when the $s \in \Omega$ and $f(s) = 0$. This solution is considered ideal since the search process of IMTS filters between the available k-class solutions by attaining the optimal solution with evaluation $f(s) = 0$, thus resulting in effecting transitioning of solutions for k-ECP.

3.1 IMTS procedure for *k*-ECP

The proposed IMTS procedure includes the process of initialization and the process of applying the modified tabu search for obtaining the mandatory solution. This process is repeated for n iterations and the perturbation operator is used by IMTS to modify the mandatory solution to obtain new mandatory solution. This solution will be considered mandatory until the better solution is produced in other iterations. This iterated process of the modified search process will eliminate the conflicting solutions and results in optimal equitable k-coloring solution until β number of consecutive perturbations. Algorithm 2 shows the IMTS procedure for k-ECP. This algorithm determines the best mandatory solution based on the evaluation function $f(s)$.

Algorithm 2 IMTS procedure for k-ECP

Require: Graph $G = (V, E)$, k, β, α
Ensure: The best solution s
Initializing $s \leftarrow$ Solution(V, E, k)
Applying $s \leftarrow$ Modified Tabu Search(s, α)
Consecutive perturbation counter $d \leftarrow 0$ for unchanged s
repeat
    $s' \leftarrow$ Perturbation Operator(s)
    $s'' \leftarrow$ Modified Tabu Search(s', α)
    if $f(s'') < f(s)$ **then**
        $s \leftarrow s''$
        $d \leftarrow 0$
    else
        $d \leftarrow d + 1$
    end if
until $d = \beta$ or $f(s) = 0$
return s

Step 3 of Algorithm 2 presents the initialization process. The sole purpose of the solution initialization process will be to generate an initial solution with fewer conflicts. Algorithm 3 presents the solution initialization process. Let U be the list of unassigned vertex nodes and v is the randomly selected vertex. The set of neighbors of v in V_i is given by $\Gamma^i(v)$. This initialization process is performed by randomly selecting the vertices and assigning them with the suitable k color classes. After the completion of the assigning processes, the remaining vertices are categorized as unassigned vectors and are assigned to one of the existing k-color class based on the greedy approach.

Algorithm 3 Solution initialization of IMTS

Require: Graph $G = (V, E)$, k
Ensure: k-class candidate for ECP
for $i \in [1, k]$ **do**
    $V_i \leftarrow \emptyset$
end for
Set of unassigned vertices $U \leftarrow V$
for $i \in [1, k]$ **do**
    Select a vertex v randomly from V
    $V_i \leftarrow V_i \cup \{v\}$, $U \leftarrow U \setminus \{v\}$
end for
$i \leftarrow 1$
while $U \neq \varphi$ **do**
    $v \leftarrow \arg\min\{|\Gamma^i(v)| : v \in U\}$
    $V_i \leftarrow V_i \cup \{v\}$, $U \leftarrow U \setminus \{v\}$
    $i \leftarrow 1 + (i \bmod k)$
end while

The preliminary process of setting the solutions is performed by defining the initial value of i as 1 and i-th color class V_i as

the initial class. This initial color class is assigned with the unassigned vertex v that has the smallest number of neighbors in V_i. This random assigning process is continued by setting $i \leftarrow 1 + i \; modk$, and repeating the steps again for all other vertices. After assigning color classes to all vertices, the newer solution is saved and the optimal solution is determined by the modified Tabu search process presented in steps 4 and 8 in Algorithm 2.

3.2 Modified Tabu Search Algorithm

The modified Tabu search is achieved by improving the new point generation mechanisms and parameter updating rules of the basic Tabu search [24]. The main purpose of modifying the basic Tabu search is to guarantee the best balance between exploration and exploitation searches and improve the convergence rate such that the algorithm does not end up in the local optimum. The entire search process of the Tabu search consists of the intensification, diversification and refinement phases. The intensification phase initializes the search to quickly obtain optimal point. The diversification phase exploits the unknown spaces for better optimal points while the refinement phase filters the obtained best points and selects the global optimum solution. As defined above, the intensification and refinement phases searches for optimal solution among the available points while diversification phase generates new solutions for the other phases. To improve this process, the Gaussian probability density function (pdf) is used in the modified Tabu search. The main constraint for generating new solutions is that the $68-95-99.7$ rule, which defines that 68% of the points obtained from a Gaussian distribution are inside one standard deviation from the mean value, while 95% of the points are within two and 99.7% are within three standard deviations. This constraint is satisfied by generating new points in a relatively small neighbor of the specific point. Similarly for diversification phase, better local optima must be obtained to avoid stagnating at a local optimal point. For this purpose, Cauchy pdf is used which produce new points that stay in unexplored spaces from the current optimal points without constraints like Gaussian. The Gaussian and Cauchy pdf are given by.

$$G(x_i) = \frac{1}{\sqrt{2\pi\sigma_i^2}} exp\left(-\frac{(x_i-\mu_i)^2}{2\sigma_i^2}\right) \tag{5}$$

$$C(x_i) = \frac{1}{\left(\pi\gamma_i\left[1+\left(\frac{x_i-a_i}{\gamma_i}\right)^2\right]\right)} \tag{6}$$

where x_i is the solution point, μ_i is the mean value, σ_i is the standard deviation, γ_i is the scaling parameter and a_i is the location of the optimal solution. Based on these pdf functions, the new solution points can be obtained as

$$x_i = \mu_i + \sigma_i P \tag{7}$$

$$x_i = a_i + \gamma_i \; tan\left[\pi\left(P-0.5\right)\right] \tag{8}$$

Here P is the accumulation function specified as the integral of either Gaussian or Cauchy pdf denoted as $F\left(u\right)$ in the below equation.

$$P = \int_{-\infty}^{\infty} F\left(u\right) du \tag{9}$$

Secondly, the parameter updating rule is improved based on the scalar parameter γ and standard deviation σ. Setting larger value of these parameters will yield in low convergence speed while a smaller value will reduce the global searching capability. Hence dynamic updating is used for automatically determining these parameters for obtaining optimal solution.

$$a_{i+1} = a_0 - a_0\left(1-\frac{1}{i}\right)^q \tag{10}$$

where $a_0 = \frac{x_u - x_l}{10}$ and $q = log_{29/30}(w)$ with w is the attenuation parameter and x_u and x_l are the higher and lower limits of the dynamic strategy.As the searches advances, a is reduced steadily and improves the converging speed of the algorithm. Based on this process, the search process is performed in IMTS which is given in Algorithm 4.

Specified a neighbourhood function N, the evaluation function $f(s)$ in equation (3), and a given initial solution s_0, the modified Tabu search provides the best solution to replace the mandatory solution. Here d is the parameter set to count the consecutive iterations where s_b is not updated i.e., s_b stays the best solution. By using the modified steps as described above, the optimal solution is obtained in less time and also the solution is globally optimal, thus averting the local optima situation. The utilization of Gaussian and Cauchy pdf in Tabu search has significantly improved the optimal solution determination as shown in Figure 1.

Algorithm 4 Modified Tabu Search process

Require: Input solution s_0, the neighbourhood N, and α
Ensure: Best solution s_b
Generate new solution using $G(x_i)$ and $C(x_i)$
Current solution $s \leftarrow s_0$
Best solution obtained until now $s_b \leftarrow s$
Iteration counter $d \leftarrow 0$
repeat
    Select the best neighbourhood solution $s' \in N(S)$
    $s \leftarrow s'$
    Update parameters using Equations 8 and 9
    Update Tabu list
    if $f(s) < f(s_b)$ **then**
        $s_b \leftarrow s$
        $d \leftarrow 0$
    else
        $d \leftarrow d + 1$
    end if
until $f(s) = 0$
return s_b

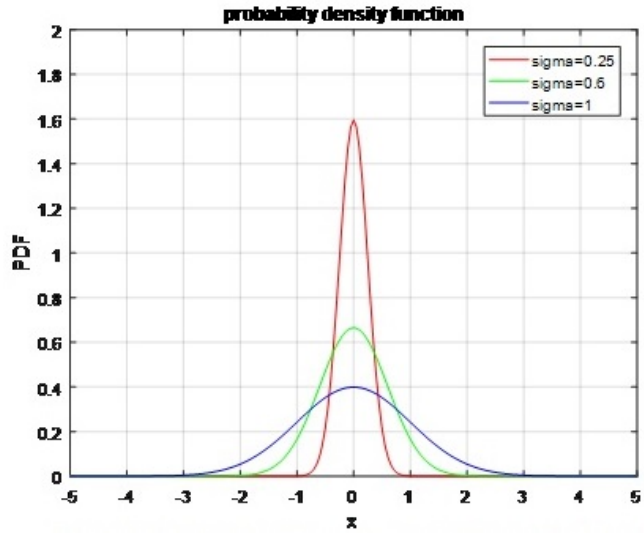

Figure 1: Gaussian and Cauchy pdf performance in IMTS

4 Application of IMTS for ECP in Scheduling ICC Cricket World Cup 2019

ICC Cricket World Cup is the global competition conducted by the International Cricket Council (ICC) every four years. The Men's World Cup tournament held in 2019 is modeled as ECP for scheduling the tournament. The 2019 event was contested by men's national teams of ten cricketing countries. It was from 30 May to 14 July, 2019 with the league matches taking place in round robin format. The semi-finals and final were played as knock-out format. The tournament was organized in seven cricket grounds across six cities in England and Wales. The matches were scheduled on the basis of flexibility of the TV audience with one match taking place each weekday and two matches taking place in weekends to attract the cricketing crowds. This strategy is mainly based on the profit model but it also considers the travel flexibility of the cricketing players and officials. In this work, the multi-nation tournament is considered for evaluating the effectiveness of ECP in solving the scheduling problems. For simplicity, only the main matches in the league stage is considered while knock-out matches are left out due to their easy scheduling.

The 10 teams participated in the tournament are sorted in alphabetical order for evaluation. Afghanistan, Australia, Bangladesh, England, India, New Zealand, Pakistan, South Africa, Srilanka and West Indies are the teams. They are numbered $1, 2, \cdots, 10$ for match ordering. By sorting the match combinations, the single round robin format will lead to 45 matches in 9 rounds which are shown in the Table 1

As the tournament is single round robin, the teams are ordered as the nodes of a graph $G = (V, E)$ where each vertex $v \in V$ as

Table 1: Round-robin schedule format

Round	Matches				
1	1,2	3,9	4,8	5,7	6,10
2	1,3	2,10	4,9	5,8	6,7
3	1,4	2,3	5,9	6,8	7,10
4	1,5	2.4	3,10	6,9	7,8
5	1,6	2.5	3,4	7,9	8,10
6	1,7	2,6	3,5	4,10	8,9
7	1,8	2,7	3,6	4,5	9,10
8	1,9	2,8	3,7	4,6	5,10
9	1,10	2,9	3,8	4,7	5,6

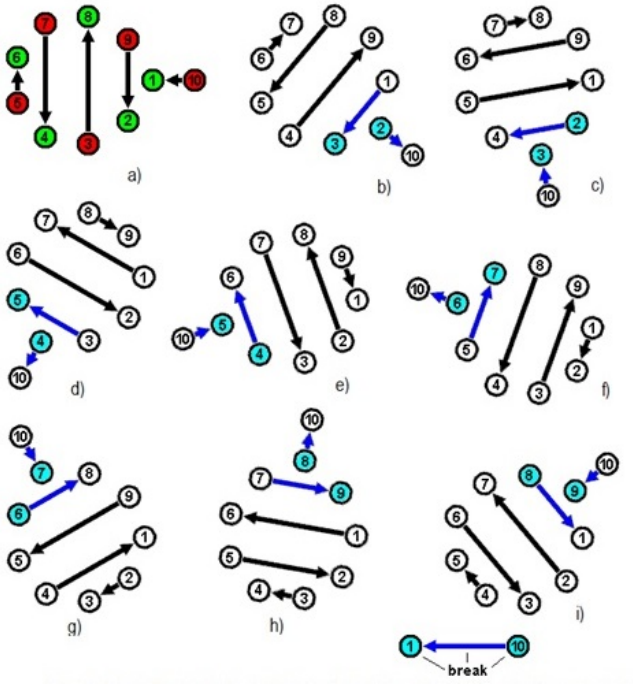

Figure 2: ICC World Cup Round robin schedule of nine rounds

an unordered pair $v = \{t_i, t_j\}$, representing a match amongst teams t_i and t_j. The vertices number $|V|$becomes $\frac{1}{2}n(n-1)$ and the number of possible colors $k = n - 1$ is determined for concrete scheduling. The edge dimensions are given by [25] as in equation 11

$$D = \frac{4(n-2)+1}{|V|-1} \tag{11}$$

Figure 2 shows the IMTS for World Cup tournament by splitting the scheduling process for each day. In this pattern, the tournament can be organized in 10 or 11 days including the knock-out matches. Each round can be contested in one day at 5 venues and thus the time can be minimized and also the expenditure.

Figure 3 shows the input graph plotted for evaluation for the tournament with the said 10 teams. The plot is obtained by the node plot structure used to construct the graph vertices. The edges are connected based on the matches assumed.

Figure 4 shows the Plot area of the graph for assigning the 10 teams as vertices of the graph G and utilizing it in scheduling the matches. Once scheduled, the edges of the graph denote the matches and coloring of the vertices illustrate the teams that can be scheduled in the same round. Scheduling of the matches on the same day reduces the overall timing of the schedule. On comparing with the original schedule of the tournament, few constraints are avoided. The main constraint is the scheduling based on TV audiences. The other constraint is the allocation of reserve days and possible extensions of playing time that might affect the travel schedule.

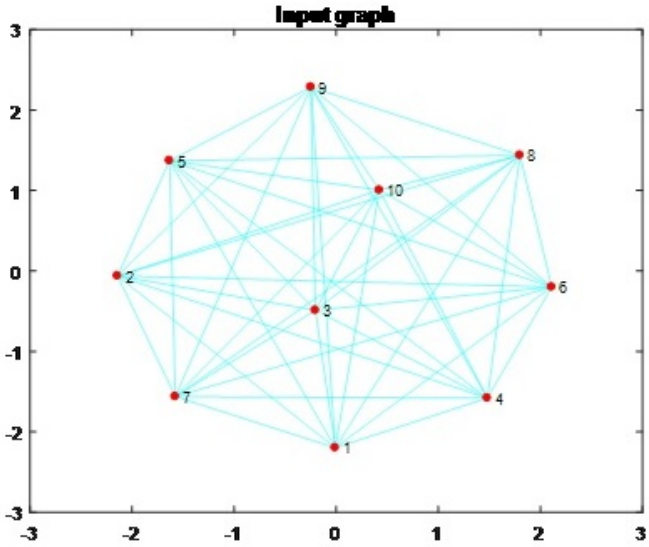

Figure 3: Input Graph of World Cup Tournament

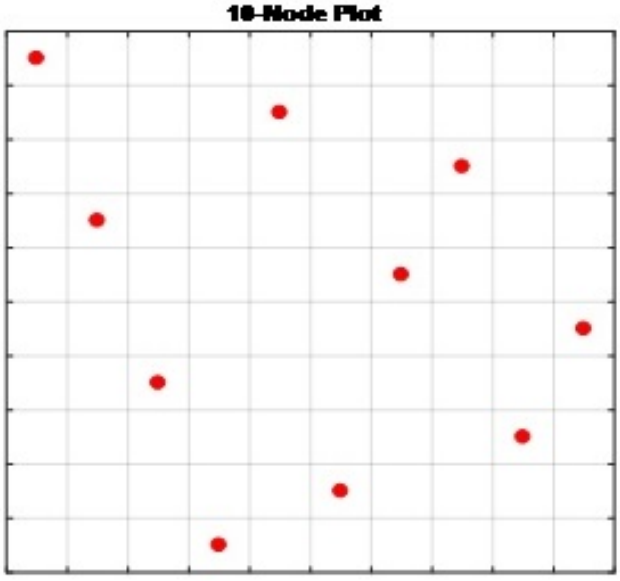

Figure 4: Plotting of the Scheduled Teams in Graph Vertices

Figure 5 shows the coloring output of the World Cup tournament scheduling problem. From the results, it can be seen that the coloring constraint of no adjacent vertices have the same colour and equity constraint are satisfied by the IMTS approach. This justifies the performance of the suggested IMTS algorithm for the ECP.

5 Performance Evaluation

The approximation of the proposed IMTS for ECP is performed in the previous section for the scheduling problem of ICC Cricket World Cup 2019. The results have shown effectiveness of the proposed approach. In addition to that evaluation, the proposed IMTS is applied on benchmark instances which are commonly in evaluating GCP and ECP problems. The experimental setup is given in the Table 2

The performance of the IMTS is provided in Table 3 along with a comparison of existing methods namely Tabu Search (TS) [17] and BITS [19]. The proposed IMTS is measured for the value of initial $k\,(\mathbf{k}_i)$, best $k\,(\mathbf{k}_b)$ and average values of $k\,(\mathbf{k_{avg}})$ for 20 runs for estimating the success rate $(\mathbf{S}R)$. A total of 60 benchmark instances are utilized which weregenerated in DIMACS machine benchmark format with varying number of nodes available at the following link: https://turing.cs.hbg.psu.edu/txn131/graphcoloring.html. The evaluations are performed for the proposed IMTS for 20 runs on

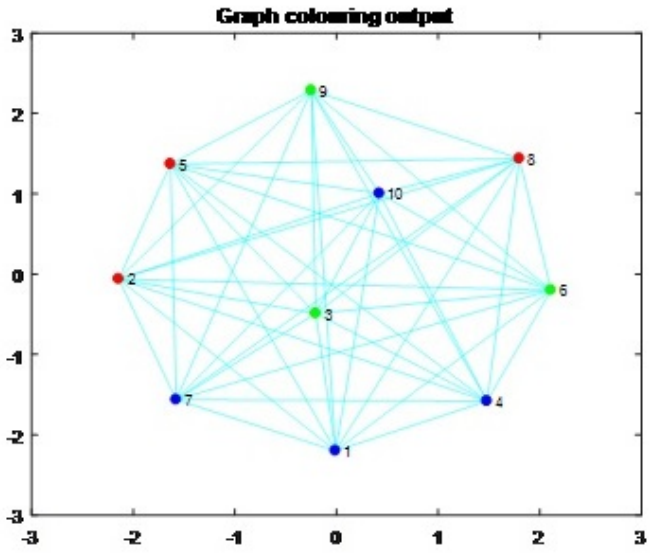

Figure 5: Equitable Coloring of the World Cup Scheduling Problem

Table 2: Experimental Setup

OS	Windows 7 and above, 32bit
Processor	Intel core i5 3470 3.2 GHz
Storage	500GB Intel SSD SC2CT060A3 ATA device
RAM	4GB DDR3
Network bandwidth	1 Gbps
Simulation tool	MATLAB v.2016b
Simulation time	600 seconds
Total Runs	20
Number of Instances	60

each instance to validate the success rates.

From the table 3, it can be found that the IMTS algorithm has better values of k_i, k_b and k_avg with significantly higher success rates than the existing schemes TS and BITs on most instances, thus suggesting that the proposed IMTS reduces the convergence rate and hence the final solutions are better. For a total of 20 runs of the proposed IMTS on each instance, the algorithm returned successful solutions on most runs, indicated by the SR rate. This shows the significance of the proposed approach in handling the ECP and its applications to real-world problems.

6 Conclusion

The introduced IMTS algorithm for tackling the equitable coloring problem demonstrates marked enhancements in performance, attributed to its integration of the modified Tabu search technique alongside a strategic backtracking approach. The algorithm's efficacy is substantiated through its application to address the scheduling conundrum of the ICC Cricket World Cup tournament, yielding favorable outcomes. Furthermore, assessments conducted on benchmark instances underscore the IMTS algorithm's superiority in delivering improved results and notably accelerated convergence rates for the ECP. The algorithm's effectiveness is a synergy of the combined efforts of its constituent processes. Notably, the IMTS algorithm's versatility extends to the successful resolution of other real-world NP-hard problems as well.

Acknowledgments

The present version of this paper owes much to the comments, corrections, suggestions, typographical errors and kind remarks of the learned referee.

Authors' Contributions

MV and KP have found new results and proved the same in this paper. D and INC have given the idea for the data and have drawn the graphs using MATLAB software. All four authors have read and approved the final manuscript.

Table 3: Computational results of IMTS algorithm on benchmark instances

Instance	Nodes	TS	BITS				IMTS			
		k_b	k_i	k_b	k_{avg}	SR	k_i	k_b	k_{avg}	SR
DSJC125.1	125	5	5	5	5	20/20	5	5	5	20/20
DSJC125.5	125	18	17	17	17.5	20-Oct	17	16	16.5	20-Dec
DSJC125.9	125	45	44	44	44	20/20	43	42	42.65	20/20
DSJC250.1	250	8	8	8	8	20/20	8	8	8	20/20
DSJC250.5	250	32	32	30	31.9	20-Jan	31	30	30.45	20-Aug
DSJC250.9	250	83	72	72	72	20/20	70	69	69.65	20/20
DSJC500.1	500	13	13	13	13	20/20	13	13	13	20/20
DSJC500.5	500	63	57	56	56.95	20-Jan	53	53	53.25	20-Jul
DSJC500.9	500	182	130	129	129.9	20-Feb	127	127	127.6	20-Nov
DSJR500.1	500	12	12	12	12	20/20	12	12	12	20/20
DSJR500.5	500	133	126	126	126.3	14/20	121	121	121.2	17/20
DSJC1000.1	1000	22	22	21	21.95	20-Jan	21	21	21.25	20-Jul
DSJC1000.5	1000	112	112	103	105.1	20-Mar	105	103	104.95	20-Dec
DSJC1000.9	1000	329	254	252	253.3	20-Jan	232	230	232.65	20-Nov
R125.1	125	-	5	5	5	20/20	5	5	5	20/20
R125.5	125	-	36	36	36	20/20	36	36	36	20/20
R250.1	250	-	8	8	8	20/20	8	8	8	20/20
R250.5	250	-	67	66	66.65	20-Jul	66	66	66	20-Nov
R1000.1	1000	-	20	20	20	20/20	20	20	20	20/20
R1000.5	1000	-	269	250	250.4	20-Dec	257	248	248.34	16/20
le450_5a	450	-	5	5	5	20/20	5	5	5	20/20
le450_5b	450	7	5	5	5	20/20	5	5	5	20/20
le450_5c	450	-	5	5	5	20/20	5	5	5	20/20
le450_5d	450	8	5	5	5	20/20	5	5	5	20/20
le450_15a	450	-	15	15	15	20/20	15	15	15	20/20
le450_15b	450	15	15	15	15	20/20	15	15	15	20/20
le450_15c	450	-	15	15	15.1	18/20	15	15	15	19/20
le450_15d	450	16	15	15	15.7	20-Jun	15	15	15	15/20
le450_25a	450	-	25	25	25	20/20	25	25	25	20/20
le450_25b	450	25	25	25	25	20/20	25	25	25	20/20
le450_25c	450	-	26	26	26	20/20	26	26	26	20/20
le450_25d	450	27	26	26	26	20/20	26	25	26.1	20/20
wap01a	2368	46	43	42	42.6	20-Aug	44	41	42.1	15/20
wap02a	2464	44	42	41	41.8	20-Apr	41	41	41	13/20
wap03a	4730	50	46	45	45.05	19/20	44	42	43.55	19/20
wap04a	5231	-	46	44	44.15	17/20	45	45	45.1	15/20
wap05a	905	-	50	50	50	20/20	50	50	50	20/20
wap06a	947	-	42	41	41.7	20-Jun	41	41	41	20-Nov
wap07a	1809	-	43	43	43.05	19/20	43	41	41.8	17/20
wap08a	1870	-	43	43	43.05	19/20	42	41	41.75	17/20
flat300_28_0	300	36	35	34	34.7	20-Jun	33	33	33.45	20-Sep
flat1000_50_0	1000	-	112	101	102.8	20-Jan	102	99	101.2	20-Mar
flat1000_60_0	1000	-	112	102	102.9	20-May	109	101	102.5	20-Aug
flat1000_76_0	1000	112	112	102	103.4	20-Mar	109	99	101.65	20-Jan
latin_square_10	900	130	129	115	120	20-Jan	121	113	117.17	20-Jun
C2000.5	2000	-	202	201	201.6	20-Jul	198	197	198.4	20-Aug
C2000.9	2000	-	504	502	502.4	20-Nov	502	493	498.6	14/20
mulsol.i.1	197	50	49	49	49	20/20	49	48	48.45	20/20
mulsol.i.2	188	48	36	36	36.35	13/20	33	31	32.8	18/20
fpsol2.i.1	496	78	65	65	65	20/20	61	61	61	19/20
fpsol2.i.2	451	60	47	47	47	20/20	43	43	43.25	20/20
fpsol2.i.3	425	79	55	55	55	20/20	53	51	52.5	20/20
inithx.i.1	864	66	54	54	54	20/20	49	49	50.35	20/20
inithx.i.2	645	93	36	36	36.35	13/20	35	31	33.75	15 /20
inithx.i.3	621	-	38	37	37.45	20-Nov	35	35	35	20-Oct
zeroin.i.1	211	51	49	49	49	20/20	45	45	45	19/20
zeroin.i.2	211	51	36	36	36	20/20	34	33	33.4	20/20
zeroin.i.3	206	49	36	36	36	20/20	33	33	33	20/20
myciel6	95	7	7	7	7	20/20	7	7	7	20/20
myciel7	191	8	8	8	8	20/20	8	8	8	20/20

Competing Interests

The authors declare that they have no competing interests.

References

[1] Jonathan L Gross and Jay Yellen. *Graph theory and its applications*. CRC Press, 2005.
[2] LR Foulds. *Graph theory applications*. Springer Science & Business Media, 2012.
[3] Narsingh Deo. *Graph theory with applications to engineering and computer science*. Courier Dover Publications, 2017.
[4] P. M. Pardalos, T. Mavridou, and J. Xue. The graph coloring problem: A bibliographic survey. In *Handbook of combinatorial optimization*, pages 1077–1141. Springer, 1998.
[5] T. Vredeveld and J. K. Lenstra. On local search for the generalized graph coloring problem. *Operations Research Letters*, 31(1):28–34, 2003.
[6] H. Furmanczyk and M. Kubale. Equitable coloring of graphs. *Contemporary mathematics*, 352:35–54, 2006.
[7] H. Furmańczyk. Equitable coloring of graph products. *Opuscula Mathematica*, 26(1):31–44, 2006.
[8] H. Furmańczyk and M. Kubale. Equitable and semi-equitable coloring of cubic graphs and its application in batch scheduling. *Archives of Control Sciences*, 25(1):109–116, 2015.
[9] A. Drexl and S. Knust. Sports league scheduling: graph-and resource-based models. *Omega*, 35(5):465–471, 2007.
[10] R. Lewis and J. Thompson. On the application of graph colouring techniques in round-robin sports scheduling. *Computers & Operations Research*, 38(1):190–204, 2011.
[11] Z. Yan, W. Wang, and X. Zhang. Equitable colorings of cartesian products with balanced complete multipartite graphs. *Discrete Applied Mathematics*, 180:200–203, 2015.
[12] L. Bahiense, Y. Frota, T. F. Noronha, and C. C. Ribeiro. A branch-and-cut algorithm for the equitable coloring problem using a formulation by representatives. *Discrete Applied Mathematics*, 164:34–46, 2014.
[13] P. San Segundo. A new dsatur-based algorithm for exact vertex coloring. *Computers & Operations Research*, 39(7): 1724–1733, 2012.
[14] I. Mendez-Diaz, G. Nasini, and D. Severin. A polyhedral approach for the equitable coloring problem. *Discrete Applied Mathematics*, 164:413–426, 2014.
[15] I. Mendez-Diaz, G. Nasini, and D. Severin. An exact dsatur based algorithm for the equitable coloring problem. *Electronic Notes in Discrete Mathematics*, 44:281–286, 2013.
[16] I. Mendez-Diaz, G. Nasini, and D. Severin. A dsatur based algorithm for the equitable coloring problem. *Computers & Operations Research*, 57:41–50, 2015.
[17] I. Mendez-Diaz, G. Nasini, and D. Severin. A tabu search heuristic for the equitable coloring problem. In *International Symposium on Combinatorial Optimization*. Springer, 2014.
[18] W. Wang, J. K. Hao, and Q. Wu. Tabu search with feasible and infeasible searches for equitable coloring. *Engineering Applications of Artificial Intelligence*, 71:1–14, 2018.
[19] X. Lai, J. K. Hao, and F. Glover. Backtracking based iterated tabu search for equitable coloring. *Engineering Applications of Artificial Intelligence*, 46:269–278, 2015.
[20] W. Sun, J. K. Hao, W. Wang, and Q. Wu. Memetic search for the equitable coloring problem. *Knowledge-Based Systems*, page 105000, 2019.
[21] P. Galinier and A. Hertz. A survey of local search methods for graph coloring. *Computers & Operations Research*, 33(9): 2547–2562, 2006.
[22] P. Galinier, Z. Boujbel, and MC. Fernandes. An efficient memetic algorithm for the graph partitioning problem. *Annals of Operations Research*, 191(1):1–22, 2011.
[23] P. Galinier, J. P. Hamiez, J. K. Hao, and D. Porumbel. Recent advances in graph vertex coloring. In *Handbook of optimization*, pages 505–528. Springer, 2013.
[24] S. An, S. Yang, S. L. Ho, T. Li, and W. Fu. A modified tabu search method applied to inverse problems. *A modified tabu search method applied to inverse problems*, 47(5):1234–1237, 2010.
[25] R. Lewis and J. Thompson. On the application of graph colouring techniques in round-robin sports scheduling. *Computers & Operations Research*, 38(1):190–204, 2011.

El Cezeri
Journal of Science and Engineering
ISSN: 2148-3736

Research Article

Unveiling the Power of Blockchain in Pharmaceutical Supply Chains: Strengthening Security and Improving Drug Traceability

Vandani Verma[1a]
[1] Department of Mathematics, Amity Institute of Applied Sciences, Amity University, Noida, India
vandaniverma@yahoo.com

DOI : 10.31202/ecjse.1338782
Received: 07.08.2023Accepted: 13.05.2024
How to cite this article:
Vandani Verma " Unveiling the Power of Blockchain in Pharmaceutical Supply Chains: Strengthening Security and Improving Drug Traceability ", El-Cezeri Journal of Science and Engineering, Vol: 11, Iss:2, (2024), pp.(142-151).
ORCID: 0000-0003-4175-9227

Abstract : Pharmaceutical supply chains involve multiple stakeholders at various stages, beginning with the API source, moving on to the medication manufacturer, packaging and distribution firms, administrative regulators, hospitals, pharmacies, and finally the patient. Because of the difficulty in tracking and ensuring authenticity, counterfeit drugs are more likely to penetrate the distribution system. Increasing counterfeit medicinal products in the market pose a potential threat to the pharmaceutical supply chain and to the lives of innocent people. There is a need for technology that could provide privacy, trust, transparency, security, authorization, and authentication to clients and show proof of the origin of products. Due to significant qualities such as decentralization, transparency, a trust-free environment, anonymity, and immutability, blockchain-based drug traceability provides a viable answer to this problem. Blockchain technology provides an efficient and cost-effective option for improving various drug traceability functions and procedures to assure appropriate identification. Blockchain is being employed in other areas of the pharmaceutical sector, such as packaging and supply chain activities. This paper describes the challenges in the pharmaceutical supply chain and how blockchain combined with the pharmaceutical supply chain can be a problem solver. We also review a blockchain architecture for product traceability in the pharmaceutical supply chain system.

Keywords : Blockchain Architectures, Drug Traceability, Healthcare, Information Sharing, Pharmaceutical Supply Chain, Security

1 Introduction

Cryptography serves as the fundamental basis for the blockchain system. The advent of blockchain technology, which offers a reliable and transparent framework for the storage and dissemination of information, is presenting novel opportunities to tackle significant issues pertaining to data privacy, security, and integrity across various domains, such as healthcare. Messages were encoded millennia ago as a protective measure against potential adversaries. The literature of the 1980s and 1990s featured numerous articles that posited the integration of cryptography with secure data chains and the initiation of digital currencies. In the year 1982, David Chaum [1] introduced the concept of digital currency and blind signatures, which enable individuals to affix their signature to a document, asserting their ownership while simultaneously concealing the information contained within the document. Subsequently, in 1990, David founded DigiCash [2], a cryptographic system that utilized both private and public keys, as well as signatures, to generate an untraceable form of digital currency. Regrettably, DigiCash faced financial insolvency and was officially declared bankrupt in 1998. Adam Back is credited with the establishment of hash cash, a proof-of-work system created to restrict the spread of unsolicited emails, colloquially called spam, in 1997. Prior to sending an email, the sender would be required to verify their ability to solve a computational puzzle, thereby consuming computational resources and heightening the expenses associated with sending out large volumes of spam emails. This innovative approach was subsequently expounded upon in a scholarly article published in 2002 [3]. In 1998 [4], the concept of "bit gold" was put forth as a decentralized form of digital currency. It involved a combination of proof-of-work and a network of computers that recognized the legitimacy of the proof-of-work and incorporated it into the subsequent problem, along with a timestamp. However, it is important to note that bit gold was purely theoretical and never attained the status of a genuine currency. In 1998, another article [5] was published that elucidated the fundamental principles of digital currencies, such as Bitcoin, and this research is referenced in Satoshi Nakamoto's seminal Bitcoin paper. It was the extensive efforts undertaken from the 1980s to the 2000s that established the foundational framework for Bitcoin and the underlying blockchain technology. In 2008, Satoshi Nakamoto [6] outlined in his article the process of Bitcoin creation and the linking of transaction blocks into chains. With Satoshi Nakamoto's establishment of the Bitcoin network and its inaugural blockchain in 2009, the concept became a tangible reality. This foundational blockchain

played a crucial role in Bitcoin, thwarting double spending and serving as a decentralized public ledger for all transactions within the Bitcoin network. Nakamoto further solidified this by mining the inaugural block on the Bitcoin network, famously dubbed the "genesis block." In blockchain technology, all records, whether they be transactional or medical, are stored in blocks. Once a block reaches its capacity with data, it becomes part of the chain of preceding blocks, and a new block is generated for subsequent data entries. This immutable nature ensures that once added to the blockchain, blocks cannot be altered, with any modifications requiring notification to all previous users. The scalability and decentralized nature of blockchain technology make it invaluable for improving supply chain processes, enhancing the global economy, and promoting project sustainability. Every aspect of the supply chain, from raw materials to transportation logistics to human resources, can be efficiently tracked using blockchain technology. Numerous studies [7], [8], and [9] have suggested alterations and devised novel methodologies to enhance and implement a diverse range of applications, such as smart contracts, supply chain management, and healthcare. This article discusses the possibilities and limitations of blockchain technology for drug tracing in the pharmaceutical supply chain. The main contributions of our study are as follows:

- We explore the issues of the pharmaceutical supply chain without blockchain.
- We analyse the suitability of Blockchain properties for drug tracing by giving an overview and several architectural designs.
- We discuss solutions in pharmaceutical supply chain management leveraging blockchain technology.
- We review thorough implementation of Blockchain solutions in pharmaceutical supply chains, launched as the eZTracker Platform by Zuellig Pharma.
- We investigate a Blockchain SCMS use case for COVID-19 vaccine distribution.

2 Challenges in Pharmaceutical Supply Chain Management System

- Counterfeit Drug Prevention: Products that are purposefully manufactured and have their identity labelled to appear to be genuine and the sale of fake medications harms both patients and the pharmaceutical industry as these may be harmful or ineffective to patients. Avoiding counterfeiting that can only be accomplished by identifying illegal intermediaries or determining provenance is a big challenge.
- Product Distribution: In supply chain management, goods are exchanged between several parties, none of whom are aware of any previous exchanges that took place. The drug supply chain lacks the infrastructure to ensure comprehensive manufacturer-to-end user tracking. Drugs are initially given to wholesalers by the manufacturer, who then give them to hospitals or pharmacies and the absence of process transaction tracking in classical supply chain is challenging its effective implementation.
- Tracking and Tracing: Quality assurance and tracking of all stages of drug production from manufacturer to consumer has always posed a challenge. Deaths have resulted from the distribution of substandard and counterfeit drugs, prompting governments around the globe to incorporate trace and track systems to monitor pharmaceuticals supply chains.
- Safety and Security: Classical drug supply chain management characteristics cannot broadcast necessary information securely and reliably. Data can be easily removed, altered, and tampered with in many cases. Keeping data safe from alteration, removal, and modification while sending it securely and reliably all over the network is a bigger challenger to users.
- Inaccurate Stock Data: A lack of visibility into inventory or stock data is one of the most serious issues in the supply chain. Healthcare facilities, manufacturers, and vendors would lack up-to-date inventory information. Many hospitals, for example, are unaware of the number of resources they have or will require during the covid-19 pandemic. Hospitals that use antiquated software to manage inventory, procurement, shipping, and other operations may struggle to meet timelines.
- Quality Priority: Because medicines deal with people's lives, quality is the most important factor to consider. The major function of a supply chain is to retain the product's quality so that it is effective until it is consumed by the customer. For example, maintaining proper temperature and humidity levels. Many systems do not provide such assurance.

3 Characteristics and Architecture of Blockchain for Drug Traceability

In this section, we discuss the characteristics of blockchain in context with drug traceability and two further architectures with these characteristics as proposed by Uddin et al. [7]. Following are the characteristics of block chain:

- Immutability: Immutability is a core pillar of blockchain technology, ensuring the integrity of the digital ledger by making it immutable. Unlike traditional money transfer systems, which allow transaction details to be easily tampered with and require the involvement of trusted third parties to ensure data integrity, blockchain works on the principle that each block is intricately linked to its predecessor, significantly reducing the likelihood of block alteration.

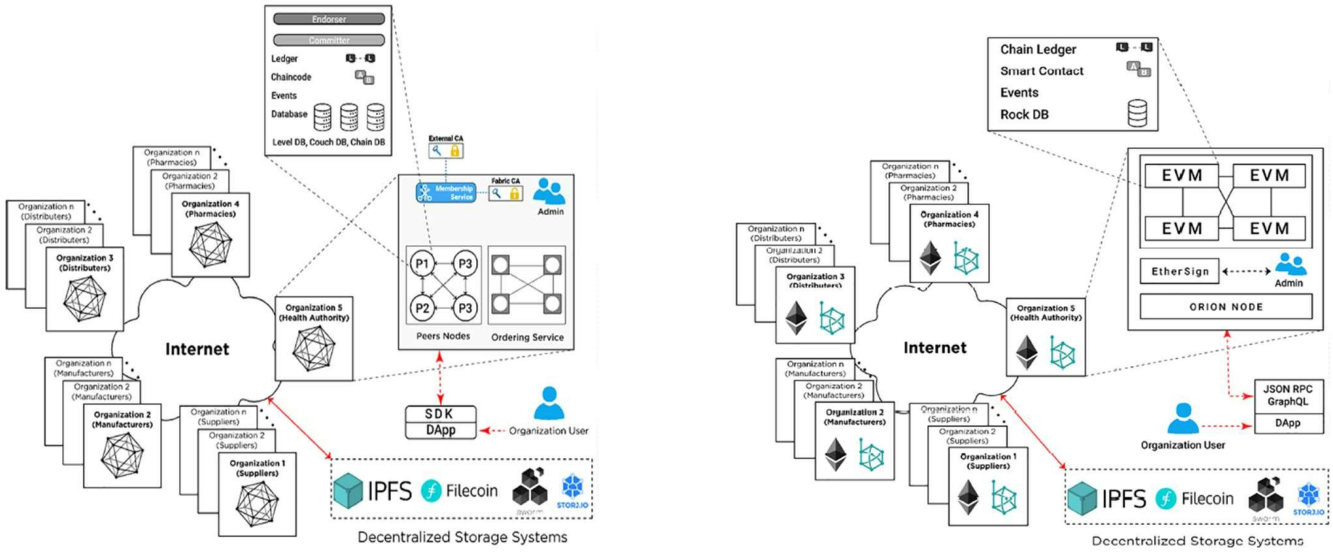

(a) Hyperledger Fabric Blockchain Architecture **(b) Hyperledger Besu Blockchain Architecture**

Figure 1: Blockchain Architecture [7]

- Decentralization: Decentralisation is a distinguishing feature of blockchain networks, which eliminates the need for a trusted third party or central authority to supervise transactions. This decentralised distributed ledger solution efficiently overcomes issues such as single-point failures and dependency on third parties to ensure transaction integrity.
- Heightened Security: After transaction details are hashed, appended to a block, and made public, altering the transaction information becomes impossible without modifying the hash value. This is because the blockchain relies on irreversible hashes for all its data. Thus, anyone attempting to alter data would need to compromise every block across the entire network.
- Distributed Ledgers: All details regarding a transaction and its participants are distributed among all involved parties. This ensures that any malicious alterations to a transaction can be readily detected, promoting transparency, and making the system resistant to tampering.

A distributed ledger technology called Hyperledger Fabric [7] (Fig. 1a as presented in [7]) provides reliable solutions with high degrees of secrecy, resilience, adaptability, and scalability. By enforcing trust between several parties without requiring mining, it preserves desired blockchain characteristics like block immutability and avoids double spending through the use of smart contracts. It is perfect for intricate supply chain systems because of its transaction throughput, which may approach several thousand transactions per second. The Hyperledger Fabric medication traceability architecture [7] incorporates a blockchain-based supply chain system that protects privacy, confidentiality, and data security. The notion of channels separates business logic from data privacy regulations across stakeholders. A permissioned private blockchain network is formed, with a Health Authority registering organisations and users through the membership service provider. This protects privacy and secrecy by decentralising identity management. At its heart, Hyperledger Fabric consists of peer nodes that store ledger copies and execute smart contracts, while an ordering service receives, orders, and broadcasts transactions for validation. The transaction processing approach consists of four phases: proposal, endorsement, ordering, and execution, which ensures determinism and dependability in updating the ledger's state. Hyperledger Fabric's principles provide safe and transparent transaction management for many parties in the pharmaceutical supply chain, reducing hazards such as counterfeit pharmaceuticals.

To execute medication-related traceability transactions on a Hyperledger Besu network [7] (Fig. 1b as presented in [7]), a Distributed App (DApp) sends signed private transaction requests to a Hyperledger Besu EVM node. These transactions include recipient addresses (or privacy group IDs), sender addresses, and transaction types. Privacy groups, denoted by unique IDs, grant access to certain data exclusively to designated accounts or nodes. The DApp interface transmits transactions to Orion via a Private Transaction Handler, which distributes them to the appropriate Orion nodes. Orion nodes record transactions in a state database and provide the transaction hash to the Private Transaction Handler. Additionally, Privacy Marker Transactions (PMT) are generated, mined into blocks, and broadcasted. The Mainnet Transaction Processor executes PMTs, which are then executed and committed to the private world state on nodes that have the relevant precompiled smart contract. Nodes without a contract ignore the marker transaction.

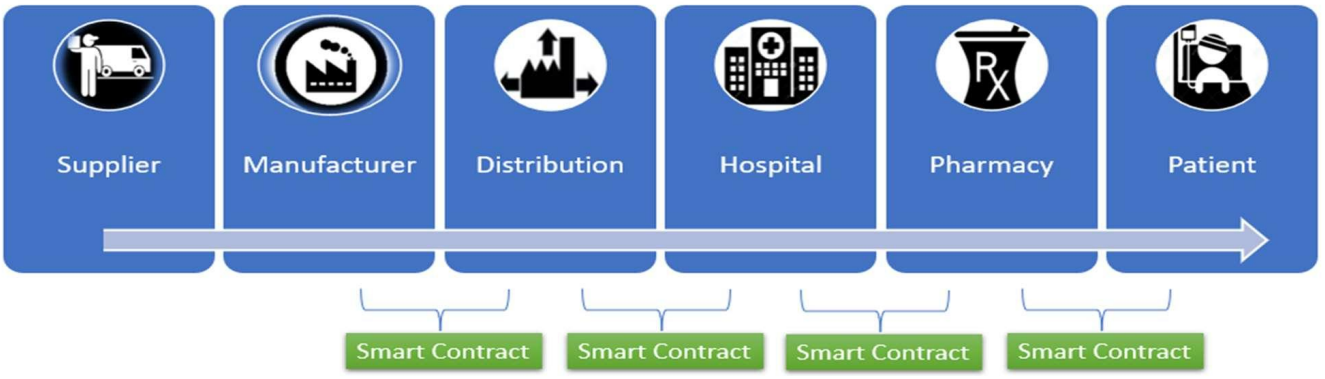

Figure 2: Blockchain for Product Traceability

4 Pharmaceutical Supply Chain Management System with Blockchain

The pharmaceutical supply chain comprises of several stakeholders, like a supplier, manufacturer, distributor, retailer, pharmacy, and at last, the consumer (patient). Product distribution frequently necessitates sophisticated packing, unpacking, and repacking methods, making drug authenticity, and tracking incredibly hard. Since medicine deals with humans' lives, quality is of the utmost importance, and it's not only the quality while manufacturing but also maintaining the quality of the products so that they are efficient until the time they are consumed by the patient, and so it's the responsibility of the manufacturer to store the drugs at the right temperature, ensuring that the storage humidity is right, depending on the storage requirement for the product. Also, in the pharma industry, whenever there is a product on the shelf-life, and it is not sold, either because it is expired, or it is near expiration, or because it may have quality issues, the supply chain (Fig. 2) ensures the pickup of these products from the complex network of thousands of retailers, distributors, and wholesalers and disposes of them. This scenario also offers a chance for the counterfeit drug industry, where they can buy these expired drugs and reprint their expiry labels to sell them into the market.

This scenario of the introduction of counterfeit drugs into the market poses a challenge to bringing all the supply chain (raw material-producing companies, manufacturers, distributors, and then the different channels through which they call the hospital and clinic) and, at the end, the patient together, as they tend to be a fragmented ecosystem altogether. The first challenge is to share information between parties when there's no standard mechanism for data transfer and a lack of trust, as people don't want to share data ownership. Lack of information and communication between parties create entry points for illicit products from outside the system. The second challenge is to track a product's activity from end to end along the supply chain so that information is passed over consistently and is being recorded in a timely manner, making it accessible to whoever needs access to that data. Then, the third challenge is: how do you give drug supply information to a patient so that a patient is able to verify it through a mobile phone, investigate the supply chain, and decide before purchasing the medicine or getting vaccinated? Thus, a verified block chain-based pharmaceutical supply chain is the solution to these challenges. Several studies have been done towards implementing blockchain in the pharmaceutical supply chain; some of the relevant ones are listed in the table 1

Each participating entity uploads its transaction to the blockchain network (depending on the finished activity). At the first stage, many manufacturers send raw materials to the producer and record their transactions on the block chain network. This transaction contains information such as the raw material's name, quantity, and quality, as well as the supplier's location.

When the manufacturer receives the raw materials, smart contracts are activated, and appropriate action is taken. All network authorities have access to the network and can check the validity and history of any medicine at any time. Similarly, the manufacturer interacts with the network at the next level, and so on. Thus, in a block chain network, various aspects of the supply chain are recorded, and every new transaction in the network is recorded in an immutable block that is time-stamped to keep track of the exact product in the end-to-end chain and ensures that the block's details are not tampered with. At last, when the drugs are delivered to the patient, he can trace the drug through a mobile app that allows him to scan a data matrix QR code on the medication (Fig. 3) and be able to trace right the way back to the origin of that product and provides information like where it was manufactured, where it came from, where it's been, how long it was in certain locations, where it was stored in the right temperature controls, and that it's been through a supply chain and being handled in the correct way, so it transforms a patient's mobile phone into a cloud-based verification tool.

5 Review of eZTracker designed by Zuellig Pharma[31]

Recognizing the need for blockchain networks in the pharmaceutical and healthcare industries (Table 1), Zuellig Pharma: a professional services firm, has created a platform that would serve as the foundation for a complete plant-to-patient supply

Table 1: Blockchain in Healthcare Supply chain Management

S. No.	Reference	Key Findings
1	Wu et al. [10]	Introduced a delivery structure comprised of several private distributed ledgers and a blockchain public ledger, as well as its implementation.
2	Jochumsen et al. [11]	Using a literature review and expert interviews, this study investigates the impact of Blockchain on the pharmaceutical supply chain. The authors have interviewed various Co-Founder and Executive Director pharmaceutical industry experts, including project managers to conduct this study.
3	Clauson et al. [12]	Using Blockchain technology, the study explores several difficulties (such as product identity, traceability, verification, detection, and etc) as well as prospects for improvement in the healthcare supply chain.
4	Tseng et al. [13]	The system's objective is to reduce the likelihood that fake medications will enter the supply chain for real ones. The double-spending prevention feature of the Gcoin Blockchain was used by the authors of this study to address the issue of fake medications. The Gcoin Blockchain has created and is maintaining an immutable, transparent, and secure database of drug supply chain transaction data that is consensus driven.
5	Hossein et al. [14]	The authors created a Blockchain-based architecture that uses multiple system miners to validate and protect patient data in the healthcare industry. Also, investigated several barriers to using Blockchain in IoT to protect patients' privacy. Concerns expressed included network overhead imposed by the Proof of Work consensus technique and a limited number of transactions recorded in the Blockchain network.
6	Bryatov et al. [15]	A pharmaceutical supply chain architecture is built using the Blockchain Hyperledger Fabric technology. They have highlighted drug counterfeiting as a severe problem in the supply chain and proposed a comprehensive plan to address it.
7	Jamil et al.[16]	According to the authors, the pharmaceutical supply chain's safety has become a serious concern to public health. Using Hyperledger Fabric, they demonstrated pharmaceuticals supply chain management. They also created a smart contract to allow patients to obtain electronic prescription data and electronic health information for a limited period.
8	Drosatos et al. [17]	Provide a thorough overview of the scope and constraints of Blockchain technology in the biological field. Most research focuses on how to integrate, maintain the integrity of, and control access to patient data related to health records. Medical research, clinical trials, the pharmaceutical supply chain, and medical insurance are just a few of the other interesting and cutting-edge applications that are emerging.
9	Yang et al. [18]	Presents an architecture that integrates Blockchain technology into global electronic health records with the use of smart contracts. The proposed system is practical for health providers to implement, without affecting record management effectiveness and interoperable with current e-healthcare systems.
10	Jayaraman et al. [19]	Highlights the potential benefits of combining IoT and Blockchain Technology for the healthcare supply chain. The study investigated how IoT-based Blockchain design, with its smart contract's capability, can address challenges and problems in the healthcare supply chain, including product recalls, supply constraints, expiry monitoring, and fake goods.
11	Tijan et al. [20]	This article delves into the application of Blockchain technology in logistics and supply chain management. Blockchain technology could aid in a variety of supply chain tasks such as tracking objects, tracking orders, vouchers, bills, and transactions, and so on.
12	Abou-Nassar et al. [21]	Proposed a Blockchain-based Decentralized Interoperable Trust framework (DIT) for a healthcare IoT system using smart contracts to boost trust. To ensure trustworthy communication, the system leverages a ripple chain, which verifies nodes depending on underlying interoperable structure.
13	Fekih et al. [22]	An overview of blockchain, particularly as it relates to healthcare, is provided in this article. Electronic Medical Records, Remote Patient Monitoring, Pharmaceutical Supply Chain, Health Insurance Claims, and other healthcare-related use cases and challenges were highlighted.
14	Reda et al. [23]	The healthcare and pharmaceutical supply chain architecture described in this article uses blockchain technology to ensure that real medications get to the people who need them most.
15	Y. L. Chang et al. [24]	Analysed blockchain applications in the maritime, transportation, food, pharmaceutical, and manufacturing supply chains to highlight the key challenges for blockchain implementation.
16	Houtan et al. [25]	Proposed a new model based on the Ethereum network and patient health records. Study includes patients' digital identity, records management, patient data, and decentralised applications for autonomous clinical operation.
17	Alghazwi et al. [26]	The literature on the use of blockchain for genome. They divided searches into commercial and non-commercial categories and predicted several challenges, including constraints to Implementation, interoperability, smart contract security, data privacy, and verifiability, among others.
18	Xiao et al. [27]	To replace the traditional healthcare system, researchers created a consortium Blockchain-based health chain. A consortium of hospitals, insurance companies, and government agencies that may be able to solve the traditional supply chain problems.
19	Cerny et al. [28]	General overview of the challenges associated with the use of blockchain technology in the supply chain. The article makes a distinction between conventional supply chains and supply chains built on blockchain technology. The lack of traceability, a lack of real-time information, the provenance of commodities, counterfeit goods, and other issues related to supply chain.
20	Sunmola et al. [29]	The study examined two different case studies to conduct a literature review on the application of Blockchain technology in traditional supply chains and its deployment in pre-adoption, adoption, and post-adoption stages.
21	Musamih et al. [30]	Authors demonstrated a Blockchain-based drug traceability solution for pharmaceutical supply chain through built in app DApp (Decentralized application) using various Ethereum smart contracts for permission. As a system stakeholder, they followed FDA (Food and Drug Administration) standards and regulations.

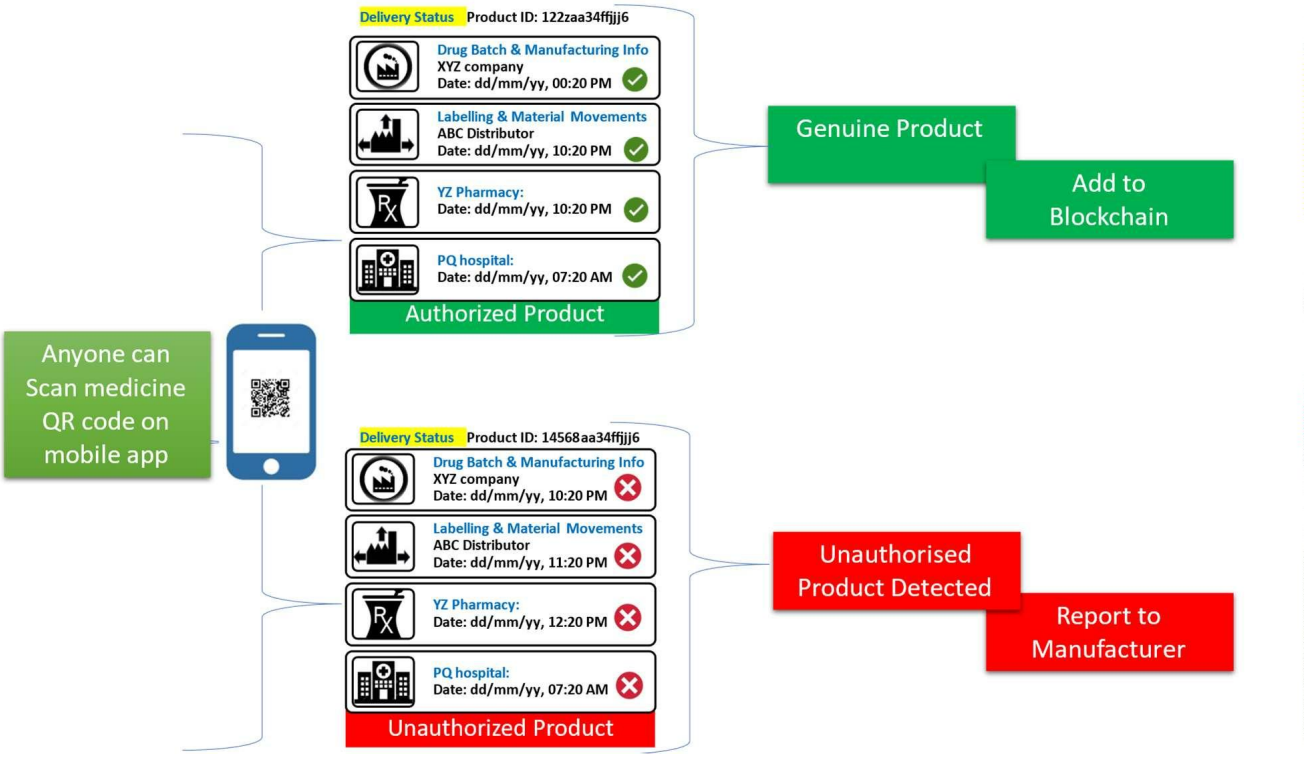

Figure 3: Product Traceability by Patient

chain information network. A one-of-a-kind platform designed with the following goals in mind to create a resilient blockchain network where:

- Supply Chain Concerns and Importance: One out of every ten pharmaceutical products sold in developing nations is fake, costing the region of SEA alone an estimated 2.6 billion USD in lost revenue every year, in addition to posing serious risks to patient safety.
- Pharmaceutical Industry Traceability: Grey markets or parallel imports of drugs are common. Beyond shrinking profit margins for pharmaceutical companies, the greater risks come from endangering public health by failing to comply with regional regulatory approval and labelling requirements.
- Margin erosion because of supply chain inefficiencies: Due to inefficient supply chains and inadequate storage conditions, the pharmaceutical industry loses an average of 4.5percent of its potential revenue.
- Inflated costs and a long-time lag for product recalls: In the last ten years, the average product recall has cost medical device manufacturers USD 10 million (excluding brand damage).
- Harsher penalties and stricter health policies regarding patient safety: Authorities around the world are increasing their scrutiny to ensure that supply chain practices do not jeopardise patient safety.

5.1 Collaboration Challenges with Information Exchange:

Challenge 1: Due to a lack of information and communication between supply chain parties and the lack of a data transfer mechanism, illegal products from outside the system may enter the system.

Challenge 2: Even when information is transmitted, activities are not consistently associated with product / package identities, limiting the effectiveness of sharing. In a system with interconnected feedback loops, efforts to optimise the supply chain are hampered by a lack of end-to-end information.

Challenge 3: Patients lack access to and no way to utilise the supply chain's information regarding product movement and provenance.

5.2 eZTracker Solution to challenges

eZTracker is a blockchain-based solution that gives pharmaceutical manufacturers transparency and traceability over their goods' movements throughout the distribution network. eZTracker turns patients' mobile devices into instant validation tools by tracking the unique QR code. Within seconds, a medication's code can be traced back to its manufacturer and country of origin,

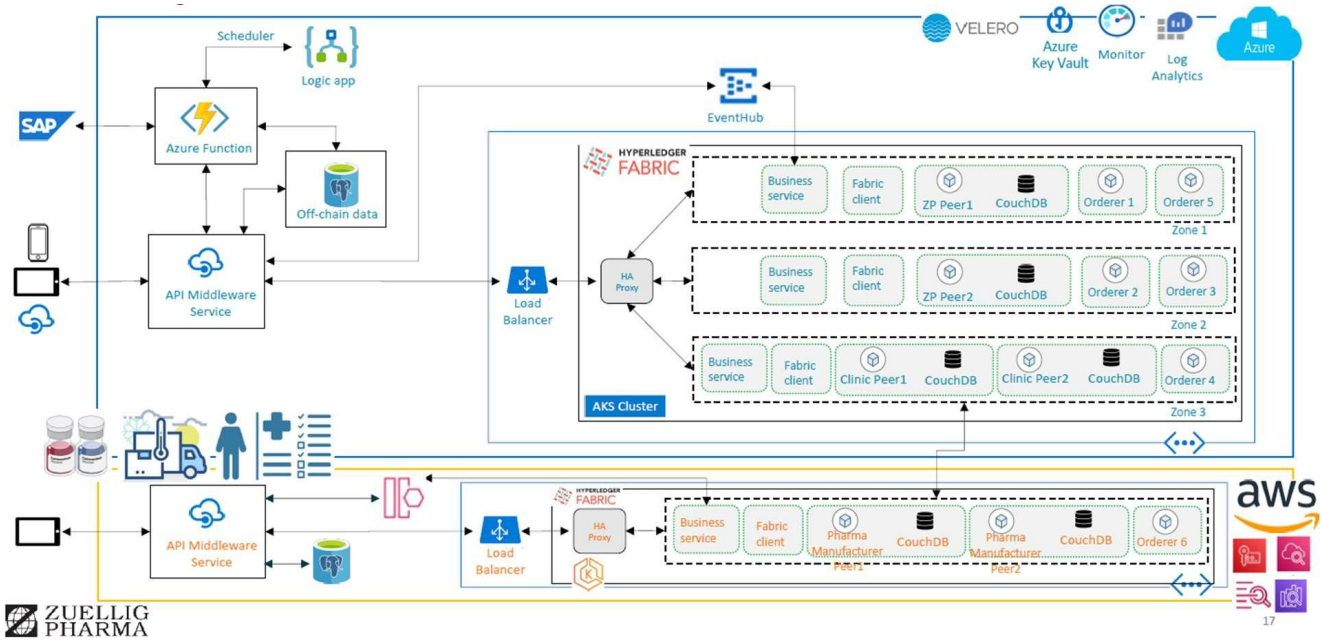

Figure 4: Zuellig Pharma Drug Traceability Blockchain Architecture [31]

which enables them to confirm the provenance and authenticity of their purchase, raising the bar for compliance and quality control to increase patient safety. Zuellig Pharma [31] has designed a material tracker (Fig. 4.) using Hyperledger blockchain technology in which the manufacturer shares material information, including batch information, expiry data, and all other data, with the blockchain that fits the evidence for traceability purposes. Now, this data will be shared along with the blockchain network with all the participants, including the distributor (like Azure Farmer or the other distributor, hospitals, clinics, as well as the other end users). So, when the product reaches the warehouse of Pharma Company, they will also feed in more information in the blockchain, like the shipping date of the medicine to the client, to the hospital, or to the clinic. Zuellig Pharma blockchain also manages the repo repository by storing patient information and patient vaccination details; some details are not shared in the blockchain because of privacy and confidentiality. Salient Features of [31] Participants host and operate their own "Node," which keeps their data safe in their own surroundings.

- Before being fed into the Node, every data point on product movements is confirmed by Smart Contracts and heavily encrypted.
- Participants can choose what data on their Node is recorded on the ledger ("on-chain") and what information is accessible to others.
- Smart Contracts and APIs allow users to "virtually" query ledger data across Nodes without transferring real data.

6 Blockchain SCMS for COVID-19 Vaccine Distribution

Blockchain technology may be the best option for managing COVID-19 vaccine distribution. An efficient allocation of a COVID-19 vaccine would necessitate global agreement on its delivery as well as a transparent, verifiable, and timely supply management system. Blockchain technology may be appropriate to handle such a difficult task, letting all countries and participating associations to be nodes in a network that can visualise immutable and real-time records [32]. The system could keep tabs on important details like vaccine production, distribution, and stock, as well as vaccine-related supplies (like needles, glass vials, and refrigeration units), both within and between nations. It could also keep tabs on the vaccine's quality by keeping track of its batch number, producer, expiration date, and temperature control. To minimise loss and waste, the system should also enable measurement of these two factors.

Blockchain technology, when combined with internet of things ('IoT') technology, could also be used to monitor the COVID-19 vaccine rollout [33](e.g. temperature sensors). Because each vaccination has varied storage needs, temperature and storage duration monitoring is crucial for the COVID-19 vaccine distribution chain. Temperature and other sensitive data could be tracked using blockchain technology throughout vaccination batch shipping and storage. The system would function by placing smart IoT sensors on shipping containers that would gather, store, and transfer data to the blockchain. Other authorised parties could then instantly examine this information on the blockchain, allowing hospitals, distributors, and regulators to confirm that the vaccinations were carried and stored securely and effectively. Many additional possible benefits of blockchain

in the context of pharmaceutical supply chains include the ability to locate problems, limitations, and restrictions rapidly and effectively, as well as eliminate the possibility of double computation through instantaneous transactions. As previously discussed, blockchain could help with quickly recognising troublesome products (such as defective, inaccurately stored, or counterfeit products) and efficiently expelling them from the supply chain.

7 Benefits of Blockchain in Pharmaceutical Supply Chain Management System

- Material Traceability for Pharma Manufacturers: Using blockchain technology, key farmer manufacturers can track the products from the plant down to the patient. Other things like managing inventory visibility and auto-replenishments are basically ways to strengthen trust and really allow them to give a stamp of approval that the products that they have are going through an easy tracker. Customers are assured that these are genuine products; they've been through a genuine supply chain, and they've been handled in the correct way. Block chain also helps in reducing waste and cost with higher demand and inventory visibility. Strengthen brand trust and reduce revenue loss by identifying "grey trade" occurrences.
- Quality Assurance for Patients: Blockchain provides comprehensive traceability from production to the point of reaching the patient, effectively preventing the introduction of counterfeit drugs or medical devices into the ecosystem. In cases where targeted recalls or inspections are necessary, blockchain facilitates swift and precise actions. Furthermore, quality parameters are documented by certifying agencies on the shared ledger, significantly reducing the risk of data tampering. Thus, the prescriber of the drug can verify it at any time, and people will have the right drugs anytime they need them, building confidence that they can go ahead and take that genuine medication, but also the quality. Thus, block chain empowers patients with the quality-related data of each box of medication, creating a sense of security that medication is quality-assured and genuine. Allow for more effective and accurate adverse event reporting and product recalls.
- Efficiency for Healthcare Organizations: Generate business efficiencies by minimizing inefficiencies in inventory management. Allow for more efficient and secure payment processing for pharmaceutical companies and other sub-distributors and wholesalers.

8 Results and Discussion

The pharmaceutical supply chain faces challenges such as counterfeit drugs, inefficient distribution, and quality maintenance. Numerous studies [7, 10-31] have been conducted to resolve this with the help of blockchain technology by ensuring transparency, traceability, and security throughout the supply chain process. With blockchain, each transaction is recorded on an immutable ledger, addressing issues like counterfeit drug introductions and inefficient recalls. The use of Hyperledger Fabric technology, Hyperledger Besu Network, and initiatives like Zuellig Pharma's eZTracker blockchain solutions provide transparency and traceability, enabling manufacturers to track product movements and consumers to verify the authenticity of their medications. By utilising Hyperledger blockchain technology, eZTracker ensures the integrity of data related to product movements, batch information, and expiration dates, enhancing traceability and accountability across the supply chain. In terms of COVID-19 vaccine distribution, blockchain provides an effective and transparent alternative for managing vaccine allocation and supply chain logistics. Real-time monitoring of temperature-sensitive vaccinations is now possible thanks to the integration of IoT technology and blockchain, ensuring adherence to storage regulations and minimising waste. Furthermore, blockchain enables the fast identification of defective items, which improves the overall safety and efficiency of pharmaceutical supply chains. Overall, blockchain technology offers various advantages for pharmaceutical supply chain management, such as increased traceability, quality assurance, and operational efficiency. By adopting blockchain-based systems like eZTracker, stakeholders may minimise risks, increase transparency, and assure the supply of safe and legitimate pharmaceuticals to patients worldwide by just scanning through the mobile app. Thus, these technological advancements significantly reduce counterfeit medicine and provide patients with legitimate drug supply information.

9 Conclusion

Blockchain qualities like decentralisation, immutability, increased security, and distributed ledgers allow for the safe traceability of medications from producers to end-user patients, lowering the possibility of counterfeit drugs entering the market. The paper discusses various architectural advancements in blockchain technology that can be used in the pharmaceutical supply chain to reduce counterfeit medicine. One of the proposed solutions is for consumers, i.e., patients may use smartphone applications to scan QR codes on pharmaceuticals to learn about their origins, production information, and supply chain trip, boosting confidence and trust in pharmaceutical supply chains. Blockchain's immutability and decentralisation provide data integrity and security, providing answers to issues such as counterfeit medication prevention, product distribution, and erroneous stock data. The paper also reviews Zuellig Pharma's eZTracker technology and demonstrates blockchain's disruptive potential by enabling transparency and traceability across the supply chain. Looking ahead, blockchain technology promises to revolutionise healthcare supply chain management, notably in COVID-19 vaccine delivery, by enabling real-time tracking, monitoring, and verification to guarantee equal access and minimise waste.

Competing Interests

The authors declare that they have no conflict of interest.

References

[1] David Chaum. Blind signatures for untraceable payments. In David Chaum, Ronald L. Rivest, and Alan T. Sherman, editors, *Advances in Cryptology*, pages 199–203, Boston, MA, 1983. Springer US. ISBN 978-1-4757-0602-4.

[2] David Chaum and Sandra Roijakkers. Unconditionally-secure digital signatures. In *Advances in Cryptology-CRYPTO'90: Proceedings 10*, pages 206–214. Springer, 1991.

[3] Adam Back et al. Hashcash-a denial of service counter-measure. *Available at : http://www.hashcash.org/papers/hashcash.pdf*, 2002.

[4] Nick Szabo. Bit gold: towards trust-independent digital money. *Recuperado de: https://web.archive.org/web/20140406003811/http://szabo.best.vwh.net/bitgold.html*, 1998.

[5] Wei Dai. B-money-an anonymous, distributed electronic cash system, 1998.

[6] Satoshi Nakamoto. Bitcoin: A peer-to-peer electronic cash system. *Available at https://bitcoin.org/bitcoin.pdf*, 2008.

[7] Mueen Uddin, Khaled Salah, Raja Jayaraman, Sasa Pesic, and Samer Ellahham. Blockchain for drug traceability: Architectures and open challenges. *Health informatics journal*, 27(2):14604582211011228, 2021.

[8] Sanjeev Kumar Dwivedi, Ruhul Amin, and Satyanarayana Vollala. Blockchain based secured information sharing protocol in supply chain management system with key distribution mechanism. *Journal of Information Security and Applications*, 54:102554, 2020.

[9] Seyednima Khezr, Md Moniruzzaman, Abdulsalam Yassine, and Rachid Benlamri. Blockchain technology in healthcare: A comprehensive review and directions for future research. *Applied sciences*, 9(9):1736, 2019.

[10] Haoyan Wu, Zhijie Li, Brian King, Zina Ben Miled, John Wassick, and Jeffrey Tazelaar. A distributed ledger for supply chain physical distribution visibility. *Information*, 8(4):137, 2017.

[11] Magnus Lyster Jochumsen and Atanu Chaudhuri. Blockchain's impact on supply chain of a pharmaceutical company. In *EUROMA Conference*, volume 6, 2018.

[12] Kevin A Clauson, Elizabeth A Breeden, Cameron Davidson, and Timothy K Mackey. Leveraging blockchain technology to enhance supply chain management in healthcare:: An exploration of challenges and opportunities in the health supply chain. *Blockchain in healthcare today*, 2018.

[13] Jen-Hung Tseng, Yen-Chih Liao, Bin Chong, and Shih-wei Liao. Governance on the drug supply chain via gcoin blockchain. *International journal of environmental research and public health*, 15(6):1055, 2018.

[14] Koosha Mohammad Hossein, Mohammad Esmaeil Esmaeili, Tooska Dargahi, et al. Blockchain-based privacy-preserving healthcare architecture. In *2019 IEEE Canadian conference of electrical and computer engineering (CCECE)*, pages 1–4. IEEE, 2019.

[15] SR Bryatov and AA Borodinov. Blockchain technology in the pharmaceutical supply chain: Researching a business model based on hyperledger fabric. In *Proceedings of the International Conference on Information Technology and Nanotechnology (ITNT), Samara, Russia*, volume 10, pages 1613–0073, 2019.

[16] Faisal Jamil, Lei Hang, KyuHyung Kim, and DoHyeun Kim. A novel medical blockchain model for drug supply chain integrity management in a smart hospital. *Electronics*, 8(5):505, 2019.

[17] George Drosatos and Eleni Kaldoudi. Blockchain applications in the biomedical domain: a scoping review. *Computational and structural biotechnology journal*, 17:229–240, 2019.

[18] Guang Yang, Chunlei Li, and Kjell E Marstein. A blockchain-based architecture for securing electronic health record systems. *Concurrency and Computation: Practice and Experience*, 33(14):e5479, 2021.

[19] Raja Jayaraman, Khaled Salah, and Nelson King. Improving opportunities in healthcare supply chain processes via the internet of things and blockchain technology. *International Journal of Healthcare Information Systems and Informatics (IJHISI)*, 14(2):49–65, 2019.

[20] Edvard Tijan, Saša Aksentijević, Katarina Ivanić, and Mladen Jardas. Blockchain technology implementation in logistics. *Sustainability*, 11(4):1185, 2019.

[21] Eman M Abou-Nassar, Abdullah M Iliyasu, Passent M El-Kafrawy, Oh-Young Song, Ali Kashif Bashir, and Ahmed A Abd El-Latif. Ditrust chain: towards blockchain-based trust models for sustainable healthcare iot systems. *IEEE access*, 8:111223–111238, 2020.

[22] Rim Ben Fekih and Mariam Lahami. Application of blockchain technology in healthcare: a comprehensive study. In *The Impact of Digital Technologies on Public Health in Developed and Developing Countries: 18th International Conference, ICOST 2020, Hammamet, Tunisia, June 24–26, 2020, Proceedings 18*, pages 268–276. Springer, 2020.

[23] Moulouki Reda, Dominique Bernard Kanga, Taif Fatima, and Mohamed Azouazi. Blockchain in health supply chain management: State of art challenges and opportunities. *Procedia Computer Science*, 175:706–709, 2020.

[24] Yanling Chang, Eleftherios Iakovou, and Weidong Shi. Blockchain in global supply chains and cross border trade: a

critical synthesis of the state-of-the-art, challenges and opportunities. *International Journal of Production Research*, 58 (7):2082–2099, 2020.

[25] Bahar Houtan, Abdelhakim Senhaji Hafid, and Dimitrios Makrakis. A survey on blockchain-based self-sovereign patient identity in healthcare. *IEEE Access*, 8:90478–90494, 2020.

[26] Mohammed Alghazwi, Fatih Turkmen, Joeri Van Der Velde, and Dimka Karastoyanova. Blockchain for genomics: a systematic literature review. *Distributed Ledger Technologies: Research and Practice*, 1(2):1–28, 2022.

[27] Yonggang Xiao, Bin Xu, Wenhao Jiang, and Yunjun Wu. The healthchain blockchain for electronic health records: development study. *Journal of medical Internet research*, 23(1):e13556, 2021.

[28] Mikuláš Černỳ, Marián Gogola, Stanislav Kubal'ák, and Ján Ondruš. Blockchain technology as a new driver in supply chain. *Transportation Research Procedia*, 55:299–306, 2021.

[29] Funlade T Sunmola, Patrick Burgess, and Albert Tan. Building blocks for blockchain adoption in digital transformation of sustainable supply chains. *Procedia Manufacturing*, 55:513–520, 2021.

[30] Ahmad Musamih, Khaled Salah, Raja Jayaraman, Junaid Arshad, Mazin Debe, Yousof Al-Hammadi, and Samer Ellahham. A blockchain-based approach for drug traceability in healthcare supply chain. *IEEE access*, 9:9728–9743, 2021.

[31] Daniel Laverick and Zhang Haisheng. A blockchain-enabled solution to drive material traceability along the pharmaceutical supply chain in asia. pages 1–20. ., 2021.

[32] Manan Shukla, Jianjing Lin, and Oshani Seneviratne. Blockiot: blockchain-based health data integration using iot devices. In *AMIA Annual Symposium Proceedings*, volume 2021, page 1119. American Medical Informatics Association, 2021.

[33] H Schofield and L Thasarathakumar. Blockchain, covid-19 and the pharmaceutical supply chain. *PharmExec*, 2021.

El Cezeri
Journal of Science and Engineering
ISSN: 2148-3736

Research Article

Neutronic Analysis on Molten Salt Reactor (MSR) Using OpenMC Code With Variations of Geometry Core Fueled By LiF-BeF_2-UF_4

Ratna Dewi Syarifah[1a], Briyanti Adelia Putri[1b], Indarta Kuncoro Aji[2c] Ahmad Muzaki Mabruri[3d]

[1] Physics Department, University of Jember, Jember, Indonesia
[2] Molten Salt Lab. Inc., Kyushu University, Kasuga, Fukuoka, Japan
[3] Department of Nuclear Science and Engineering, Bandung Institute of Technology, Bandung, Indonesia

rdsyarifah.fmipa@unej.ac.id

DOI : 10.31202/ecjse.1364028
Received: 24.09.2023 Accepted: 24.014.2024
How to cite this article:
Ratna Dewi Syarifah, Briyanti Adelia Putri, Indarta Kuncoro Aji, Ahmad Muzaki Mabruri, " Neutronic Analysis on Molten Salt Reactor (MSR) Using OpenMC Code With Variations of Geometry Core Fueled By LiF-BeF_2-UF_4", El-Cezeri Journal of Science and Engineering, Vol: 11, Iss:2, (2024), pp.(152-159).
ORCID: [a]0000-0001-9110-2093; [b]0009-0009-4624-0636. [c]0000-0002-6936-9178; [d]0000-0001-9383-8424;

Abstract : Nuclear Power Plant can produce electricity more efficiently and have low carbon emissions. The nuclear reactor used in this study is the MSR (Molten Salt Reactor) FUJI-12. This study aims to conduct an analysis neutronics on MSR FUJI-12 by varying the geometry shape of the reactor core and finding the most effective geometry core to use in MSR. The material used in this study is a mixture of LiF-BeF_2-UF_4 molten salts. This study uses OpenMC code with nuclear data library ENDF/B VIII.1. The shapes of the geometry core that will be compared are, pancake, balance, and tall. The three geometry core shapes will then be varied into seven kinds. The results show that the geometry of the core is very influential on the reactivity of a nuclear reactor. The value for all geometry core variants at the beginning of the operating reactor is in a supercritical condition and it will be a critical or subcritical condition at the end of the reactor's operating life. Balance and tall 1 variants have a high on distribution neutron flux and fission rate. The Balance variant also produces the smallest mass of plutonium nuclides. The neutronic analysis that has been carried out show that the balance variant is the optimal geometry core design that can be used on the MSR FUJI-12.

Keywords : Molten Salt Reactor, Monte Carlo, OpenMC, Geometry Core.

1 Introduction

The use of electrical energy in Indonesia continues to increase every year. Electricity consumption per capita in Indonesia in 2020 is 1.088 GWh and in 2021 is 1.122 GWh [1]. Most of Indonesia's electricity nowadays uses fossil fuels (coal). Around 87% of total electricity production in Indonesia in 2020 come from a coal [2]. Using coal as a fuel will have a negative impact on the environment. The negative impact on the environment results both from the mining and from its [3].

Nuclear Power Plant is an alternative to providing electricity that can produce a larger and more stable electricity capacity. Nuclear energy is sustainable because it has least polluting and the lowest environmental impact [4].The fission reaction process in a nuclear reactor releases large amounts of energy in the form of heat, which is then used to produce steam and drive turbines to generate electricity [5]. Nuclear Power Plants have experienced many developments from Generation I to Generation IV. MSR is a type of Generation IV nuclear reactor design that uses a mixture of molten salts as both fuel and coolant [6]. MSR FUJI-12 is a nuclear reactor design developed in Japan and is considered more economical because it can be mass-produced and does not require large areas of land [7]. The FUJI-12 reactor core consists a hexagonal cylinder with a flow channel for fuel made from graphite in the middle [8].

Neutronic analysis of MSR has been analysed. The research in [9] using LiF-BeF_2-ThF_4-UF_4 as a fuel showed that MSR FUJI-12 can achieve its criticality with the ^{233}U concetration in the fuel of 0.34% or more. The study in [10] that use ^{235}U on LiF-BeF_2-ThF_4-UF_4 showed that the miniFUJI MSR reactor could gain its criticality condition for 1.96% of UF_4 with ^{235}U enrichment at the smallest amount 95% in the 50 MWth. The study in [11] showed that the composition of LiF-BeF_2-UF_4 can be use for MSR fuel. The research in [12] showed an neutronic analysis on MSR FUJI-12 using ^{235}U as a fissile material in LiF-BeF_2-UF_4 fuel. There are three eutectic compositions of fuel used in this study. The fuel 1 has 48% LiF-51,5% BeF_2-0.5% UF_4, the fuel 2 has 69% LiF-23% BeF_2-8% UF_4, while the fuel 3 has 70% LiF-18% BeF_2-12% UF_4. The result showed that the eutectic composition of LiF-BeF_2-UF_4 in fuel 2 and fuel 3 can potentially be used as a liquid salt fuel mixture in MSR FUJI-12 with an operating power of 350 MWt.

The geometry core of the reactor is one of the important things when analyzing a nuclear reactor. Geometry shape of the

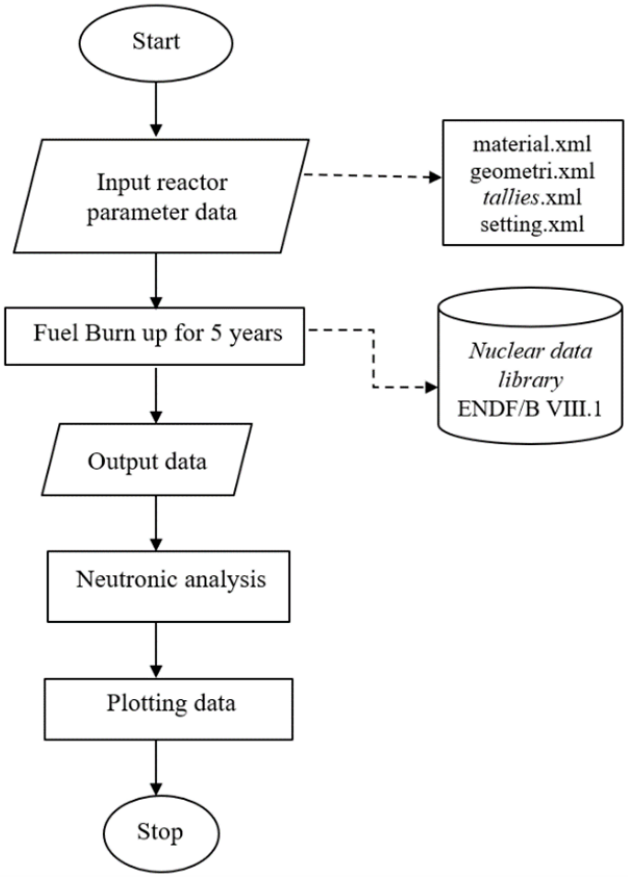

Figure 1: Research Procedure

core will determine the graph of the value of and the reactivity value of a reactor. The research [13] on Gas Cooled Fast Reactor used 3 geometry type, i.e. pancake, balance, and tall. The result showed that the pancake is an effective type used in Gas Cooled Fast Reactor. The paper [14] presents the neutronic analysis of core shape in a Small Molten Salt Fast Reactor. The geometry core shape that used are pancake, balance, and tall. The result in 50 MWth showed that balance is the most effective size, while 20 and 30 MWth showed that pancake is the most effective size. This study aims to conduct an analysis of neutronics on MSR FUJI-12 by varying the geometry shape of the reactor core and finding the most effective geometry core to use in MSR using OpenMC code.

2 Methodology

The study of neutronic analysis on MSR FUJI-12 with variations geometry core was conducted using OpenMC code developed by Computational Reactor Physics Group (CRPG) on Massachusetts Institute of Technology (MIT) and nuclear data library ENDF/B VIII.1. The research procedure is shown in Figure 1.

OpenMC is an open-source Monte Carlo particle transport code. OpenMC is capable to simulating all nuclear reactions producing secondary neutrons, including (*n, 2n*), (*n, 3n*), fission, and level inelastic scattering. The data of interactions neutron with nuclei are represented in ACE format, and it can be generated with the NJOY nuclear data processing system to convert raw ENDF/B data into a representation that is suitable for use in a Monte Carlo code [15].

The Monte Carlo method is one of the numerical methods that can be used to solve the neutron transport equation. Monte Carlo method simulates neutron transport as a stochastic process. The neutron path starts from the neutron source in the nuclear reactor, most are fission sources. Fission sources have energy distribution in the form of a fission spectrum in space with an isotropic distribution direction. The probability that a neutron has a collision at a distance s along the flight path is:

$$T(s) = \Sigma_{\mathrm{t}}(s) \exp[-\int_0^s \Sigma_{\mathrm{t}}(s')\, ds'] \tag{1}$$

The collision occurs in the n th region at a distance is:

$$s'_{\mathrm{n}} = (1/\Sigma_{\mathrm{t}})(-ln\lambda - \Sigma_{j=1}^{n} \Sigma_{\mathrm{t\,j}} s_{\mathrm{s_j}} \tag{2}$$

Table 1: Spesification of MSR FUJI-12

Parameters	Value
Power	350 MWt
Average power density	7 kWt/liter
Burn up	5 years
Fuel Salt Composition:	
LiF	69%
BeF_2	23%
UF_4	8%
Density	2.9 gr/cm^3
Thermal input	840 K

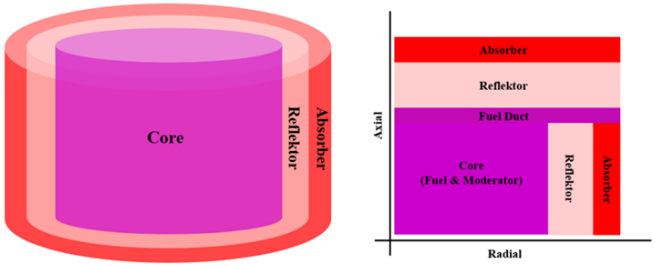

Figure 2: Constituent component of core

The Monte Carlo method requires several repetitions so that the simulated phenomena can be described completely and realistically [16].

The molten salt fuel mixture on the MSR must be in the eutectic composition. The eutectic composition is the mixing point of a chemical compound with the lowest temperature. The eutectic temperature of a mixture can be achieved by determining the right composition, so that the compound mixture can be used as a fuel in MSR. ^{235}U was used as a fissile material and ^{238}U as a fertile material. The specification of MSR FUJI-12 shown in Table 1.

The MSR FUJI-12 composed a core, reflector, absorber, and fuel duct. The active core is where the fission chain reaction happens, which consists of fuel and moderator. The fuel duct is located at the upper and lower active as a fuel path. The fuel duct that used in this research have a 2.5 cm of thickness. The active core is protected by reflectors and absorbers on the radial and axial boundaries. The reflector serves to reflect the neutrons into the active core of the reactor. The absorber functions as a neutron absorber from the reactor's active core. This research use reflectors with a thickness of 60 cm in the axial and 50 cm in the radial, while the absorber has the same size in axial and radial with a thickness of 20 cm. The energy filter that applied in this research is about 0 – 20 MeV. The design of MSR FUJI-12 is shown in Figure 2.

The moderator material is made of graphite so that the energy of the neutrons remains in thermal energy. The reflector is also made of graphite which serves to reflect the neutrons. Graphite has the characteristics of a stable material in high temperature and radiation environments and is able to conduct heat well. The absorber is made of boron carbide that has a function as a reactor's neutron absorber and protector. The absorber that used in this paper

The geometry shapes of the core that will be compared are pancake (diameter > height), balance (diameter = height), and tall (diameter < height). Then the three geometry core shapes will be varied into seven kinds: pancake 1, pancake 2, pancake 3, balance, tall 1, tall 2, and tall 3. Figure 3 show variations of the geometry core shapes. The amount of fuel volume fraction, input power, and percentage of fissile material has the same value, while the volume of the reactor core is cultivated almost the same. The value of these aspects is made the same to emphasize the output results comparison of the geometry core. The size and volume of each variant of the geometry core shown in Table 2.

The MSR FUJI-12 core consists of a hexagonal prism assembly. The assembly ring arrangement consists of the inner ring and *n* th ring. The inner ring is the innermost part of the assembly arrangement which consists of one hexagonal prism pin. The *n* th ring is the ring that surrounds the inner ring. Figure 4 shown the arrangement of assembly ring on MSR FUJI-12.

The total number of rings used in each variant of the geometry core are varies. Determination of the number of rings refers

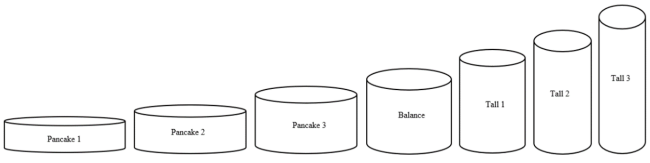

Figure 3: Variations of the geometry core shapes

Table 2: Size variation of the geometry core

Geometry	Diameter (cm)	Height (cm)	Ratio (H/D)
Pancake 1	514.6	241.68	0.4
Pancake 2	471	288.495	0.6
Pancake 3	428.5	348.561	0.8
Balance	400	400	1
Tall 1	354.246	510	1.4
Tall 2	310	665.973	2.1
Tall 3	270.9	872.092	3.2

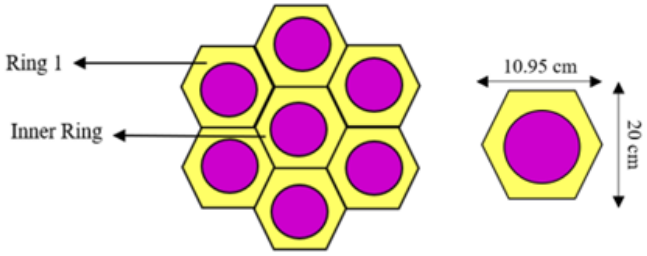

Figure 4: Arrangement of assembly pin fuel

to the size of the diameter and height of the reactor core. The pin fuel has a pitch diameter of 20 cm and the diameter of the duct is 10.95 cm. The all variant geometry core design of MSR FUJI-12 on radial axis shown in Figure 5. Table 3 shown the specification of pin and assembly.

The formula that used in this study are:

1. Weight Fraction

$$Mass_x = (Mr_x \times mol_x), \quad wo = \frac{Mass_x}{\Sigma_{i=x}^{n} Mass_i} \tag{3}$$

2. Excess Reactivity

$$\rho = \frac{k^{\text{eff}} - 1}{k^{\text{eff}}} \times 100\% \tag{4}$$

2.1 Analysis on effective multiplication factor

DThe effective multiplication factor is a constant that shows the ratio of the number of neutrons produced in one generation divided by the number of neutrons lost due to absorption and leakage in the previous generation. The value of shows the criticality level of a reactor. The value of is expected to be close to critical conditions at the beginning of the operation until the end of the operation so that the fission chain reaction can continue. The effective multiplication factor in each variant of the geometry core shown in Figure 6.

The value of for each variant of the geometry core is in a supercritical condition at the beginning of the operating reactor and will decrease significantly as the reactor's operating period progresses until it enters a critical or subcritical condition state. A decrease in the throughout the reactor's operating life can occur due to reduced fuel nuclides due to the burn up process. The resulting from all variants with the same volume of geometry core has almost the same value. However, the in the tall variant produces a smaller value when compared to the pancake and balance variants.

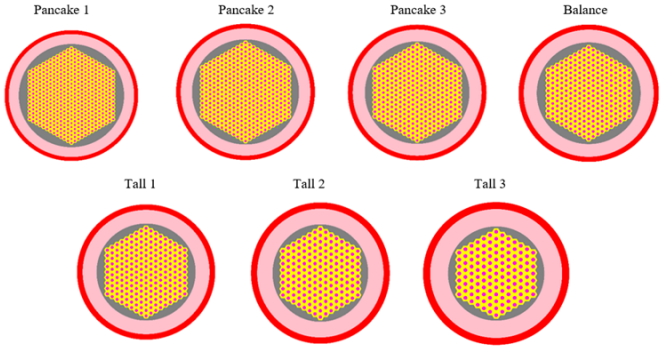

Figure 5: All variants geometry core design of MSR FUJI-12 on radial axis

Table 3: Specification of pin and assembly

Parameter	Value
Diameter of pitch	20 cm
Diameter of duct	10.95 cm
Total rings dan assembly	
· *Pancake* 1	13 *rings* (469 pin)
· *Pancake* 2	12 *rings* (397 pin)
· *Pancake* 3	11 *rings* (331 pin)
· *Balance*	10 *rings* (271 pin)
· *Tall* 1	9 *rings* (217 pin)
· *Tall* 2	8 *rings* (169 pin)
· *Tall* 3	7 *rings* (127 pin)

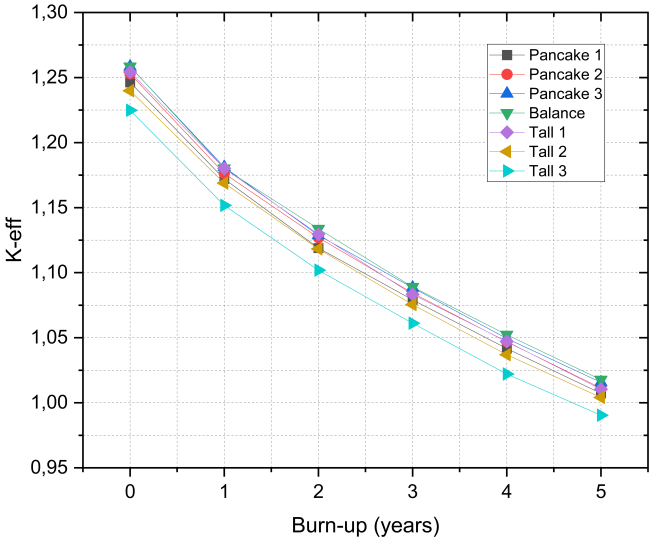

Figure 6: k-eff in each variant of the geometry core

2.2 Analysis on flux neutron and fission rate

The neutron flux is the total distance traveled by all the neutrons per unit volume per unit time. The unit of neutron flux is neutrons/cm^{2}s. The neutron flux distribution is reviewed at the beginning of life (BOL) and the end of life (EOL) of the reactor. A color spectrum describes the distribution of the resulting neutron flux at a specific scale. The red indicates the number of scattered neutrons that occur in the central region. The greenish-yellow color indicates that the distribution of neutrons is moving outwards and away from the central region. At the same time, the blue color indicates that the distribution of neutrons that occur is getting smaller.

Figure 7 shown neutron flux at the beginning of the reactor in the radial direction (XY). Figure 8 shown neutron flux at the end of the reactor in the radial direction (XY). The maximum distribution of neutron flux is in the core area which consists of fuel and moderator. The neutron flux distribution in BOL has a higher absorption area compared to EOL. The balance variant geometry core has the opportunity to be used as an optimal design on MSR FUJI-12. The balance variant has a high neutron flux value and the decrease in neutron flux from the start to the end of the operation is also stable so that the reactor is able to maintain the maximum combustion process.

Fission rate is the rate of fission reaction in a reactor which refers to the production of neutrons per unit time or can be

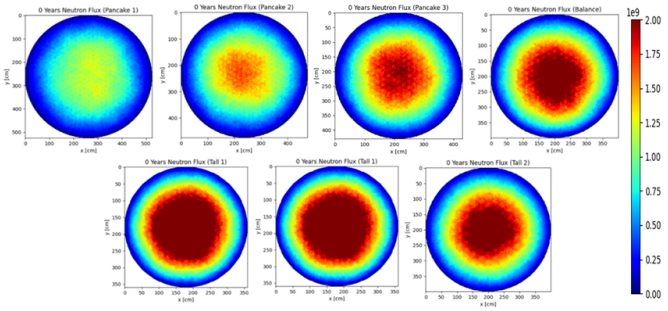

Figure 7: Neutron flux in the radial direction (XY) at the BOL

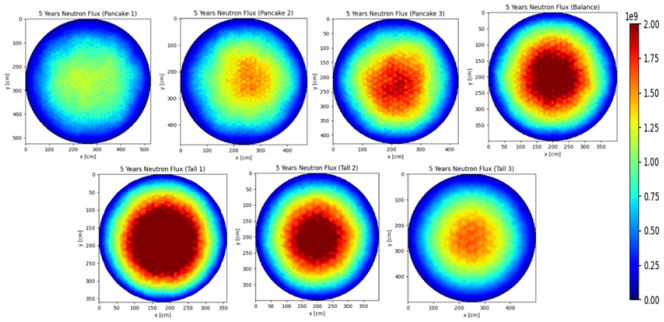

Figure 8: Neutron flux in the radial direction (XY) at the EOL

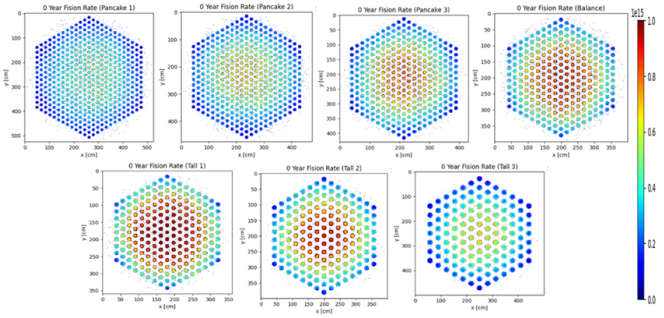

Figure 9: Fission rate in the radial direction (XY) at the BOL

expressed in neutrons/s. The value of the neutron flux affects the fission rate in a nuclear reactor. The fission rate in the reactor is described by the shape of the fuel channels which produce colors according to the level of fission combustion that occurs in the reactor core.

Fission rate is also reviewed at the beginning of life (BOL) and the end of life (EOL) of the reactor. Figure 9 shown a fission rate at the beginning of the reactor operation in the radial direction (XY). Figure 10 shown a fission rate at the end of the reactor operation in the radial direction (XY). Based on the Figure 9 and Figure 10 show that the fission reaction occurs in the fuel region, which also corresponds to the distribution of the neutron flux. The tall 1 and balance variants have a high rate of fission reaction when compared to the other variants.

2.3 Analysis on microscopic cross section

Microscopic cross section is the probability of a neutron experiencing several reactions with a single isotope within a certain range of energy groups. Figure 11 shown a microscopic cross section of ^{235}U. The resonance region refers to the energy range in which there is a significant increase in cross section. The resonance region has an energy characteristic where the nuclide is easily excited. The cross section of neutron absorption that occurs in this energy range indicates is very high fission reaction occurs. When thermal neutrons pass through this resonance region, they are likely to be absorbed by atomic nuclei and cause a sustained fission reaction in the reactor.

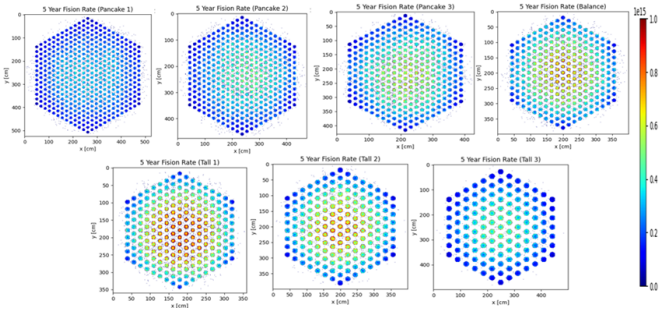

Figure 10: Fission rate in the radial direction (XY) at the EOL

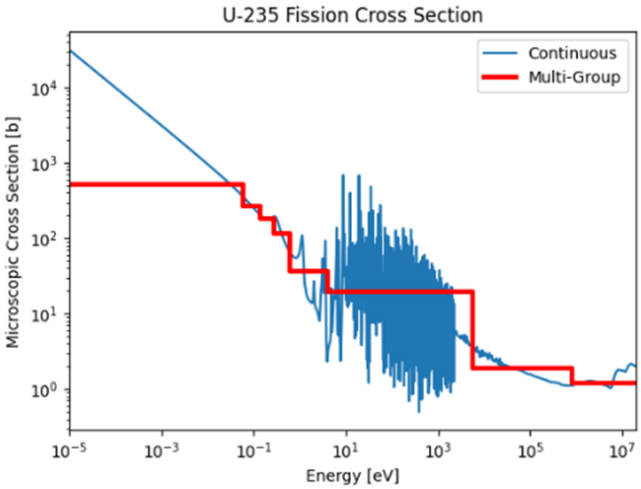

Figure 11: Microscopic cross section of ^{235}U

Table 4: The amount of plutonium remaining at the end of reactor operation

Isotope Pu	Mass (kg) P1	P2	P3	B	T1	T2	T3
^{238}Pu	1.74	1.74	1.73	1.71	1.72	1.73	1.73
^{239}Pu	227.8	227.3	227.2	225.7	225.7	227.6	228.1
^{240}Pu	31.49	31.40	31.52	31.46	31.24	31.41	31.50
^{241}Pu	24.81	24.85	24.84	24.42	24.65	24.85	24.83
^{242}Pu	2.58	2.58	2.58	2.55	2.58	2.58	2.58
Total	288.43	287.93	287.89	285.92	285.95	288.19	288.80

P = Pancake, B = Balance, T = Tail

2.4 Analysis on fission product

The radioactive elements used in this study consists of ^{235}U as a fissile material and ^{238}U as a fertile material. The remaining plutonium fuel from the operation of the MSR FUJI-12 reactor consisted of ^{238}Pu, ^{239}Pu, ^{240}Pu, ^{241}Pu, and ^{242}Pu. The remaining amount of plutonium fuel is obtained from the decay of ^{238}U. Figure 11 is shown the growth of the number of nuclides from ^{235}U, ^{238}U, and plutonium in the geometry core of the balance variant. The mass of uranium has decreased significantly from the beginning of operation to the end of the reactor operation. Decreasing the mass of ^{238}U will have an impact on increasing the number of plutonium nuclides. Table 4 is the amount of plutonium remaining at the end of reactor operation

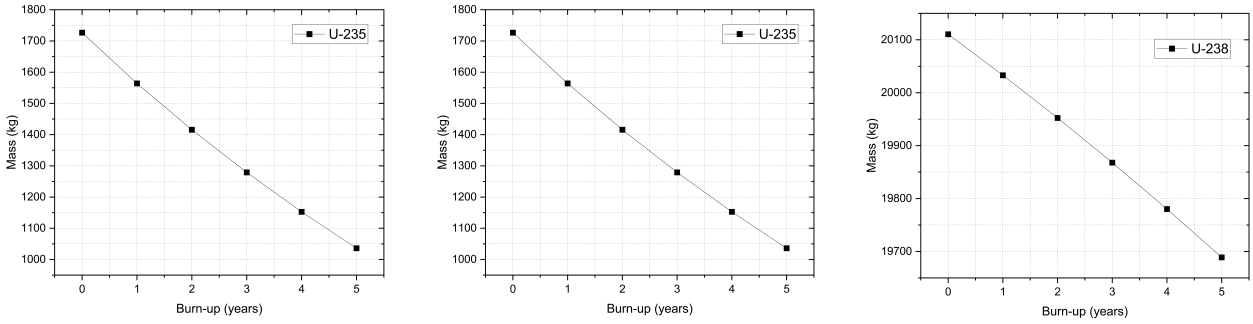

(a) **(b)** **(c)**

Figure 12: (a) Total nuclides of ^{235}U; (b) Total nuclides of ^{238}U; (c) Total nuclides of plutonium

Based on Table 4, ^{238}Pu is the nuclide that produces the least mass while ^{239}Pu has the most mass. It can happen because ^{238}Pu has a shorter half-life than ^{239}Pu. Half-life refers to the time required for half the amount of a radioactive isotope to decompose. Pu-238 which has a shorter half-life than Pu-239 indicates that its radioactive activity is higher. Because it has high radioactive activity, the plutonium residue remaining after use in the reactor tends to be relatively small, thereby reducing the amount of plutonium waste produced. The number of remaining plutonium nuclides at the end of burn up in each variant of the reactor geometry core obtained similar results. However, the balance variant produces the smallest plutonium nuclide mass when compared to the other variants although the difference is very slight.

MSR is the IVth Generation Reactor that was created by emphasizing several aspects, one of the aspects is non-proliferation.

Non-proliferation refers to the efforts to prevent the spread of nuclear weapons used for military purposes. The principle of non-proliferation is to produce less plutonium waste to minimize the use of fuel as a nuclear weapon. This shows that geometry core design of the balance variant is the optimal design for the MSR FUJI-12.

3 Conclusion

The k-eff value for each geometry core variant is in a supercritical condition at the beginning of the operating reactor and significantly decrease as the reactor operating period progresses until at a critical or subcritical condition. The geometry core of the reactor is very influential on the distribution of neutron flux and fission rate. The balance and tall 1 variant have a high distribution of neutron flux and fission rate. The amount of plutonium nuclides resulting from reactor waste in the balance variant produces the least mass. Considering several aspects of the neutronic analysis that has been carried out, the balance variant is the optimal geometry core design that can be used on the MSR FUJI-12.

4 Authors' Contributions

Ratna Dewi Syarifah: Conceptualization, Writing – review & editing, Supervision, Methodology. Briyanti Adelia Putri: Writing – original draft, Visualization. Indarta Kuncoro Aji: Validation, Formal analysis. The authors read and approved the final manuscript. Ahmad Muzaki Mabruri: Validation, review & editing. The authors read and approved the final manuscript.

Competing Interests

The authors declare that they have no competing interests.

References

[1] Direktorat Jenderal Ketenagalistrikan. *Statistik Ketenagalistrikan 2021*. Jakarta, 2022.
[2] BP. *BP Statistical Review of World Energy 2022 (71st Edition)*. London, 2022.
[3] M H Hasan, T M I Mahlia, and N Hadi. A review on energy scenario and sustainable energy in indonesia. *Renewable and Sustainable Energy Reviews*, 16:2316–2328, 2012.
[4] W B Barry, A Alonso, D A Meneley, J Misak, T Blees, and Jan B van Erp. Why nuclear energy is sustainable and has to be part of the energy mix. *Sustainable Materials and Technologies*, 1–2:8–16, 2014.
[5] M Wauran. Peta pembangkit listrik tenaga nuklir (pltn) dunia dan prospeknya. *Jurnal Ilmiah Teknik Energi*, 1(9):83–91, 2009.
[6] J Serp, M Allibert, O Benes, S Delpech, O Feynberg, V Ghetta, D Heuer, D Holcomb, V Ignatiev, J L Kloosterman, L Luzzi, E M Lucotte, J Uhlír, R Yoshioka, and D Zhimin. The molten salt reactor (msr) in generation iv: Overview and perspectives. *Progress in Nuclear Energy*, 77:308–319, 2014.
[7] I K Aji and A Waris. Studi pemanfaatan plutonium sebagai bahan bakar pada molten salt reactor fuji-12. pages 2–6, 2010.
[8] I K Aji, S Pramuditya, A W Novitrian, and D Irwanto. Delayed neutrons effect on power reactor with variation of fluid fuel velocity at msr fuji-12. In *International Conference on Recent Trends in Physics*, pages 1–6, 2017.
[9] A Waris, I K Aji, Novitrian, R Kurniadi, and Z Su'ud. Plutonium and minor actinides utilization in thorium molten salt reactor. In *AIP Conference Proceedings*, volume 1448, pages 115–118, 2012.
[10] I K Aji and A Waris. Preliminary study on weapon grade uranium utilization in molten salt reactor minifuji. In *AIP Conference Proceedings*, pages 57–60, 2014.
[11] L V Jones, D E Etter, C R Hudgens, A A Huffman, T B Rhinehammer, N E Rogers, P A Tucker, and L J Wittenberg. Phase equilibria in the ternary fused-salt system lif-bef2-uf4. *Journal of the American Ceramic Society*, 45(2):79–83, 1962.
[12] A M Mabruri, R D Syarifah, I K Aji, Z Hanifah, A Arkundato, and G Jatisukamto. Neutronic analysis on molten salt reactor fuji-12 using 235u as fissile material in lif-bef2-uf4 fuel. *Eastern-European Journal of Enterprise Technologies*, pages 6–12, 2022.
[13] R D Syarifah, Z Su'ud, K Basar, and D Irwanto. Comparative study on various geometrical core design of 300 mwth gas cooled fast reactor with un-pun fuel long-life without refuelling. In *International Conference on Energy Sciences*, pages 1–5, 2017.
[14] D S Lestari, C Wulandari, A Waris, and S Permana. Neutronic analysis of core shape and h/d ratio in small molten salt fast reactor 20-50 mwth. In *Annual Nuclear Safety Seminar*, pages 170–173, 2021.
[15] P K Romano, N E Horelik, B R Herman, A G Nelson, B Forget, and K Smith. Openmc: A state of the art monte carlo code for research and development. *Annals of Nuclear Energy*, pages 90–97, 2015.
[16] W M Stacey. *Nuclear Reactor Physics: Second Edition*. Wiley VCH Verlag GmbH & Co. KgaA, Weinheim, 2007.

El Cezeri
Journal of Science and Engineering
ISSN: 2148-3736

Research Article

Experimental Investigations on the Drilling Performance of Carbon Nanotubes Reinforced Glass/Epoxy Multi-scale Composites

Murat Koyunbakan[1a], Volkan Eskizeybek[2b], Ali Ünüvar[3c] Ahmet Avcı[4d]
[1] Mechanical Engineering Department, Faculty of Simav Technology, Kütahya Dumlupinar University, Kütahya, Turkiye
[2] Materials Science and Engineering Department, Faculty of Engineering, Çanakkale Onsekiz Mart University, Çanakkale, Turkiye
[3] Industrial Design Department, Faculty of Architecture and Design, İstanbul Ticaret University, İstanbul, Turkiye
[4] Biomedical Engineering Department, Faculty of Engineering, Necmettin Erbakan University, Konya, Turkey

murat.koyunbakan@dpu.edu.tr

DOI : 10.31202/ecjse.1366208
Received: 25.09.2023 Accepted: 19.01.2024
How to cite this article:
Murat Koyunbakan, Volkan Eskizeybek, Ali Ünüvar, Ahmet Avcı, " Experimental Investigations on the Drilling Performance of Carbon Nanotubes Reinforced Glass/Epoxy Multi-scale Composites", El-Cezeri Journal of Science and Engineering, Vol: 11, Iss:2, (2024), pp.(160-159).
ORCID: [a]0000-0003-2135-9648; [b]0000-0002-5373-0379. [c]000-0001-7285-1531; [d]000-0002-1946-6260;

Abstract : Modifying fiber-reinforced polymers (FRPs) with carbon nanotubes (CNTs) becomes an effective strategy to improve the mechanical performance of the structural parts and add multifunctionality. However, this strategy increases the costs of such new-generation multi-scale composites. Machining of FRPs is challenging due to their susceptibility to machining-driven damages, leading to high-cost wastes. To prevent high-cost waste, the machinability of new-generation multi-scale composites with minimum damage becomes a vital processing issue. This work investigates the impact of CNTs on the drilling performance and hole quality of glass/epoxy multi-scale composites. Multi-scale composite laminates were drilled with high-speed steel drills under dry conditions. Cutting speed and feed rate were parametrically optimized, considering the deformation factor, delamination, and thrust force. The change in thrust force was recorded in situ, and deformation factors were calculated using image processing techniques. Moreover, the damage assessment of drilled holes was carried out with scanning electron microscope analysis to reveal the drilling-induced micro-scale damages. The addition of CNTs within the epoxy matrix increased thrust forces; however, lower delamination failures around exit sides were observed for multi-scale composites. Taguchi technique and analysis of variance were utilized to explore the contributions of drilling parameters and material type to the thrust force and deformation factor. Feed rate and material type were major factors affecting the deformation factor.

Keywords : Carbon Nanotube, Delamination, Multi-scale Composite, Machinability.

1 Introduction

Glass fiber-reinforced polymer composites (FRPs) have been employed intensively in various industries due to their high strength and stiffness, corrosive stability, and low thermal expansion [1, 2]. Although composite structures are designed to be produced to near-net shape, additional finishing operations like drilling are frequently preferred, especially for assembly [3]. The drilling process is utilized intensely to create bolted or riveted assemblies in composite structures, mainly employed in the aerospace and automotive industries [4, 5]. However, the drilling process of FRPs may raise severe defects that lead to the failure of composite structures, such as delamination, debonding, hole shrinkage, and fiber pull-out [6, 7]. Selecting optimum drilling parameters is crucial in achieving low thrust force and good hole quality and avoiding delamination [8].

Drilling fiber-reinforced composite materials can lead to delamination, which impairs the material's service life [5, 9]. Therefore, the drilling-dominated delamination failure of laminated composites has been investigated extensively in experimental and analytical methods [10, 11]. Capello[12] stated that drilling-dominated delamination failure is the primary responsible failure mechanism affecting the lifetime of the material. Mohan et al. [13] demonstrated that drilling parameters such as feed rate, cutting speed, and laminate thickness are the main parameters of delamination failure. Latha and Senthilkumar [14] recorded 3D images of the hole after drilling and established that the feed rate and drill diameter affect the delamination failure.

Different approaches have been suggested to reduce the delamination failure of FRPs. Recently, adding nanoscale fillers within FRPs to improve mechanical and physical properties has become an exciting point in material science. Carbon nanotubes (CNTs) offer to tailor interlaminar regions, well known as the "weak link" in laminated composites, without damaging the structure of FRPs due to their superior mechanical and physical properties [15, 16]. While much work has been carried out to

understand the mechanical properties of CNTs-modified FRPs, little has been carried out in machinability, particularly in the drilling process. Thus, the machinability of the new generation nanocomposites becomes a vital processing issue. Li et al. [17] investigated the drilling performance of CNTs-modified carbon fiber/epoxy composites and provided a reduced delamination factor of about 16% with the addition of CNTs. Kaybal et al. examined the effects of cutting parameters upon thrust force and delamination in carbon nanotube-modified carbon fiber-reinforced plastics. The impacts of the drilling parameters and degrees of influence were determined using the response surface analysis and Taguchi method. They reported that the machinability of Epoxy / CF is better than CNT-Epoxy/CF [18]. Kaybal et al. investigated the thrust force and delamination in drilling carbon-epoxy composites reinforced with boron nitride nanoparticles. According to the experimental results, boron nitride nanoparticles aided in reducing the delamination factor in the machining of the composite material [19]. Depending on the matrix materials, the impact of CNTs on the cutting forces varies. For instance, Mahmoodi et al. [20] and Le et al. [21] reported enhanced cutting forces and tool wear at high MWCNT weight percent in polystyrene (PS) or epoxy-based nanocomposites. It was reported that the cutting force of MWCNTs reinforced polycarbonate composite was less than that of neat polycarbonate. MWCNT/epoxy nanocomposites also produced higher thrust force with increasing CNT wt% in drilling. Kharwar and Verma [22] presented that the enhanced CNT ratio in the epoxy matrix resulted in higher trust forces. Moreover, in drilling, it has been shown by Çelik et al. [23] and Kumar et al. [24, 25] that CFRPs treated with graphene or graphene oxide (GO) typically result in greater cutting forces, delamination, surface roughness, and circularity error. Once more, there are disparities between research regarding how CNT nanofillers affect drilling of fiber reinforced polymer composites. While some studies found poor machinability with higher thrust forces and delamination in multiscale composites compared with the neat CFRPs [18], others found superior holes in MWCNT modified carbon fiber or glass fiber reinforced composites in terms of reduced thrust force, delamination, and surface cracks, as well as higher residual flexural strength [26, 27, 28].

The disparity in the impacts of CNTs on cutting forces in multiscale composite machining reported in the literature is likely a result of the various materials, CNT weight ratios, and cutting parameters employed in the various experiments. The main goal of this study is to investigate the drilling performance of CNTs-modified FRPs. Different drilling parameters are applied to neat and CNT-modified FRPs under the same conditions to consider the drilling performances of CNT-modified FRPs using high-speed steel drills. Taguchi technique and analysis of variance (ANOVA) were utilized to explore the contributions of drilling parameters and material type to the thrust force and deformation factor. A scanning electron microscopy (SEM) analysis was performed to assess the damage to drilled holes and reveal the drilling-induced micro-scale damages. According to the findings, the current study can fill a gap in the literature on machining CNT-modified composite laminates with minimum waste.

2 Experimental Methods

2.1 Materials

The woven glass fabric (Metyx Composite, 300 g/m^2) and diglycidyl ether bisphenol A (DGEBA) epoxy with an aliphatic amine curing agent (Momentive Hexion L285 and H285) were preferred to fabricate composite laminates. Multi-walled CNTs (MWCNTs) used in this study (Cheap Tube Inc., wt 95%) were synthesized by catalytic chemical vapor deposition process with lengths between 0.2 and 2 μm and diameters about 30-50 nm.

2.2 Oxidation of CNTs

The increase in mechanical properties by adding CNTs within polymer matrices is mainly governed by the effectiveness of dispersion within polymer matrix [29]. It is well known that the oxidation of CNTs improves dispersion and interfacial bonding with polymer matrix [30]. Hence, KMnO4/H2SO4 solution was applied to create oxygen-containing functional groups on the CNTs' sidewalls [31]. A desired amount of CNTs/KMnO4/H2SO4 mixture was prepared, and it was bath-sonicated for one hour at room temperature. After refluxing at 150^{o}C for 5 h, concentrated HCl (10 ml) was introduced within the mixture. Finally, the mixture was filtered with polar solvents and dried at 100^{o}C overnight.

2.3 Manufacturing of Multi-scale Composite Laminates

Multi-scale composite laminates are produced using vacuum-assisted resin infusion (VARIM) [32]. The matrix resin was prepared by dispersing 0.3 wt% of oxidized CNTs in the epoxy matrix without hardener using tip sonication (Bandelin Sonoplus HD 2070) for 15 min. The mixture was mixed manually for 5 min after the added curing agent and then degassed at 50^{o}C for 30 min. The neat epoxy mixtures were prepared without utilizing dispersing and degassing processes. The mixtures were slowly infused into a vacuum bag containing six plies of woven glass fabric under negative pressure, cured at 80 ^{o}C for 60 min, and then post-cured at 120 ^{o}C for 180 min. The laminates cooled to room temperature slowly. The thickness of the composite laminates was 3±0.25 mm. The fiber volume fraction (vf) of the composite laminate was obtained experimentally by the acid bath dissolution process according to ASTM D-3171/15, which was around 52%. Tensile strengths of composite laminates were measured according to ASTM D 3039 standard using an Instron 3369 universal tensile testing machine with a crosshead speed of 5 mm/min at room temperature. At least five specimens were tested for each composition. The typical tensile features of prepared composites are given in Supplementary Table S1.

Table 1: Experimental design using L18 orthogonal array and results.

Exp. No	Material	CS (m/min)	FR (mm/rev)	TF (N)	DF Entrance	DF Exit
1	Epoxy	50	0.05	20.2325	1.1007	1.251
2	Epoxy	50	0.10	37.7433	1.1042	1.2824
3	Epoxy	50	0.20	62.9150	1.1618	1.4191
4	Epoxy	75	0.05	16.5100	1.1128	1. 26
5	Epoxy	75	0.10	30.9825	1.1268	1.2834
6	Epoxy	75	0.20	61.2350	1.1642	1.4751
7	Epoxy	90	0.05	14.4750	1.1144	1.329
8	Epoxy	90	0.10	29.8300	1.1324	1.2939
9	Epoxy	90	0.20	49.1850	1.1715	1.3536
10	CNT/Epoxy	50	0.05	21.3033	1.1195	1.132
11	CNT/Epoxy	50	0.10	45.1475	1.1204	1.1338
12	CNT/Epoxy	50	0.20	56.2200	1.202	1.3191
13	CNT/Epoxy	75	0.05	18.5100	1.1279	1.143
14	CNT/Epoxy	75	0.10	39.3975	1.1323	1.1855
15	CNT/Epoxy	75	0.20	52.2400	1.2307	1.3354
16	CNT/Epoxy	90	0.05	17.5725	1.1609	1.169
17	CNT/Epoxy	90	0.10	34.9575	11.1617	1.2186
18	CNT/Epoxy	90	0.20	45.3550	1.2457	1.3699

2.4 Experimental Drilling Procedure

The drilling process of the fabricated composite laminates was utilized at a Mazak Variaxis 500 machining center. A piezoelectric dynamometer (Kistler 9257B) with a charge amplifier and data acquisition board was used to measure thrust forces during drilling. A high-speed steel (HSS) twist drill with two cutting edges (Ø8 mm and a point angle of 118°) was used to drill composite laminates. During the drilling process, the samples were fixed on the dynamometer between two steel supporting blocks with twelve holes (Ø12 mm) (Figure S1). The supporting blocks were preferred due to their advantages during drilling FRPs at high feed rates [33, 34]. Four holes were drilled for each processing parameter (see Supplementary Table 2), and the average thrust force values were calculated.

In the drilling of composite materials, the delamination at the entry and exit of the hole was evaluated via the delamination factor, FD, using the maximum crack length from the hole center. The deformation factor was determined by formula 1. [35];

where Dmax is the maximum diameter of the damage zone, and D is the hole diameter.

A Leica DM2700 M model optical microscope visualized the delamination zones at the drill entrance and exit. Scanning electron microscopy (SEM) (A Zeiss Evo LS 10) was also used to monitor the cross-sections of holes to reveal delamination failure between layers of the laminates. Taguchi technique is used to design high-quality experimental systems [35, 36]. Notably, the drilling parameters were designed to have three levels, while the material type has two. The L18 array was applied to design experiments, as shown in Table 1.

Taguchi method uses signal-to-noise (S/N) ratios to analyze mean response and variation derived from the quadratic loss function. The widely applicable S/N ratios are given in Eqs. 2–4;

$$F_D = \frac{D_{\max}}{D} \tag{1}$$

$$\text{Nominal is the best: } \frac{S}{N} = 10\log\left(\frac{y^2}{s^2}\right) \tag{2}$$

$$\text{Lower is the best: } \frac{S}{N} = -10\log\left(\frac{1}{n}\sum_{i=0}^{n}\frac{1}{y_i^2}\right) \tag{3}$$

$$\text{Higher is the best: } \frac{S}{N} = -\log\left(\frac{1}{n}\sum_{i=0}^{n}\frac{1}{y_i^2}\right) \tag{4}$$

Where y' is the average of measured data, s^2 is the variation of y, n is the number of measurements, and y is the measured data [13]. The signal-to-noise response tables of the thrust force and deformation factor for each experiment are shown in Table 2.

2.5 Thrust force and delamination factors

The impact of drilling parameters on the recorded thrust forces and calculated deformation factors is shown in Figure 1. In general, the thrust force increases with increasing feed rates for both composite laminate samples at fixed cutting speeds (Figure 1a). Note that higher feed rates result in the increased contact area and load on the tool. The lowest thrust forces were recorded at the highest cutting speed (90 m/min) for fixed feed rates for all cases. This result is attributed to the softening of the polymer

Table 2: S/N response table for thrust force and delamination factor.

Trial No	Thrust Force (S/N Ratio)	Delamination Factor of Entrance (S/N Ratio)	Delamination Factor of Exit (S/N Ratio)
1	-26.120991	-0.83338	-1.94515
2	-31.536804	-0.86095	-2.16047
3	-35.975084	-1.30263	-3.04026
4	-24.354941	-0.92834	-2.00741
5	-29.822329	-1.03694	-2.16724
6	-35.739994	-1.32055	-3.37643
7	-23.212371	-0.94082	-2.47050
8	-29.493065	-1.08000	-2.23801
9	-33.836654	-1.37485	-2.62981
10	-26.568950	-0.98048	-1.07693
11	-33.092674	-0.98746	-1.09073
12	-34.997817	-1.59809	-2.40555
13	-25.348128	-1.04541	-1.16092
14	-31.909373	-1.07923	-1.47803
15	-34.360063	-1.80304	-2.51223
16	-24.896671	-1.29590	-1.35629
17	-30.870807	-1.30188	-1.71722
18	-33.132503	-1.90827	-2.73378

matrix with increasing cutting speed since higher temperatures occur at higher cutting speeds [37]. The high cutting speed and low feed rate result in minimized thrust forces for both composite laminates. Interestingly, relatively lower thrust force values were measured for CNTs/epoxy composites in the case of the highest feed rate. In contrast, relatively higher thrust forces were recorded for other cases, as shown in the figure. Kumar and Singh [38] reported that the thrust force was decreased by adding CNT nanoparticles. Similarly, Soleymani et al. [39] and Rajakumar et al. [40] revealed the diminishing trend in the thrust force by adding nanoparticles into the matrix. This result can be attributed to thermal relaxation of the CNT modified epoxy matrix due to the increased thermal conductivity with the addition of CNTs. Drilling-triggered delamination is an interlaminar failure problem for laminated composites and is fundamentally governed by interlaminar fracture toughness. Delamination damage for drilled composite laminates is expressed numerically by the deformation factor, which is the highest diameter in the damaged area to the diameter of the drill. Several observations can be made regarding calculated deformation factors for the entrance and exit sides, as shown in Figure 1b-c. Deformation factors increase with increasing feed rates and cutting rates as expected. The calculated deformation factors at entrance sides for CNT-modified composite laminates are relatively higher than neat composite laminates. However, an opposite delamination trend was observed for the exit holes, as higher deformation factors were found for neat composites rather than CNT-modified laminates at the processing conditions. The increase in deformation factors regarding increasing cutting speeds and feed rates is around 8 and 18% for entrance and exit holes, respectively. The higher deformation factors at the exit holes can be attributed to the bending effect of thrust forces and burr-dominated delamination. Note that lower deformation factors for CNT-modified laminates were obtained at exit holes, indicating the positive contribution of CNTs on delamination properties.

During drilling, the surface delamination types of laminated composites can be grouped as peel-up delamination at the entrance and push-down delamination at the hole's exit. The CNTs-modified glass fiber-reinforced epoxy composites provide higher Mode I interlaminar fracture toughness than traditional glass fiber-reinforced composite laminates. Our previous studies proved that CNT addition within the epoxy matrix for glass fiber-reinforced composites increased Mode I interlaminar fracture toughness by more than 20% of traditional glass fiber-reinforced composite laminates [41]. Results indicate that CNT modification of the epoxy matrix specifically enhances the delamination resistance of the composite laminate at the exit hole despite higher thrust forces being recorded [18]. These results suggest that adding CNTs increases fiber-polymer interfacial properties and mechanical toughening mechanisms [42, 43].

Generally, the deformation factor increases with increasing cutting speeds at fixed feed rates for both composite laminates. Maximum deformation factors were obtained at the highest feed rates. An almost linear increasing trend for the deformation factor with increasing cutting speeds at fixed feed rates was measured for CNT-modified composite laminates.

2.6 SEM analysis

The effect of CNT modification on the delamination of composite laminates during the drilling process was investigated by SEM analysis. The cross-sections of holes drilled at different cutting parameters were visualized and represented in Figure 2.

SEM investigations revealed that the fibers perpendicular to the tool axis were cut uniformly. Fiber pull-out was not observed for these layers (Figure 2a). Delaminated layers can be seen advancing around the hole surface (Figure 2b). The thrust force plays a vital role in the delamination of layers since the stress originated by thrust force leads to interlaminar crack propagation. Besides, bending and shear occur around the hole, and a combined stress problem appears during the drilling of layered composite laminates.

The uncut fibers as burr for laminated composites can be seen at the laminate cross-section in Figure 3a. Note that the

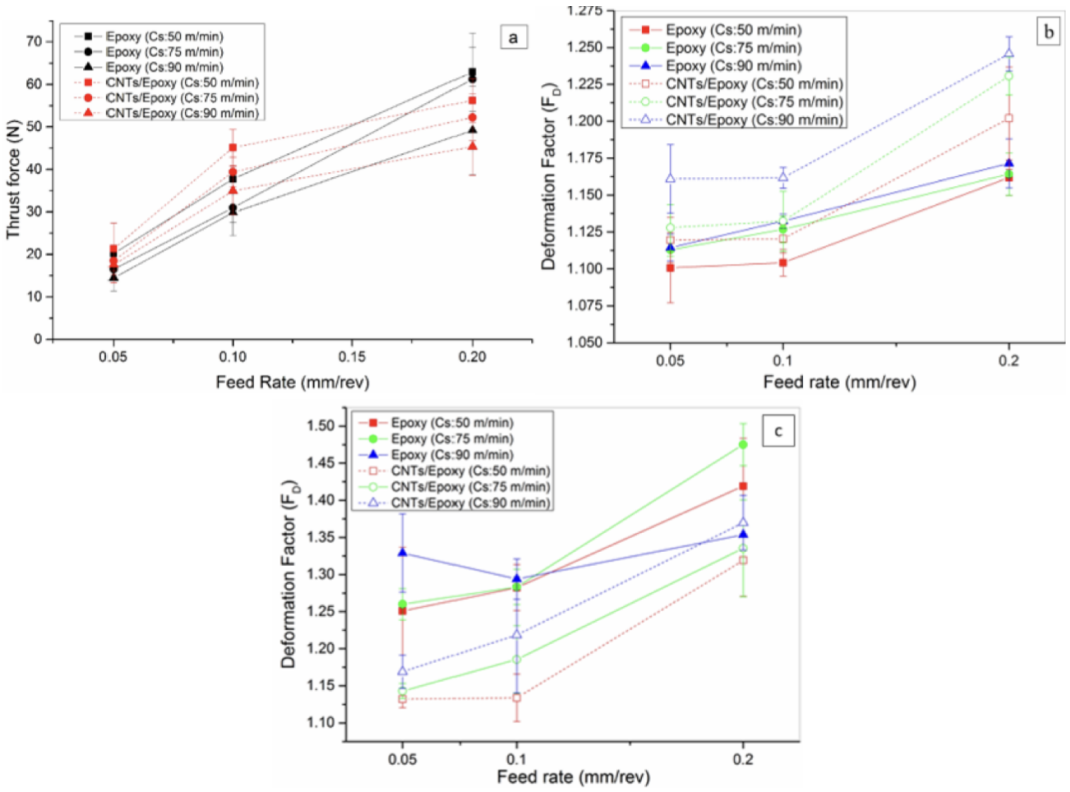

Figure 1: a) Measured thrust forces for epoxy and CNTs modified epoxy GF reinforced laminated composites at different drilling parameters, deformation factors b) entrance, c) exit

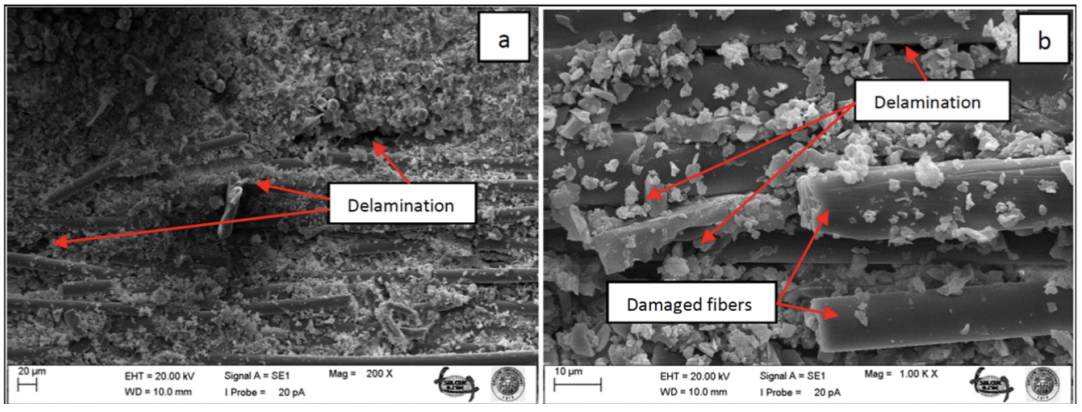

Figure 2: High magnification SEM images of the hole cross-section of GF/epoxy laminates (Feed Rate:0.1 mm/rev; Cutting speed: 75 m/min) a) delamination from resin-rich region of the lamina (the drill entry is located at the upside of the image), b) Fiber damage around delamination path of the laminate (the drill entry is located at the upside of the image)

composite laminates were fixed between two parallel tools to reduce vibration during drilling. However, the uncut fibers were observed mainly at the exits of holes (Figure 3b). Also, the figure represents the delamination damage between fabric layers initiated during drilling, as shown in Figure 3c. CNT pulled out as indicated by arrows, improves interlaminar fracture toughness by bridging and pull-out.

The impact of CNTs on the drilling performance is represented schematically in Supplementary Figure S2. Randomly oriented CNTs within the epoxy matrix were placed between glass fabric plies as resin-rich regions. The resin-rich regions in laminated composites are known to be very sensitive to the formation and propagation of cracks. During drilling, the thrust force and rotation of the drill bit lead to delamination failure by generating compression, bending, and shear stresses in the interlaminar region of the plies. CNTs between the plies within the resin-rich region enhance the contact area and adhesion between the matrix and fibers, increasing interlaminar fracture toughness.

Moreover, the bridging and pull-out of CNTs after crack formation increases the absorption of the fracture energy, which

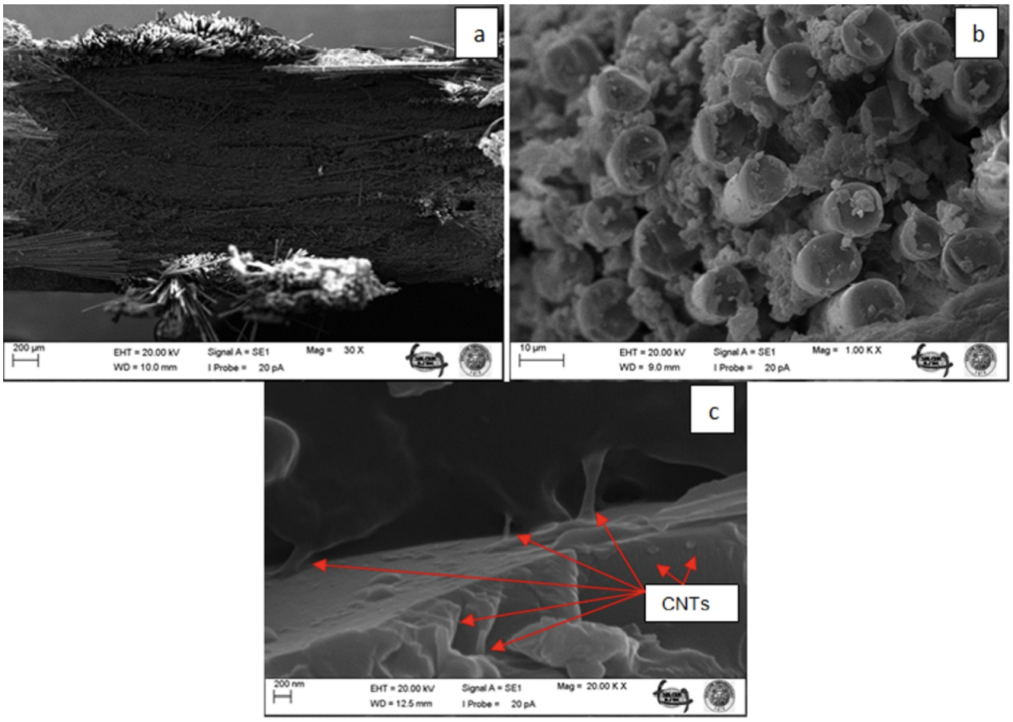

Figure 3: SEM images of the hole cross-section of CNT modified GF/epoxy laminates (Feed Rate:0.1 mm/rev; Cutting speed: 75 m/min) a) low magnification of hole cross-section (the drill entry is located at the upside of the image), b) uncut fiber around drill exit, c) CNTs contributing on delamination toughing of the composite laminate by bridging and pull-out

Table 3: S/N response table for thrust force and deformation factors.

	Thrust Force			Deformation Factor of Entrance			Deformation Factor of Exit		
Level	Material	C.Speed	F. Rate	Material	C.Speed	F. Rate	Material	C.Speed	F. Rate
1	-30.01	-31.38	-25.08	-1.075	-1.094	-1.004	-2.448	-1.953	-1.670
2	-30.58	-30.26	-31.12	-1.333	-1.202	-1.058	-1.726	-2.117	-1.809
3	-	-29.24	-34.67	-	-1.317	-1.551	-	-2.191	-2.783
Delta	-24.354941	-0.92834	-2.00741						
Rank	-	3	2	1	2	3	1	2	3

drives the crack and limits the crack's propagation between the plies. Thereby, deformation factors were explicitly decreased at the exit holes for CNT-modified composite laminates by considering increased interlaminar fracture toughness with the addition of CNTs. The calculated S/N values for each experiment are represented in Table 3. The S/N ratio response graphs for thrust force and delamination factors at the workpiece entrance and exit are given in Figure 4. Based on the S/N ratio response results, the optimum drilling parameters were obtained as Level 3 (90 m/min) and Level 1 (0.05 mm/rev) for the cutting speed and feed rate, respectively. These results are consistent with our discussions derived from Figure 3.

On the other hand, the optimal material type found is epoxy and CNTs/epoxy for entrance and exit hole surfaces, respectively. Cutting speed and feed rate at Level 1 were obtained as the optimum drilling parameters for the deformation factor at the entrance

Table 4: Table ANOVA for the deformation factors at the entrance.

Source	DF	SS	MS	F	PCR
Material	1	0.2994	0.29936	29.59	18.0116
Cutting Speed (m/min)	2	0.1494	0.07469	7.38	8.9902
Feed Rate (mm/rev)	2	1.0914	0.54583	53.94	65.6915
Residual Error	12	0.1214	0.01012		
Total	17	1.6618			

Table 5: Table ANOVA for the deformation factors at the exit.

Source	DF	SS	MS	F	PCR
Material	1	2.3498	2.34982	38.00	30.5696
Cutting Speed (m/min)	2	0.1777	0.08884	1.44	2.3117
Feed Rate (mm/rev)	2	4.4172	2.20861	35.72	57.4654
Residual Error	12	0.7420	0.06183		
Total	17	7.6867			

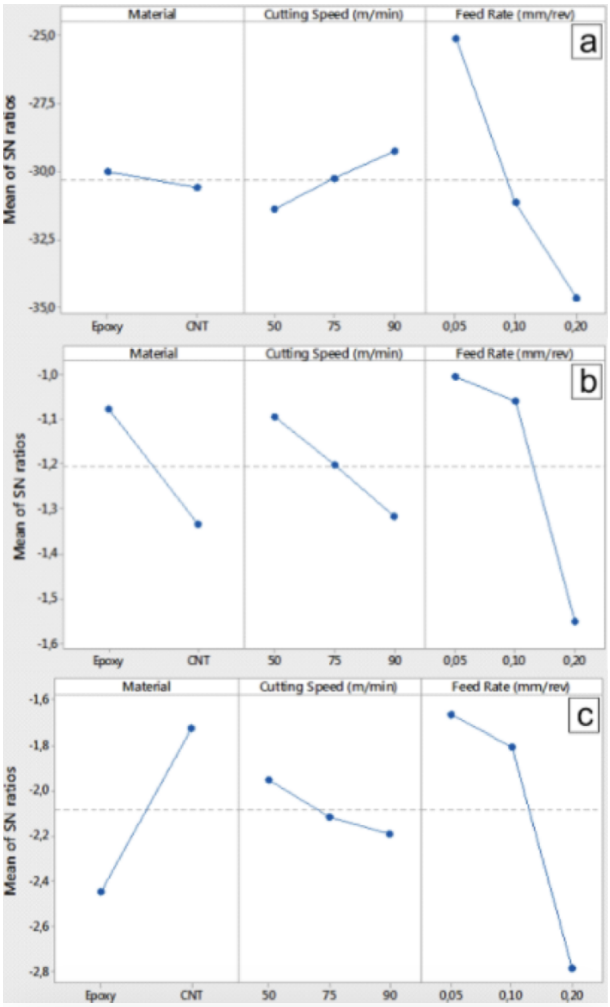

Figure 4: Main effects plots for S/N ratios a) thrust force, b) deformation factor at entrance, c) deformation factor at exit

Table 6: Table ANOVA for the thrust force.

Source	DF	SS	MS	F	PCR
Material	1	1.436	1.436	2.33	0.4713
Cutting Speed (m/min)	2	13.773	6.887	11.16	4.5203
Feed Rate (mm/rev)	2	282.077	141.038	228.66	92.5789
Residual Error	12	7.402	0.617		
Total	17	304.688			

and exit holes.

The analysis of variance (ANOVA) was implemented to realize the effects of material type and drilling parameters on the thrust force (Table 4) and delamination factors (Table 5 and Table 6). Based on the results in Tables 4-6, the feed rates govern the thrust force and delamination. Feed rate dominates the measured thrust force values with 92.57% PCR value, as seen in Table 4. According to ANOVA analysis, the thrust force is not affected by material type. The contribution of feed rate on deformation factors is calculated as 65.69 and 57.46% at the workpiece entrance and exit, respectively. ANOVA results revealed that cutting speed is the less critical parameter affecting the deformation factor, with contributions of 8.99 and 2.31%. In comparison, material type becomes the second one with contributions of 18.01 and 30.56% at the entrance and exit, respectively. The results indicate that CNT modification of the epoxy matrix contributes to decreasing deformation factors at the hole's exit side by improving the matrix's mechanical performance and interlaminar properties between resin-rich fiber layers.

3 Conclusions

The CNT-modified multi-scale epoxy/glass fiber composite laminates were drilled with HSS drills under different processing conditions. The CNT modification reduces delamination damages at the exit holes but increases thrust forces. The processing parameters were evaluated to optimize conditions for CNT-modified polymer composite laminates. However, detailed studies

should be carried out with different drills and drill geometries to clarify the effect of CNT modification on the drilling performance of the laminated composites. We believe this study will help researchers working on similar areas zoom in on nanoscale contribution to polymer composite processing. The ANOVA analysis exposed that the delamination factor is mainly controlled by feed rate, as high feed rates lead to maximum damage. However, material type also contributes as the second major factor in the deformation factor, which shows the aid of CNTs in modifying the epoxy matrix.

Acknowledgments
The authors thank the Department of Mechanical Engineering, Selcuk University, for their valuable support.

Authors' Contributions
In this study, MK: Project administration, Conceptualisation, Investigation, Writing - original draft, Visualisation. VE: Conceptualisation, Methodology, Writing - review & editing, Validation. AÜ: Investigation, Methodology, Writing - review & editing, Validation, Supervision. AA: Writing - review & editing, Supervision.

Competing Interests
The authors declare that they have no conflict of interest.

References
[1] M. Çakır and B. Berberoğlu. Investigation of changes in mechanical properties of e-glass fiber reinforced epoxy matrix composite materials with increase of fiber ratios. *El-Cezerî Journal of Science and Engineering*, 5(3):734–740, 2018. .
[2] P. Kulkarni, A. Dhoble, and P. Padole. A review of research and recent trends in analysis of composite plates. *Sadhana - Acad Proc Eng Sci*, 43:1–20, 2018. .
[3] L.M.P. Durão, D.J.S. Gonçalves, J.M.R.S. Tavares, V.H.C. De Albuquerque, and A.T. Marques. Comparative analysis of drills for composite laminates. *J. Compos. Mater.*, 46:1649–1659, 2012. .
[4] A.M. Abraõ, J.C.C. Rubio, P.E. Faria, and J.P. Davim. The effect of cutting tool geometry on thrust force and delamination when drilling glass fibre reinforced plastic composite. *Mater. Des.*, 29:508–513, 2008. .
[5] I. El-Sonbaty, U.A. Khashaba, and T. Machaly. Factors affecting the machinability of gfr/epoxy composites. *Compos. Struct.*, 63:329–338, 2004. .
[6] I.P.T. Rajakumar, P. Hariharan, and I. Srikanth. A study on monitoring the drilling of polymeric nanocomposite laminates using acoustic emission. *J Compos Mater.*, 47:1773–1784, 2008. .
[7] K. Palanikumar, B. Latha, V.S. Senthilkumar, and J.P. Davim. Analysis on drilling of glass fiber-reinforced polymer (gfrp) composites using grey relational analysis. *Mater. Manuf. Process.*, 27:297–305, 2012. .
[8] K. Debnath, M. Sisodia, and A. Kumar. Damage-free hole making in fiber-reinforced composites: An innovative tool design approach. *Mater. Manuf. Process.*, 31:1400–1408, 2016. .
[9] C.L. Tan, A.I. Azmi, and N. Muhammad. Delamination and surface roughness analyses in drilling hybrid carbon/glass composite. *Mater. Manuf. Process.*, 31:1366–1376, 2016. .
[10] J.P. Davim, P. Reis, and C.C. António. Drilling fiber reinforced plastics (frps) manufactured by hand lay-up: Influence of matrix (viapal vhp 9731 and atlac 382-05). *J. Mater. Process.Techno.*, 155(156):1828–1833, 2004. .
[11] H.M. Ali, A. Iqbal, and L. Liang. A comparative study on the use of drilling and milling processes in hole making of gfrp composite. *Sadhana - Acad Proc Eng Sci*, 38:743–760, 2013. .
[12] E. Capello. Workpiece damping and its effect on delamination damage in drilling thin composite laminates. *J. Mater. Process. Technol.*, 148:186–195, 2004. .
[13] N.S. Mohan, S.M. Kulkarni, and A. Ramachandra. Delamination analysis in drilling process of glass fiber reinforced plastic (gfrp) composite materials. *J. Mater. Process. Techno.*, 186:265–271, 2007. .
[14] B. Latha and V.S. Senthilkumar. Fuzzy rule based modeling of drilling parameters for delamination in drilling gfrp composites. *J. Reinf. Plast. Compos.*, 28:951–964, 2009. .
[15] C. Li and T.W. Chou. Elastic moduli of multi-walled carbon nanotubes and the effect of van der waals forces. *Compos. Sci. Technol.*, 63:1517–1524, 2003. .
[16] F. Durmuş, M. Ekrem, and G. Önal. Mechanical properties of mwcnt reinforced polyvinyl alcohol nanofiber mats by electrospinning method. *El- Cezerî Journal of Science and Engineering*, 4(2):146–155, 2017. .
[17] N. Li, Y. Li, J. Zhou, Y. He, and X. Hao. Drilling delamination and thermal damage of carbon nanotube/carbon fiber reinforced epoxy composites processed by microwave curing. *J. Int. J. Mach. Tools Manuf.*, 97:11–17, 2015. .
[18] H.B. Kaybal, A. Ünüvar, M. Koyunbakan, and A. Avcı. A novelty optimization approach for drilling of cfrp nanocomposite laminates. *The International Journal of Advanced Manufacturing Technology*, 100:2995–3012, 2019. .
[19] H.B. Kaybal, A. Ünüvar, Y. Kaynak, and A. Avcı. Evaluation of boron nitride nanoparticles on delamination in drilling carbon fiber epoxy nanocomposite materials. *Journal of Composite Materials*, 54:1–13, 2019. .

[20] M. Mahmoodi, M.G. Mostofa, M. Jun, and S.S. Park. Characterization and micromilling of flow induced aligned carbon nanotube nanocomposites. *J Micro Nano-Manuf*, 1:Article 011009, 2013.
[21] B. Le, A. Kernin, J. Khaliq, G. Fu, D. Huo, E. Bilotti, H. Zhang, and I. Shyha. Micro-end-milling of carbon nanotube reinforced epoxy nanocomposites manufactured using three roll mill technique. *J Manuf Process*, 70:307–320, 2021. .
[22] P. K. Kharwar and R. K. Verma. Nature instigated grey wolf algorithm for parametric optimization during machining (milling) of polymer nanocomposites. *Journal of Thermoplastic Composite Materials*, 36(2):1–23, 2021. .
[23] Y. H. Çelik, E. Kilickap, and N. Koçyiğit. Evaluation of drilling performances of nanocomposites reinforced with graphene and graphene oxide. *Int J Adv Manuf Techno*, 100:2371–2385, 2019. .
[24] J. Kumar and R.K. Verma. A novel methodology of combined compromise solution and principal component analysis (cocoso-pca) for machinability investigation of graphene nanocomposites. *CIRP J Manuf Sci Technol*, 33:143–157, 2021. .
[25] J. Kumar, R.K. Verma, and K. Debnath. A new approach to control the delamination and thrust force during drilling of polymer nanocomposites reinforced by graphene oxide/carbon fiber. *Compos Struct*, 253:1–15, 2020. .
[26] M. Baraheni, A. Tabatabaeian, S. Amini, and A.R. Ghasemi. Parametric analysis of delamination in gfrp composite profiles by performing rotary ultrasonic drilling approach: experimental and statistical study. *Compos Part B Eng*, 172:612–620, 2019. .
[27] H. Heidary, N.Z. Karimi, and G. Minak. Investigation on delamination and flexural properties in drilling of carbon nanotube/polymer composites. *Compos Struct*, 201:112–120, 2019. .
[28] N. Li, Y. Lin, J. Zhou, Y. He, and X. Hao. Drilling delamination and thermal damage of carbon nanotube/carbon fiber reinforced epoxy composites processed by microwave curing. *Int J Mach Tool Manuf*, 97:11–17, 2015. .
[29] F. Inam, D.W.Y. Wong, M. Kuwata, and T. Peijs. Multi-scale hybrid micro-nanocomposites based on carbon nanotubes and carbon fibers. *Journal of Nanomaterials*, 2010:1–1–2, 2010. .
[30] V.C.S. Chandrasekaran, S.G. Advani, and M.H. Santare. Role of processing on interlaminar shear strength enhancement of epoxy/glass fiber/multi-walled carbon nanotube hybrid composites. *Carbon N. Y*, 48:3692–3699, 2010. .
[31] K.A. Wepasnick, B.A. Smith, K.E. Schrote, H.K. Wilson, S.R. Diegelmann, and D.H. Fairbrother. Surface and structural characterization of multi-walled carbon nanotubes following different oxidative treatments. *Carbon N. Y*, 49:24–36, 2010. .
[32] M. Sánchez, M. Campo, and A. Ureña. Effect of the carbon nanotube functionalization on flexural properties of multi-scale carbon fiber/epoxy composites manufactured by varim. *Composites Part B*, 45:1613–1619, 2010. .
[33] R. Piquet, B. Ferret, F. Lachaud, and P. Swider. Experimental analysis of drilling damage in thin carbon/epoxy plate using special drills. *Compos Part A-Appl*, 31:1107–1115, 2000. .
[34] C.C. Tsao and H. Hocheng. Parametric study on thrust force of core drill. *J Mater Process Tech*, 192:37–40, 2007. .
[35] E. Kilickap. Determination of optimum parameters on delamination in drilling of gfrp composites by taguchi method. *Indian Journal of Engineering & Materials Sciences*, 17:265–274, 2010.
[36] J.L. Rosa, A. Robin, M.B. Silva, C.A. Baldan, and M.P. Peres. Electrodeposition of copper on titanium wires: Taguchi experimental design approach. *J Mater Process Tech*, 209(3):1181–1188, 2009. .
[37] T.N. Valarmathi, K. Palanikumar, and B. Latha. Measurement and analysis of thrust force in drilling of particle board (pb) composite panels. *Measurement*, 46:1220–1230, 2013. .
[38] D. Kumar and K. Singh. Investigation of delamination and surface quality of machined holes in drilling of multiwalled carbon nanotube doped epoxy/carbon fiber reinforced polymer nanocomposite. *J Mater Design Appl*, 233:647–663, 2019. .
[39] M. Soleymani Yazdi, M. Razfar, and M. Asadnia. Modelling of the thrust force of the drilling operation on pa6–nanoclay nanocomposites using particle swarm optimization. *J Eng Manufact*, 225:1757–1771, 2007. .
[40] I.P.T. Rajakumar, P. Hariharan, and I. Srikanth. A study on monitoring the drilling of polymeric nanocomposite laminates using acoustic emission. *J Compos Mater*, 47:1773–1784, 2013. .
[41] V. Eskizeybek, A. Avci, and A. Gülce. The mode i interlaminar fracture toughness of chemically carbon nanotube grafted glass fabric/epoxy multi-scale composite structures. *Compos Part A*, 63:94–102, 2014. .
[42] F.H. Gojny, M.H.G. Wichmann, B. Fiedler, and K. Schulte. Influence of different carbon nanotubes on the mechanical properties of epoxy matrix composites – a comparative study. *Compos Sci Technol*, 65:2300–2313, 2005. .
[43] F. Yildirim, M. Aydin, and A. Avci. Improved mechanical performance of three-dimensional woven glass/epoxy spacer composites with carbon nanotubes. *J Reinf Plast Compos*, 40:533–549, 2021. .

El Cezeri
Journal of Science and Engineering
ISSN: 2148-3736

Research Article

Teaching Effective Techniques for Incorporating Edge Computing in Biomedical Applications with Biomedical Students

Yeliz Durgun[1a], Mahmut Durgun[1b]
[1] Department of Biomedical Equipment Technology Program, Tokat Gaziosmanpasa University, Turhal, Tokat, Türkiye
[2] Department of Electronic Commerce and Management, Tokat Gaziosmanpasa University, Turhal, Tokat, Türkiye

yeliz.durgun@gop.edu.tr

DOI : 10.31202/ecjse.1369680
Received: 01.10.2023 Accepted: 21.05.2024
How to cite this article:
Yeliz Durgun, Mahmut Durgun, " Teaching Effective Techniques for Incorporating Edge Computing in Biomedical Applications with Biomedical Students", El-Cezeri Journal of Science and Engineering, Vol: 11, Iss:2, (2024), pp.(169-174).
ORCID: [a]0000-0003-3834-5533; [b]0000-0002-5010-687X.

Abstract : This case study demonstrates the potential of integrating the Edge Impulse platform into project based learning for biomedical technology students for edge computing consept. The use of the Edge Impulse platform as a project-based teaching and learning approach for biomedical students has been shown to significantly enhance student learning performance and experiences. The platform allows students to develop practical skills and deepen their knowledge while also providing opportunities for students to apply their projects in real-world settings. This study provides valuable insights on how to effectively improve learning for biomedical students using the Edge Impulse platform. The study focuses on a course designed using the Edge Impulse platform, where students design and develop prototype devices and systems. The course begins with the learning of basic hardware and culminates in students creating a complete prototype system. The study showcases the prototype devices and systems developed by students at the end of the course, demonstrating how the use of Edge Impulse platform improves students' practical skills and enables them to apply their projects in real-world settings. Furthermore, it highlights how this approach contributes to students' self-development and acquisition of skills that can be used in their future careers. Thus, the use of this platform can lead to new ideas and experiences which may open new horizons for biomedical research and the development of integrated devices in the current world.

Keywords : Architectures for educational technology system, Cooperative/collaborative learning, Data science applications in education,Improving classroom teaching, Teaching/learning strategies

1 Introduction

This study examines the application of edge computing in the biomedical field, particularly focusing on its instructional applications for students. Edge computing addresses the need for small-scale data processing, reducing the data transmitted over networks, thereby cutting transmission costs, alleviating network bandwidth pressure, reducing the energy consumption of local equipment, and enhancing processing efficiency [1], [2]. This approach is particularly beneficial for biomedical device companies, reducing data processing costs while increasing device performance and efficiency [3].

In the biomedical field, edge computing finds numerous applications. For example, edge computing-enabled sensors and smart devices can collect and analyze real-time data within the body. Data analytics facilitated by edge computing can aid in early disease diagnosis, determining treatment options, and monitoring treatments [4]–[8]. Machine Learning (ML), powered by edge computing, can analyze biomedical images and sound data in real-time [9]–[11]. Robotics and virtual reality applications benefit from the high performance and scalability provided by edge computing, useful in surgical operations and medical training [12]–[14]. The Internet of Medical Things (IoMT), supported by edge computing, plays a crucial role in real-time data collection and analysis in hospitals and home settings [15], [16]. Furthermore, edge computing enables the development of advanced portable technologies for real-time health monitoring [17], [18] and telemedicine applications, facilitating remote medical consultations and monitoring [19], [20].

These examples underscore the versatility of edge computing in various biomedical applications. Its capacity for real-time data collection, analytics, and ML will further propel research and development in this field.

The aim of this study is to elucidate the use of edge computing in biomedical fields for students, creating innovative solutions and providing rapid feedback. The Project-Based Learning (PBL) method, by affording students hands-on experiences in real-world projects, enhances engineering understanding, problem-solving abilities, self-efficacy beliefs, and collaborative learning skills in biomedical device technology students [21], [22]. The PBL method also aids in developing practical skills and

interdisciplinary thinking beyond theoretical knowledge, improving the performance of students with lower achievements [23].

In Edge Impulse projects, specialized wireless communication-enabled microcontrollers are essential to provide students with practical experiences based on real-world projects [24]. Cost-effective, small-sized, and high-processing power hardware platforms like the Arduino Nano BLE 33 are ideal for the PBL paradigm in biomedical fields. This platform not only facilitates hands-on experiences and enhances engineering understanding but also ensures efficient information processing with minimal cost and energy consumption. The Arduino Nano BLE 33 has been utilized in Edge Impulse trainings, serving as a foundational tool for advanced learning systems. Edge Impulse, an online platform designed for easy data collection, deep learning model training, and deployment to embedded and edge devices, supports the aforementioned biomedical solutions. While targeting business sector customers for Edge ML solutions development, Edge Impulse also fosters a research-friendly and class-friendly environment.

The integration of microcontrollers and AI applications in biomedical education is pivotal in imparting practical skills and enhancing educational processes. AI's role in personalizing educational materials, assessing student performance, and providing interactive learning experiences is increasingly recognized. For instance, Zawacki-Richter et al. (2019) offer an overview of AI applications in higher education, exploring their effective use and pedagogical evaluation [25]. Similarly, Sak and Suchodolska (2021) analyzed AI's current use in nutrient science research, demonstrating its application in biomedical sciences, particularly nutrition and dietetics [26]. Briganti and Le Moine (2020) discussed the application of AI-powered medical technologies in clinical practice and education, providing insights into integrating AI into medical education [27].

2 Experimental Methods

2.1 Overview of Arduino Nano 33 BLE

Arduino Nano 33 BLE is a small, low-cost microcontroller board that is based on the 32-bit ARM Cortex-M0+ SAMD21 microcontroller. It is designed to be compatible with the Arduino software development environment, making it easy for users to program and control various electronics projects. The board features built-in Bluetooth Low Energy (BLE) connectivity, enabling wireless communication with other devices and internet connection capabilities. Additionally, it has a built-in USB to serial converter for easy programming and communication with computers. The board offers a variety of digital and analog input/output pins and supports peripherals like timers, PWM, and I2C. Arduino Nano 33 BLE is equipped with sensors including a 9-axis IMU, temperature, and light sensors, suitable for environmental data gathering and powered by the low power Arm Cortex-M0+ processor, making it ideal for battery-powered projects. This board is extensively used in IoT devices, robotics, and home automation systems.

2.2 Project-Based Teaching Concept

The success of the project-based teaching paradigm is closely tied to the design of the projects that students undertake. Projects should align with students' prior knowledge and be appropriately challenging to maintain interest and motivation. This section outlines the course structure and describes the series of projects that embody our project-based teaching approach. Hardware for these projects is provided by the Edge Impulse TinyML Kit, allowing students to engage with sensors, actuators, and other devices necessary for real-world applications. Students can program using their choice of sensors and devices, facilitating the development of solutions for actual problems and enhancing their programming skills.

2.3 Course Content

The Microcontroller course, a three-credit, semester-long course offered to students in the Biomedical Device Technology department, introduces Internet of Things (IoT) technologies and applications. Topics covered include IoT concepts and architecture, communication mechanisms, IP stack, 6LoWPAN adaptation, protocols, operating systems, sensors, and actuators. The course aims to equip students with the ability to create and utilize IoT applications, requiring no prior hardware experience, although basic programming knowledge is beneficial.

2.4 Project Design

The project-based teaching approach implemented in this curriculum involves semester-long project work. Using the "divide and conquer" methodology, projects are designed in a series of three specific projects: Fall Detection, Cough Monitor, and Machine Vision with Low Cost Camera Modules. Projects are carried out individually or in teams of two, fostering both individual and teamwork skills. These projects are structured to challenge students and enhance their programming skills while providing real-world problem-solving experiences.

2.5 Fall Detection

Using the TinyML-based Arduino Nano 33 BLE, this project develops a fall detection device utilizing ML technology. Data from an accelerometer or motion sensor is processed to train ML algorithms and analyze subsequent data. The project uses the

Arduino Nano 33 BLE Sense board to detect falls, send alerts, and communicate via Bluetooth with a mobile app. The solution achieves a 95

2.6 Cough Monitor

This project develops a solution for monitoring the cough frequency and intensity in individuals with chronic obstructive pulmonary disease (COPD) using the Arduino Nano 33 BLE Sense. A TinyML model classifies cough sounds, and a BLE service on the device increments the cough count for each detection, with data transmitted to the cloud for analysis.

2.7 Machine Vision with Low Cost Camera Modules

Students implement image processing applications using an external VGA camera module paired with the Arduino Nano 33 BLE, supported by Edge Impulse. The project demonstrates how to acquire image data, create an ML model, and perform image classification, training the model with known data to control prediction accuracy.

3 Results

During the 2022 fall semester, 10 students in the classroom used the Arduino Nano 33 BLE platform. An informal survey conducted at the start of the class revealed that none of the students had prior experience with the hardware. Hence, we utilized training and learning materials extensively to impart basic knowledge and skills about hardware. We continuously monitored and analyzed the students' performance to identify the subjects each student found challenging or understood well. After each project, student projects were evaluated and feedback was provided, leading to suggestions for enhancing the content and execution of the projects. This approach significantly improved students' understanding of the hardware and the effectiveness of project realization.

3.1 Project 1: Sensor Module Data Handling

Project 1 focused on increasing students' confidence in working with microcontroller hardware and development environments. It involved data recording with the LSM9DS1 nine-axis Sensor Module (IMU Accelerometer, Gyroscope, Magnetometer) on Arduino Nano BLE. Students learned to organize, configure, and operate the recorded data with ML algorithms and hardware/software tools, enhancing their problem-solving skills. The project aimed to provide hands-on experience and prepare students for future challenging projects. Students successfully completed this project, creating datasets from drop trials with data from 10 volunteers including acceleration and rotation data, acquired at a 200 Hz sampling rate. One student attempt from Project 1 is illustrated in Figure 1.

3.2 Project 2: Cough Detection System

Project 2, a more advanced and challenging project, involved detecting and reporting people's coughs. It aimed to teach students how to use, structure, and read sound data for sound detection, enhancing their software development skills. All 10 students successfully completed this project, with six understanding basic audio data concepts such as frequency and pulse well, while four excelled in using pre-built software components. Figure 2 shows sample audio data from this project, highlighting the complexity of mathematical and multidimensional analysis for students.

3.3 Project 3: Object Classification with Machine Vision

In the final project, all students were able to correctly use a camera to classify selected objects such as bananas, oranges, and apples. The project results of the classification process are presented in Figure 3. Additionally, nine students successfully completed their proposed prototype systems, using their mobile phones for data recording and testing, with one student achieving partial completion. These outcomes demonstrate that increased accessibility enhances student success.

4 Discussion

The effective implementation of the project-based teaching and learning (PBL) paradigm necessitates the careful design of projects. This process involves a thorough understanding of the scientific and engineering subjects that students need to learn, as well as an insightful assessment of their academic backgrounds. Therefore, in designing the projects, it is crucial to meticulously evaluate students' prior knowledge, interests, and abilities. The difficulty level of the projects is adjusted accordingly to foster engagement and motivation. In this context, we utilized Edge Impulse, a platform known for its efficiency in collecting, analyzing, and learning from sensor data in IoT or embedded systems. Edge Impulse aids in data sampling, feature extraction, and the creation of learning models, making it an essential tool for our curriculum.

Furthermore, to assess the effectiveness of the PBL approach, a comprehensive survey was conducted at the end of the course. This survey aimed to collect feedback from students about their learning experiences, focusing particularly on the application and relevance of the projects they engaged in. The survey results were highly positive: 85% of the students reported enhanced technical skills and understanding of the subject matter. Remarkably, 90% of respondents found the Arduino Nano BLE 33

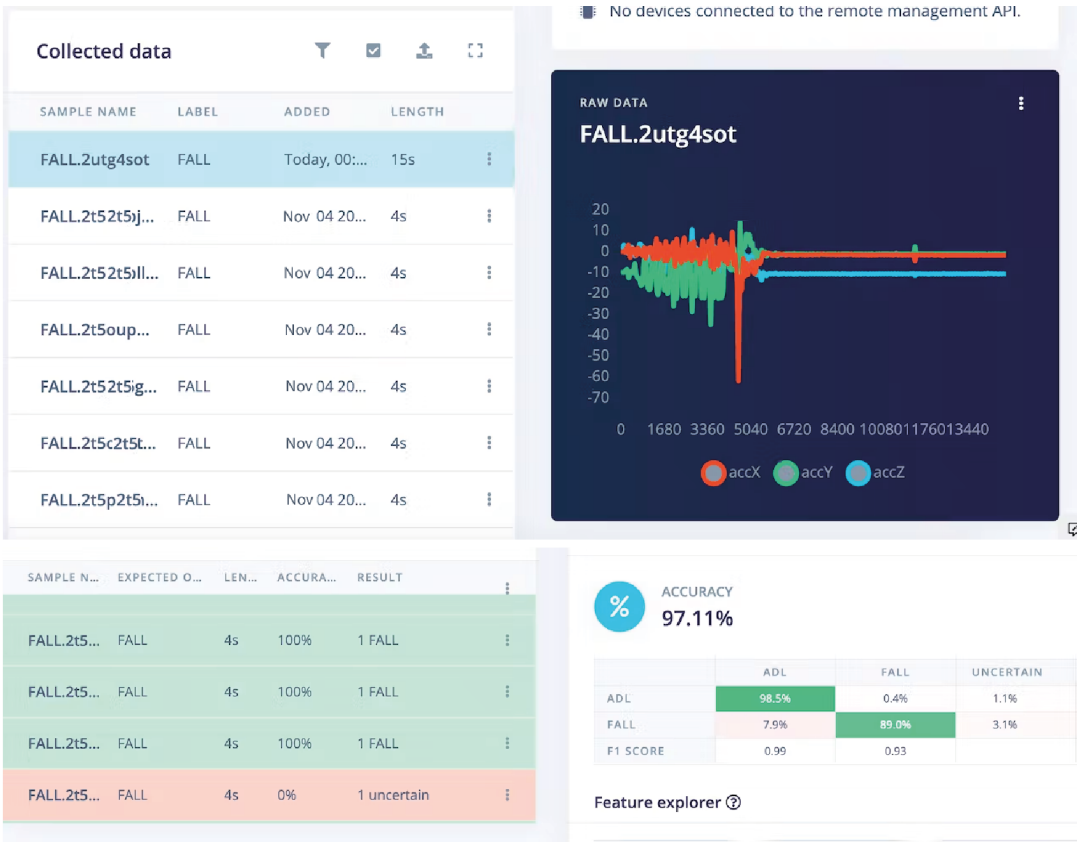

Figure 1: Student essays of Project 1

platform user-friendly, while 80% agreed that the projects aligned well with their learning styles. Additionally, 75% of the students recognized the relevance of these projects in preparing them for their future careers.

These feedbacks are invaluable as they not only validate our educational strategy but also provide critical insights for further refining our course design. Consequently, the combination of Edge Impulse and Arduino Nano BLE 33 has proven to be an innovative and effective platform, especially beneficial for students who typically have no prior hardware training or experience before taking this course. These platforms offer students opportunities to progressively develop hardware skills. Our strategy involves designing a series of projects with increasing levels of difficulty, enabling students to incrementally acquire and enhance their hardware skills.

Based on these survey findings, it is evident that the Edge Impulse and Arduino Nano BLE 33 platforms have significantly enriched student learning and experiences. The practical skills and theoretical knowledge gained through these projects are likely to be crucial in the students' future professional lives. This approach exemplifies how the use of technology in education can contribute to student success and motivation.

5 Conclusions

In this article, we have shared our experiences with the use of the Arduino Nano BLE 33 platform in a university course focused on Edge Impulse for students. The platform has been instrumental in providing an engaging and dynamic learning environment, well-suited to the course's demands. The potential of the prototype systems developed by the students in being transformed into practical biomedical products has been clearly demonstrated at the end of the course.

Through our project-based teaching and learning paradigm, we have observed significant development in students' abilities to successfully complete projects using the Edge Impulse technology on the Arduino Nano BLE 33 platform. Students not only acquired skills but were also able to generate new ideas and implement them effectively. Based on these observations, we strongly recommend the incorporation of the Arduino Nano BLE 33 platform into courses that aim to enhance students' practical and theoretical knowledge in similar fields. The platform not only supports the educational objectives but also stimulates innovation and creativity among students, making it an invaluable tool for educational purposes.

Authors' Contributions

Yeliz Durgun (YD) and Mahmut Durgun (MD) collaboratively designed the structure of the study. YD conceived the idea and was responsible for executing the field research along with laboratory analyses. MD fabricated the device, carried out the

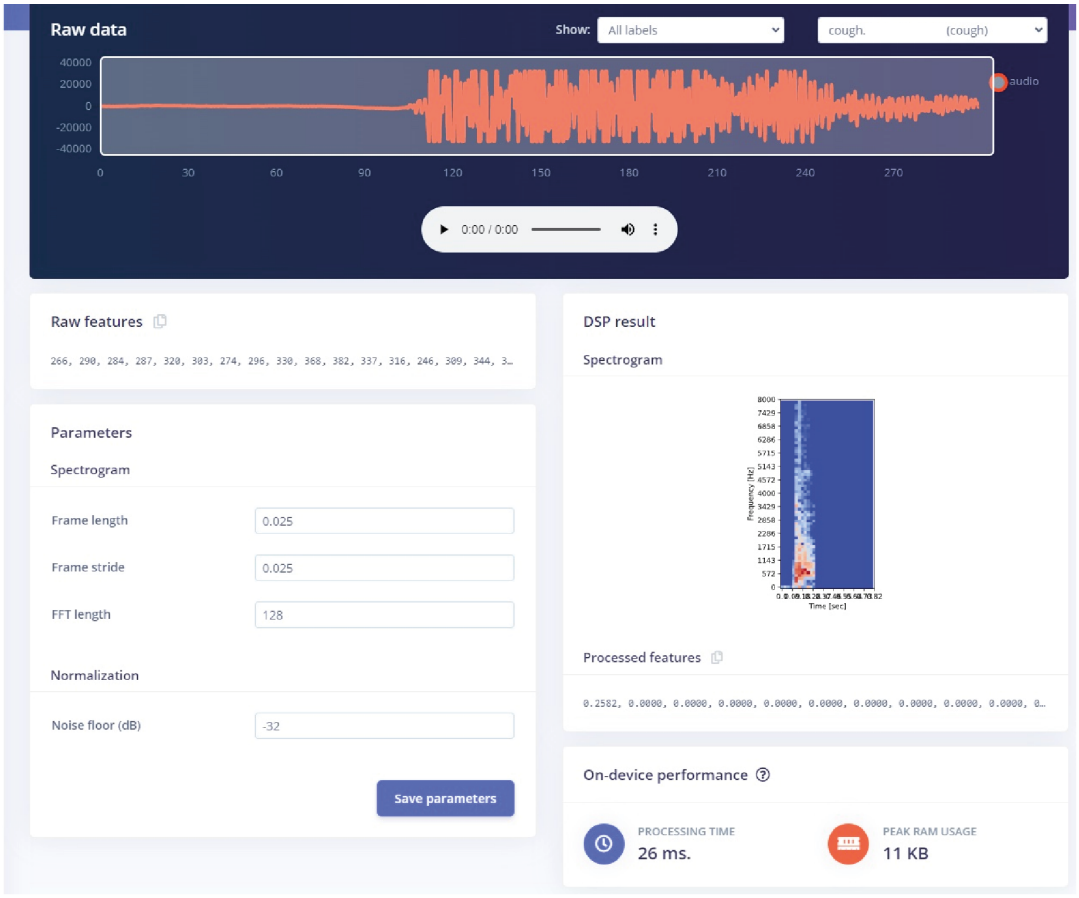

Figure 2: Student essays of Project 2

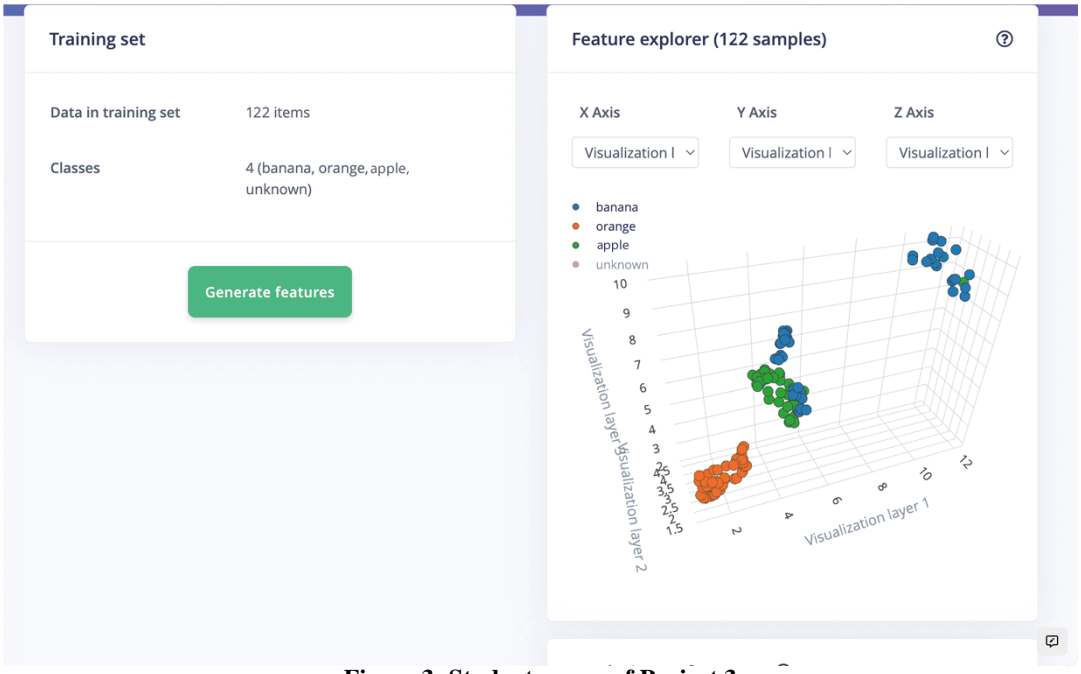

Figure 3: Student essays of Project 3

experimental work, performed the theoretical calculations in collaboration with YD, and took the lead in writing the manuscript. Both authors have read and approved the final manuscript.

Competing Interests

The authors declare that they have no conflict of interest.

References

[1] S. Chen *et al.*, ''Internet of things based smart grids supported by intelligent edge computing,'' *IEEE Access*, vol. 7, pp. 74 089–74 102, 2019.
[2] M. Hartmann, U. S. Hashmi, and A. Imran, ''Edge computing in smart health care systems: Review, challenges, and research directions,'' *Trans. Emerg. Telecommun. Technol.*, vol. 33, no. 3, p. e3710, 2022.
[3] Z. Ning *et al.*, ''Mobile edge computing enabled 5g health monitoring for internet of medical things: A decentralized game theoretic approach,'' *IEEE J. Sel. Areas Commun.*, vol. 39, no. 2, pp. 463–478, 2020.
[4] S. S. Tripathy *et al.*, ''A novel edge-computing-based framework for an intelligent smart healthcare system in smart cities,'' *Sustainability*, vol. 15, no. 1, p. 735, 2022.
[5] G. Aloi, G. Fortino, R. Gravina, P. Pace, and G. Caliciuri, ''Edge computing-enabled body area networks,'' in *2018 32nd International Conference on Advanced Information Networking and Applications Workshops (WAINA)*, 2018, pp. 349–353.
[6] S. Wan, L. Qi, X. Xu, C. Tong, and Z. Gu, ''Deep learning models for real-time human activity recognition with smartphones,'' *Mob. Networks Appl.*, vol. 25, pp. 743–755, 2020.
[7] P. Verma and S. Fatima, ''Smart healthcare applications and real-time analytics through edge computing. internet things use cases healthcare ind,'' *A Rev. edge Comput. Healthc. internet things*, vol. 275, no. 276, pp. 241–270, 2020.
[8] S. U. Amin and M. S. Hossain, ''Edge intelligence and internet of things in healthcare: A survey,'' *IEEE Access*, vol. 9, pp. 45–59, 2020.
[9] M. A. Rahman and M. S. Hossain, ''An internet-of-medical-things-enabled edge computing framework for tackling covid-19,'' *IEEE Internet Things J.*, vol. 8, no. 21, pp. 15 847–15 854, 2021.
[10] V. Vakamullu, S. Trivedy, M. Mishra, and A. Mukherjee, ''Convolutional neural network based heart sounds recognition on edge computing platform,'' in *2022 IEEE International Instrumentation and Measurement Technology Conference (I2MTC)*, 2022, pp. 1–6.
[11] U. D. Ulusar, E. Turk, A. S. Oztas, A. E. Savli, G. Ogunc, and M. Canpolat, ''Iot and edge computing as a tool for bowel activity monitoring,'' in *Edge Comput. From Hype to Real.*, 2019, pp. 133–144.
[12] A. Sacco, F. Esposito, G. Marchetto, G. Kolar, and K. Schwetye, ''On edge computing for remote pathology consultations and computations,'' *IEEE J. Biomed. Heal. Informatics*, vol. 24, no. 9, pp. 2523–2534, 2020.
[13] S. M. Lehman and C. C. Tan, ''Leveraging edge computing for mobile augmented reality,'' in *Fog/Edge Comput. Secur. Privacy, Appl.*, 2021, pp. 327–353.
[14] M. Elawady and A. Sarhan, ''Mixed reality applications powered by ioe and edge computing: A survey,'' in *Internet of Things—Applications and Future: Proceedings of ITAF 2019*, 2020, pp. 125–138.
[15] C. S. M. Babou, D. Fall, S. Kashihara, I. Niang, and Y. Kadobayashi, ''Home edge computing (hec): Design of a new edge computing technology for achieving ultra-low latency,'' in *Edge Computing–EDGE 2018: Second International Conference, Held as Part of the Services Conference Federation, SCF 2018, Seattle, WA, USA, June 25-30, 2018, Proceedings 2*, 2018, pp. 3–17.
[16] S. S. Keum, Y. J. Park, and S. J. Kang, ''Edge computing-based self-organized device network for awareness activities of daily living in the home,'' *Appl. Sci.*, vol. 10, no. 7, p. 2475, 2020.
[17] A. Jenifer *et al.*, ''Edge-based heart disease prediction device using internet of things,'' in *2022 International Conference on Applied Artificial Intelligence and Computing (ICAAIC)*, 2022, pp. 1500–1504.
[18] J. A. Miranda, M. F. Canabal, L. Gutiérrez-Martín, J. M. Lanza-Gutiérrez, and C. López-Ongil, ''Edge computing design space exploration for heart rate monitoring,'' *Integration*, vol. 84, pp. 171–179, 2022.
[19] M. Prabhu and A. Hanumanthaiah, ''Edge computing-enabled healthcare framework to provide telehealth services,'' in *2022 International Conference on Wireless Communications Signal Processing and Networking (WiSPNET)*, 2022, pp. 349–353.
[20] A. A. Alli and M. M. Alam, ''The fog cloud of things: A survey on concepts, architecture, standards, tools, and applications,'' *Internet of Things*, vol. 9, p. 100177, 2020.
[21] S. Boss and J. Krauss, *Reinventing project-based learning: Your field guide to real-world projects in the digital age*. International Society for Technology in Education, 2022.
[22] S. Han and K. Bhattacharya, ''Constructionism, learning by design, and project based learning,'' in *Emerg. Perspect. Learn. teaching, Technol.*, 2001, pp. 127–141.
[23] A. Steinemann, ''Implementing sustainable development through problem-based learning: Pedagogy and practice,'' *J. Prof. Issues Eng. Educ. Pract.*, vol. 129, no. 4, pp. 216–224, 2003.
[24] S. H. Hong, ''Edge impulse machine learning for embedded system design,'' *J. Korea Soc. Digit. Ind. Inf. Manag.*, vol. 17, no. 3, pp. 9–15, 2021.
[25] O. Zawacki-Richter, V. I. Marín, M. Bond, and F. Gouverneur, ''Systematic review of research on artificial intelligence applications in higher education – where are the educators?'' *Int. J. Educ. Technol. High. Educ.*, vol. 16, no. 1, p. 39, 2019.
[26] J. Sak and M. Suchodolska, ''Artificial intelligence in nutrients science research: A review,'' *Nutrients*, vol. 13, no. 2, p. 322, 2021.
[27] G. Briganti and O. L. Moine, ''Artificial intelligence in medicine: Today and tomorrow,'' *Front. Med.*, vol. 7, 2020.

El Cezeri
Journal of Science and Engineering
ISSN: 2148-3736

Research Article

Enhanced Histopathological Image Classification through the fusion of Thepade Sorted Block Truncation Code and Otsu Binarization features

Sudeep D. Thepade[1a], Ashwin Acharya[1b],
[1] Department of Computer Engineering, Pimpri Chinchwad College of Engineering, Pune, India
sudeepthepade@gmail.com

DOI : 10.31202/ecjse.1380112
Received: 23.10.2023 Accepted: 20.02.2024
How to cite this article:
Sudeep D. Thepade, Ashwin Acharya, " Enhanced Histopathological Image Classification through the fusion of Thepade Sorted Block Truncation Code and Otsu Binarization features", El-Cezeri Journal of Science and Engineering, Vol: 11, Iss:2, (2024), pp.(175-185).
ORCID: [a]0009-0007-9520-9972; [b]0000-0001-7809-4148.

Abstract : Histopathology is the branch of pathology that investigates the structure of cells and tissues of organisms at a microscopic level. Histopathological images are crucial in the decision-making process for effective therapies, determining the health of a particular biological structure and identifying diseases like cancer. With machine learning models, it may be feasible to increase the accuracy of medical data, decrease patient rate variations, and cut costs associated with medical care. Most medical scientists are drawn to such new technologies of predictive models in chronic disease forecasting. A novel approach for more accurate classification of histopathological images is proposed in this paper. The technique involves fusing the features extracted from two methods, namely Otsu's binarization and Thepade Sorted Block Truncation Code, to achieve improved results. The KIMIA Path960 dataset comprising 960 images is utilized for experimental validation with performance indicators like accuracy, specificity, and sensitivity. Ensembles of Simple Logistics, Multilayer Perceptron, Logistics Model Tree, as well as Simple Logistics, Random Forest, and Logistic Model Tree classifiers, demonstrated superior performance for the fusion of Thepade Sorted Block Truncation Code 7-ary and Otsu features, achieving an accuracy of 97.39 percent in a 10-fold cross-validation scenario.

Keywords : Histopathology, Thepade SBTC, Feature Fusion, Ensembles.

1 Introduction

According to current records, millions have died of diseases like cancer. The probability of receiving appropriate care and achieving favourable survival rates is markedly increased through early diagnosis. However, this diagnostic procedure is characterized by its protracted nature frequently engenders professional discord among pathologists. Several studies have raised concerns about the global shortage of medical professionals needed to handle the rising number of cancer patients. With cancer cases skyrocketing and a global shortfall of expert medical practitioners, machine learning can play a significant role. Machine learning (ML) algorithms can be trained to discern complex data trends, potentially revolutionizing diagnostic processes. A range of conventional ML algorithms has been applied to this problem, with varying degrees of success.

Though techniques such as X-rays and MRIs were used to diagnose cancer, biopsy remains the primary method for cancer diagnosis. Standard biopsy methods include surgical, vacuum-assisted, fine-needle aspiration, Core needle, and image-guided biopsy. The methodology involves a series of sequential steps, starting with collecting tissue or cell samples, then placing them onto a microscope slide, and concluding with applying a stain to facilitate visual differentiation. Subsequently, a diagnosis is established based on the examination of histopathological images with the knowledge of professionals. With Machine learning, this problem can be resolved. The classification of histopathological images using machine learning typically involves three key stages: classification, feature reduction, and feature extraction. A multitude of unique characteristics can be extracted from digital images, which is essential for precise categorization. The scientific literature has proposed numerous techniques for feature extraction, which are subsequently utilized for training and evaluating various machine learning algorithms. The paper presents an innovative approach to improve the classification performance of histopathological images by integrating features obtained from Otsu's binarization and Thepade SBTC methods.

Listed below are the key contributions of the presented work

- Ensemble: A methodology involving amalgamating multiple base models to form a unified predictive model that aims to optimize predictive performance.

- Feature Fusion: The method proposed uses a feature fusion of Otsu thresholding and Thepade SBTC(TSBTC) global features.
- Experimented Evaluation on the images of KIMIA Dataset: Experimentations are performed on KIMIA PATH960, which consists of images of epithelial, connective tissue and muscle.

2 Experimental Methods

2.1 Related Works

Studies on histopathological image classification have employed various techniques, including analyzing image spatial structure, classification through segmentation, and using global and window-based features. Deep feature-based classification has become increasingly popular in recent years. However, deep learning techniques necessitate intensive training and access to a balanced and extensive dataset.

Meghana et al.[1] conducted a comparative study to assess the effectiveness of different feature extraction techniques for histopathological image classification in the KIMIA Path960 dataset. The dataset consisted of 960 histopathological images belonging to 20 unique classes. The study compared the performance of bag-of-visual words (BoVW), deep features and local binary patterns (LBP) and found that LBP had an accuracy of 90.62%, deep features achieved 94.72% accuracy, and BoVW produced the highest accuracy of 96.50%. These findings highlight the superiority of BoVW over other feature extraction techniques when classifying the KIMIA Path960 dataset. This study enhances our understanding of how feature extraction affects histopathological image classification performance. In a study by Taha et al.[2], features were extracted using a pre-trained deep network, histogram of gradients and LBP from the KIMIA Path960 dataset. The extracted features were classified using standard image classification methods like artificial neural networks, decision trees and support vector machines. The findings showed that SVM yielded the highest accuracy among the three techniques at 90.52% when features were extracted using LBP. Conversely, when deep features were utilized for feature extraction, the accuracy was recorded at 81.14%. However, the results obtained using HOG were unsatisfactory.

The study by Ganguly et al. [3] investigates the influence of optimization algorithms on the accuracy of deep learning models applied to histopathological images. Two models, a pre-trained Resnet50 and a five-layer CNN, were utilized. The performance of three optimization algorithms, namely Radam, AdamW, and AdaMax, was evaluated on the KIMIA Path960 and NIA-curated lymphoma images dataset. Utilizing AdamW optimization algorithm with KIMIA Path960 dataset resulted in an accuracy of 99.9%, according to the study's findings. A slightly lower accuracy of 98.13% was achieved when the same approach was applied to the dataset of lymphoma images. The study highlights the significance of considering the optimization algorithm in conjunction with network architecture. The findings suggest that selecting the most appropriate optimization algorithm is critical in achieving optimal results in classifying histopathological images.

Anish et al.[4] utilized a pre-trained CNN for the classification of histopathological images on the KIMIA Path 960 dataset. The study aimed to explore various combinations between MobileNetV2 and GLCM (Gray-Level Co-occurrence Matrix) for histopathological image classification. The study revealed that combining the Mean of Sorted Gray Values and GLCM performed better than the other methods, with an AUC (Area Under the Curve) score of 0.999. Furthermore, the approach exhibited impressive results concerning F1 score (0.951), Precision (0.951), and Recall (0.951), emphasizing the potential of this method for improving diagnostic tools for cancer detection.

In a study by Rania et al. [5], the authors utilized the HOG feature extractor to computationally derive features from histopathological images, explicitly focusing on identifying invasive ductal carcinoma. A random subset of images, specifically 100, 200, 400, 1000, and 2000, was chosen from the histopathology dataset. These extracted statistical features were then utilized to train a range of ML algorithms. The study's primary objective was to discern between cancerous and noncancerous growth depicted in the histopathology images. The algorithms' performance was evaluated using various assessment metrics, such as AUC, F1 Score, precision, sensitivity, and accuracy. Notably, the algorithms demonstrated optimal performance when the number of images was restricted to 100, while their effectiveness diminished with a more significant number of images.

Irum et al. [6] proposed Pa-DBN-BC, a patch-based deep-learning method for histopathological image classification in breast cancer diagnosis. The method employs a Deep Belief Network (DBN) and utilizes logistic regression for image classification. The method proposed achieved an accuracy of 86%, outperforming previous deep learning methods. The authors attribute this superior performance to the ability of the method to automatically learn the best features, which sets it apart from traditional classification methods. BCHisto-Net was proposed to classify breast histopathological images at a hundred times magnification by Rashmi et al.[7] The proposed system classified breast histopathological images based on global and local features. The features were combined by a proposed feature aggregation branch, which was used to classify 100 images. The effectiveness of integrating the global and local features was observed in the paper as it accomplished an overall accuracy of 89% and 95% on the BreakHis and KMC datasets, respectively. Table 1 gives a gist of all the related work.

Despite the application of diverse techniques for histopathological image analysis in previous works, such as the examination of spatial structure, classification through segmentation, and the utilization of global and window-based features, feature fusion

Table 1: Related Works - Summary

Authors	Year of Publication	Dataset	Methodology	Advantage	Limitation
Meghana et al. [1]	2017	KIMIA Path960	LBP, Deep Features, BoVW	The automatic extraction of features is performed by Deep learning after the completion of data training	Deep Features need extensive training to achieve high accuracy.
Taha et al. [2]	2018	KIMIA Path960	Classification using SVM, Decision Tree and ANN on LBP, HOG and deep features	LBP offers significant advantages in discrimination and computational efficiency	HOG yielded unsatisfactory results due to model underperformance.
Ganguly et al. [3]	2020	KIMIA Path960, NIA dataset of lymphoma images	Pretrained Resnet50 model customized with several optimization algorithms, layered CNN	The model's extensive 23+ million trainable parameters enhance its efficacy in image recognition	Training Residual Neural Networks (ResNet) is time and resource-intensive.
Anish et al. [4]	2021	KIMIA Path960	Neural Networks + Gray-Level Co-Occurrence Matrix + Mean of sorted grey values	It exhibits a higher capacity to execute intricate tasks than other algorithms	It demands a substantial volume of data and entails significant computational costs.
Rania et al. [5]	2022	IDC subtype of breast cancer images	Statistical features extracted using HOG features extractor	The proposed method is easy to set up and operate	Performance of the model decreases when the number of images increases.
Rashmi et al. [7]	2021	BreakHis and KMC dataset	CNN-based architecture called BCHisto-Net	Global and local features extracted were combined by a feature aggregation branch	Relatively new; hence, not much research has been done on this method.

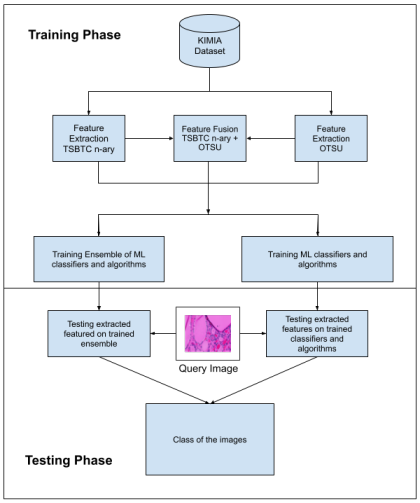

Figure 1: Block Diagram of the Proposed System

or combining both local and global features has yet to be explored extensively. Additionally, considering ensemble classifiers rather than individual ones has not been thoroughly investigated.

2.2 Proposed System

The method proposed for classifying Histopathological images consists of a training and Testing phase. Figure **??** gives an overview of the same. The extraction of image features during the training phase involves the utilization of Thepade SBTC n-ary and Otsu thresholding algorithms. Also, a fusion of extracted features from Thepade SBTC and Otsu thresholding is considered. Individual ML algorithms and classifiers and the ensemble of several classifiers and algorithms are then trained with the extracted features.

The trained classifiers and algorithms are then used to test the extracted features from the query image. The image class is identified, and the correctness accuracy is calculated. Other performance metrics, like Specificity, Sensitivity, True Positive

Rate (TPR), and False Positive Rate (FPR), are also considered.

The features extraction algorithms TSBTC, Otsu's thresholding, the machine learning algorithms and classifiers and feature fusion are further elaborated in the following subsections.

a. Thepade's Sorted Block Truncation Code (TSBTC) [8][9][10] **:**

Consider a histopathological image of size p x q and let R, G, and B represent red, green and blue planes, respectively. Each plane is then converted to a one-dimensional vector and sorted in increasing order. Each vector is divided into N distinct parts where N refers to the N-ary in Thepade SBTC N-ary. The feature vector comprises the centroid of each N part for the colour plane. So, in general, the feature vector will be composed of R_1, R_2, R_3, . . ., R_N, G_1, G_2, G_3, . . ., G_N, B_1, B_2, B_3, . . ., B_N. The general formula for calculating any R_i can be given as

$$R_i = \frac{N}{pq} \sum_{k=(i-1)\frac{pq}{N}}^{(i)\frac{pq}{N}} V_r\,[k] \tag{1}$$

Where V_r is the one-dimensional vector for the red plane sorted in increasing order, pq is the dimension of the image, and N represents the nth ary in Thepade SBTC n-ary. Similarly

$$B_i = \frac{N}{pq} \sum_{k=(i-1)\frac{pq}{N}}^{(i)\frac{pq}{N}} V_b\,[k] \tag{2}$$

$$G_i = \frac{N}{pq} \sum_{k=(i-1)\frac{pq}{N}}^{(i)\frac{pq}{N}} V_g\,[k] \tag{3}$$

Where V_b and V_g are the one-dimensional vectors sorted in increasing order for the blue and green planes, respectively

b. Otsu Thresholding Algorithm [11][12]:

Otsu's algorithm disregards the heterogeneity and variousness of the background, assuming the image comprises just the background and foreground(object). To address the issue of overlapping class distributions, the Otsu method employs a threshold to divide the image into two sections: P_0 (representing darker pixels) and P_1 (representing lighter pixels). P_0 is characterized by intensity levels ranging from 0 to t, denoted as P_0 = 0, 1, ..., t, while P_1 encompasses intensity levels from t to l-1, denoted as P_1 = t, t + 1, ..., l - 1, l. Here, t represents the threshold value, and l denotes the highest grey level of the image (e.g., 256). It is worth noting that P_0 and P_1 can be set to either foreground and background or vice versa, as the light region does not necessarily correspond to the object. This method involves an exhaustive examination of all possible threshold values to determine the optimal division between P_0 and P_1 based on the minimum pixel intensity values for each side of the threshold.

Given: For the observed grey value i=1, ..., l, the histogram probabilities are given as H(i)

$$H\,(i) = \frac{number\,\{(r,c)\ \mid image(r,c) = i\}}{(R,C)} \tag{4}$$

The column and row indices of the image are represented by c and r, respectively, while the number of columns and rows in the image are represented by C and R, respectively. The variance, mean, and weight of class T0 with intensity from 0 to t is given by $\sigma_b^2\,(t)$, $\mu_b\,(t)$, and $w_b\,(t)$, respectively.

The variance, mean, and weight of class T1 with intensity from t+1 to 1 are given $\sigma_f^2\,(t)$, $\mu_f\,(t)$, and $w_f\,(t)$, respectively.

σ_w^2 is the tallied average of the group variances. The value with the lowest within-class variance is the ideal threshold value, or t*. The within-class variance can be represented as follows:

$$\sigma_w^2\ = w_b\,(t) *\ \sigma_b^2\,(t)\ + w_f\,(t)\ * \sigma_f^2\,(t) \tag{5}$$

Where,

$$w\,(t) = \Sigma_{i=1}^{t}\ H\,(i) \tag{6}$$

$$w_f\,(t) = \Sigma_{i=t+1}^{l}\ H\,(i) \tag{7}$$

$$\mu_b\,(t) = \frac{\Sigma_{i=1}^{t}\ i * H\,(i)}{w_b\,(t)} \tag{8}$$

$$\mu_f(t) = \frac{\Sigma_{i=t+1}^{l} \; i * H(i)}{w_f(t)} \tag{9}$$

$$\sigma_b^2(t) = \frac{\Sigma_{i=1}^{t} (i - \mu_b(t))^2 * H(i)}{w_b(t)} \tag{10}$$

$$\sigma_f^2(t) = \frac{\Sigma_{i=t+1}^{t} (i - \mu_f(t))^2 * H(i)}{w_f(t)} \tag{11}$$

After obtaining t*, the input image $I(r,c)$ is segmented as

$$S(R,C) = \begin{cases} 1, & \text{if } I(r,c) > t* \\ 0, & \text{if } I(r,c) \leq t* \end{cases} \tag{12}$$

Utilizing the segmentation result $S(R,C)$, the intensity values of the input image $I(R,C)$ are partitioned into two clusters, facilitating the generation of the feature vector $[O1, O2]$, as delineated in equations 13 and 14.

$$O1 = \frac{1}{\sum_{i=1}^{r} \sum_{j=1}^{c} S(i, \; j)} \sum_{i=1}^{r} \sum_{j=1}^{c} I(i,j) * S(i, \; j) \tag{13}$$

$$O2 = \frac{1}{\sum_{i=1}^{r} \sum_{j=1}^{c} (1 - S(i, \; j))} \sum_{i=1}^{r} \sum_{j=1}^{c} I(i,j) * (1 - S(i, \; j)) \tag{14}$$

In this study, color images sourced from the KIMIA Path960 dataset are examined. The individual Red, Green, and Blue color channels of these images are isolated, yielding an Otsu Thresholding-based feature vector $[OR1, OR2, OG1, OG2, OB1, OB2]$ for each image in the dataset.

c. Feature Fusion of Thepade SBTC and Otsu Thresholding features of Histopathological images[13][14]:

The fusion of Thepade SBTC n-ary features and Otsu's thresholding is employed to achieve feature fusion for the classification of histopathological images. Considering a histopathological image with R, G and B representing the Red, Green, and Blue colour planes, respectively, the feature fusion vector combining Otsu's thresholding features and Thepade SBTC n-ary features can be denoted as [TR_1, TR_2, . . ., TR_n, TG_1, TG_2, . . ., TG_n, TB_1, TB_2, . . ., TB_n, OR_1, OR_2, OG_1, OG_2, OB_1, OB_2], where TR_i, TG_i and TB_i represent features of TSBTC n-ary while the rest represent features extracted using Otsu's Thresholding algorithm. Thus, it can be said that the feature vector will have the size 3n+6 where n is from TSBTC n-ary.

d. ML Classifiers and Algorithms Used:

Simple Logistics, Logistic Model Tree (LMT), KStar, Random Forest, Multilayer perceptron, IBK, Bayes' Net, Naive Bayes

e. Ensemble:

The ensemble is a machine learning methodology that involves amalgamating multiple base models to form a unified predictive model that aims to optimize predictive performance. Combining many models, an ensemble improves ML outcomes. Instead of using one single model, ensembles enable better prediction performance.

f. Majority Voting:

The majority voting technique integrates predictions from several machine learning models and ensembles to enhance model performance. By aggregating the results of different models, this method aims to produce superior outcomes compared to any single model used in the ensemble.

2.3 Experimentation Environment

The histopathological image classification method proposed is accomplished in Python with the help of Weka tool. The KIMIA Path960 dataset is considered for the entire experimentation. The dataset employed in this study comprises 400 images of various tissue types, including connective, muscle, and epithelial tissues. From these images, 20 scans representing distinct classes are selected, and 48 regions of interest of equal size are extracted from each whole slide image. These regions are then down-sampled to 308x168 patches for further analysis. Hence, a total of 960 (20x48) images are obtained. The images are saved as colour Tagged Image File (TFF) files. Figure **??** displays a subset of the images from the dataset.

The performance appraisal of all variations is done using percentage accuracy, Sensitivity, and Specificity. The values of these performances depend on False Positive, False Negative, True Positive, True Negative where,

TP - True Positive: When the histopathological picture is correctly identified, the outcome is a true positive.

FP - False Positive: When the histopathological picture is wrongly identified, the consequence is a false positive.

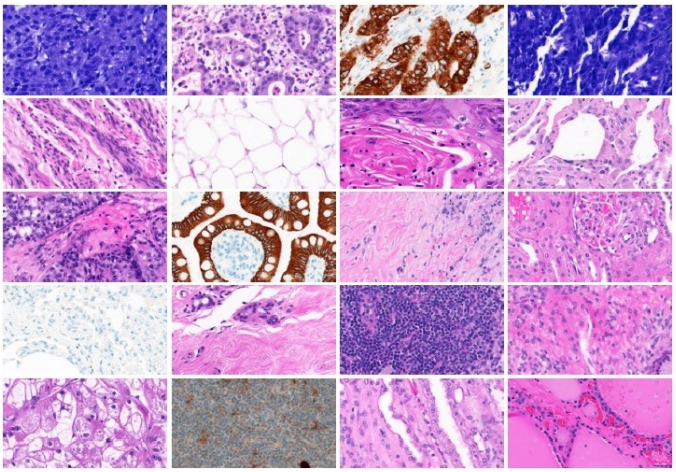

Figure 2: Samples from the KIMIA PATH960 dataset

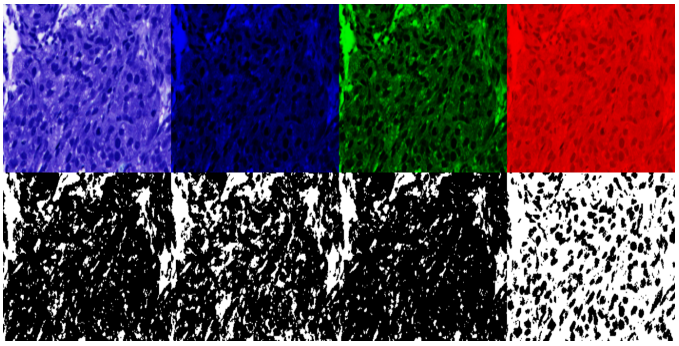

Figure 3: Binarized image of a sample from the dataset using Otsu's Thresholding Algorithm

TN - True Negative: It is an outcome in which the technique accurately detects the histopathological image that does not fit into the class of the image considered.

FN - False Negative: When a method mistakenly classifies a histopathological image as not in its original category, the result is a False Negative.

Then, the formulae for Specificity, Sensitivity, and accuracy can be given as follows:

$$Sensitivity = \frac{TP}{FN + TP} = TPRate \tag{15}$$

$$Accuracy = \frac{TP + TN}{TP + FP + FN + TN} \tag{16}$$

$$Specificity = \frac{TN}{TN + FP} = 1 - FPRate \tag{17}$$

3 Results and Discussions

The technique proposed experiments on 960 images of the KIMIA PATH960 dataset, where Thepade SBTC N-ary and Otsu thresholding algorithms are used for extracting global features. Twelve ML algorithms and eight ensembles are then used to train and test the features.

The percentage accuracy for histopathological image classification for TSBTC n-ary global features for twelve ML algorithms, namely SMO, Naive Bayes, Bayes' Net, Simple Logistics, Random Tree, Multilayer Perceptron, Random Forest, LMT, REPTree, KStar, IBK and J48 is shown in the table 1.

It can be inferred from Table 2 that the performance of Thepade SBTC bests Otsu's Thresholding for nearly all classifiers. The peak classification accuracy for the features extracted using TSBTC is 97.29% for TSBTC 7-ary with the LMT classifier, while the highest for Otsu's features was 94.48% with the LMT classifier. The graphical representation of the above data sheds further light on the performance of each feature extractor with individual classifiers. Figure **??** shows that for each classifier, the percentage accuracy for the features extracted using TSBTC n-ary increases from 2- ary to 7-ary and remains almost constant

Table 2: Percentage Accuracy for TSBTC N-ary and Otsu for different classifiers

Classifiers	2ary	3ary	4ary	5ary	6ary	7ary	8ary	9ary	10ary	Otsu
SMO	70.42	74.69	80.21	82.29	83.96	85.00	85.42	86.56	87.19	72.40
Bayes' Net	79.79	83.13	84.27	84.48	85.73	85.21	85.73	86.35	87.03	77.81
Naive Bayes	80.21	83.96	85.31	85.94	86.35	86.56	86.77	86.88	86.88	79.79
REPTree	81.46	82.81	83.96	86.25	86.04	85.42	86.98	85.83	87.64	81.56
LMT	93.54	95.94	96.46	96.56	96.25	97.29	96.56	96.88	96.67	94.48
SimpleLogistic	93.75	95.10	95.94	96.56	95.94	96.67	96.56	96.67	96.04	92.19
MultilayerPerceptron	93.33	93.65	95.21	95.63	95.10	95.31	95.21	95.94	96.35	88.75
RandomForest	90.63	91.77	93.13	94.06	94.17	94.27	94.48	95.79	94.48	88.44
KStar	90.31	92.19	92.60	93.54	93.85	94.38	94.27	94.27	94.48	88.44
lBk	90.21	91.25	92.71	93.13	93.02	93.23	93.23	93.23	93.54	89.48
J48	86.15	86.56	88.44	88.65	89.69	90.63	88.85	88.23	88.75	83.23
RandomTree	84.69	87.71	85.83	85.94	88.23	86.56	88.85	88.96	89.48	82.40

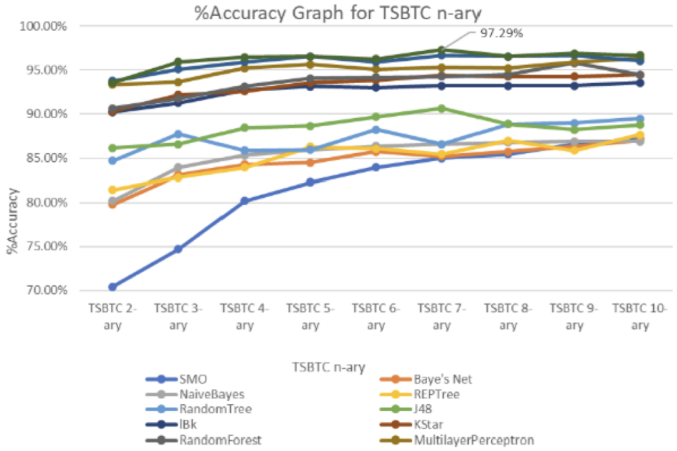

Figure 4: Performance Comparison of ML classifiers for Thepade SBTC n-ary

from 8-ary onwards. Also, it is worth noting that the classifiers KStar, RandomForest, Multilayer Perceptron, Simple Logistic and LMT gave better classification accuracies than the rest.

When the global features extracted from TSBTC and Otsu's Thresholding were fused, trained, and tested on the twelve classifiers, no performance amelioration was observed compared to TSBTC n-ary. The highest accuracy of 97.29% was obtained for the features of TSBTC 5-ary and Otsu with LMT classifier, which is the same for TSBTC 7-ary as observed before. Figure **??** shows a graphical representation of the same.

From Figure **??** and Figure **??**, it can be contemplated that the classifiers of KStar, Random Forest, Simple Logistic, Multilayer Perceptron, and Logistic Model Tree (LMT) performed better than the rest. Hence these classifiers are considered to form 8 distinct ensembles, namely – 'Logistic Model Tree+Simple Logistic+Multilayer Perceptron+Random Forest+KStar (LMT+SL+MP+RF+KS)', 'Simple Logistic+Multilayer Perceptron+Random Forest+Logistic Model Tree (SL+MP+RF+LMT)', 'Simple Logistic+Multilayer Perceptron+Random Forest (SL+MP+RF)', 'Simple Logistics+ Multilayer Perceptron+LMT (SL+MP+LMT)', 'Simple Logistic+Logistic Model Tree +Random Forest (SL + LMT + RF)', 'Simple Logistic+Logistic Model Tree (SL+LMT)', 'Simple Logistic+Multilayer Perceptron (SL+MP)', 'Random Forest+Simple Logistic (RF+SL).'

The extracted features are then trained and tested with the ensemble of classifiers to analyze performance improvement. Tables 3, 4 and 5 depict the result when ensembles are used to train and test the features extracted using TSBTC n-ary, Otsu and fusion of TSBTC and Otsu, respectively.

According to Table 3, the ensembles of LMT + Simple Logistics + Multilayer Perceptron + Random Forest + KStar and

Table 3: Performance (Accuracy) of Thepade SBTC n-ary for different ensembles

Classifiers	2ary	3ary	4ary	5ary	6ary	7ary	8ary	9ary	10ary
LMT + SL + MP + RF + KS	95.10	95.73	96.67	96.77	97.08	97.29	96.88	97.08	96.88
SL + MP + RF + LMT	95.10	96.15	96.98	96.77	96.98	97.29	97.08	97.08	96.98
SL + MP + RF	94.90	95.00	96.04	96.56	96.35	96.88	96.67	97.08	96.98
SL + MP	93.75	95.42	96.67	96.04	96.56	96.56	96.98	96.88	96.35
SL + RF	94.27	95.21	95.94	96.46	96.88	97.08	96.98	96.98	96.25
SL + RF + LMT	94.48	95.94	96.46	96.67	96.25	96.98	96.56	96.98	96.56
SL + LMT	93.85	96.04	96.56	96.67	96.46	97.08	96.56	96.98	96.46
SL + MP + LMT	94.79	95.94	96.77	96.56	96.25	97.19	96.56	96.88	96.67

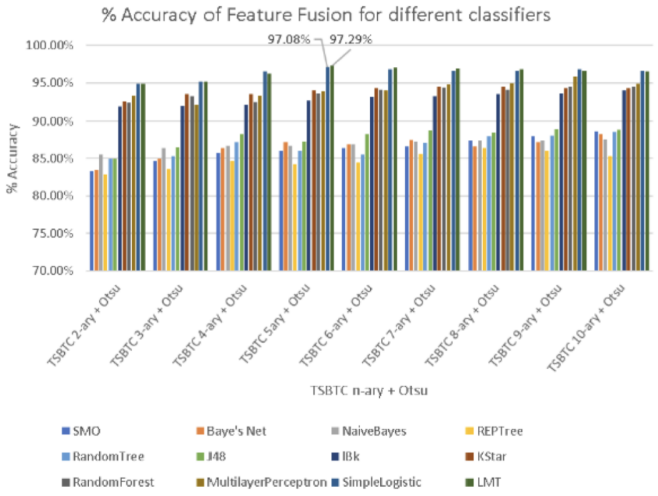

Figure 5: Performance Comparison of ML classifiers for the fusion of TSBTC n-ary + Otsu features

Table 4: Accuracy of Otsu for different ensembles

Classifiers	Otsu
LMT + SL + MP + RF + KS	92.3958
SL + MP + RF + LMT	93.8542
SL + MP + RF	91.8750
SL + RF + LMT	93.8542
SL + MP + LMT	93.9583
SL + MP	91.1458
SL + LMT	94.2708
SL + RF	93.0208

Simple Logistics + Multilayer Perceptron + Random Forest + LMT performed better for TSBTC 7-ary features, achieving an accuracy of 97.29%. Notably, the performance with ensemble learning was still the same as the highest accuracy achieved with the individual classifiers using Thepade SBTC n-ary features. From Tables 2 and 3, it can be concluded that Thepade SBTC 7-ary outperformed the other feature extractors with both individual classifiers and ensembles. A comparison of the best-performing Thepade SBTC 7-ary with the best-performing classifiers and ensembles is presented in Figure **??**. Although the ensemble of classifiers outperformed most individual classifiers, it is still evident from Figure **??** that further improvement is required to achieve the highest accuracy.

Ensemble learning was ineffective for the features extracted using Otsu's Thresholding, as the performance did not improve when an ensemble of classifiers was used. The highest accuracy obtained in this case was 94.27% for the Simple Logistic and LMT classifiers ensemble, which was lower than the 94.48% accuracy achieved by the LMT classifier alone, as shown in Table 2.

Nevertheless, the application of ensemble learning demonstrated notable success when combining Thepade SBTC and Otsu

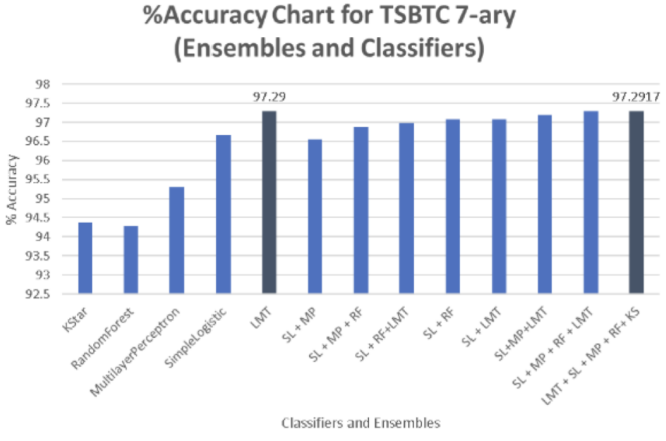

Figure 6: Performance comparison of ML classifiers and ensemble of classifiers for TSBTC 7-ary

Table 5: Performance (Accuracy) of TSBTC n-ary with various ensemble of classifiers

Classifiers	2ary	3ary	4ary	5ary	6ary	7ary	8ary	9ary	10ary
LMT + SL + MP + RF + KS	95.83	95.73	96.56	96.77	96.46	97.29	96.77	96.77	96.67
SL + MP + RF + LMT	96.15	95.83	96.67	97.08	97.08	97.29	96.77	96.98	96.35
SL + MP + RF	95.21	95.10	96.15	96.15	96.04	96.88	96.46	96.56	96.04
SL + MP	95.10	95.31	96.25	96.25	96.56	97.08	96.67	96.56	96.35
SL + RF	95.63	95.31	96.46	96.56	96.88	97.08	96.77	96.77	96.77
SL + RF + LMT	95.63	95.83	96.88	97.19	96.88	97.39	96.67	96.77	96.67
SL + LMT	95.31	95.31	96.56	97.08	96.98	97.29	96.67	96.56	96.67
SL + MP + LMT	95.52	95.94	96.88	97.08	97.08	97.39	96.67	96.98	96.67

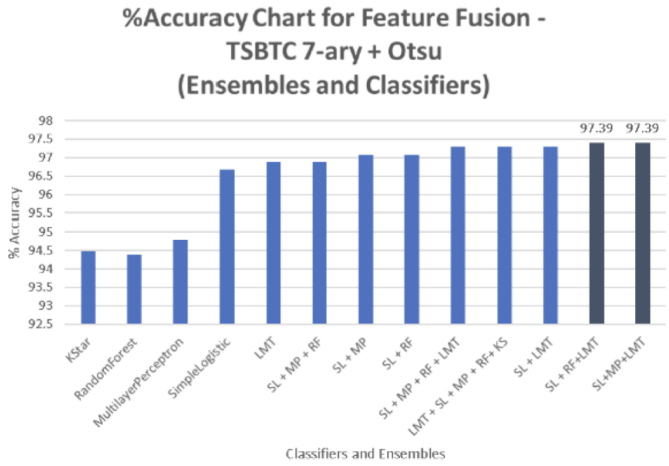

Figure 7: Performance comparison of ML classifiers and ensemble of classifiers

features. From the results in Table 3, it can be observed that for feature fusion, better performance was obtained with ensembles of Simple Logistic, Multilayer Perceptron, and Logistics Model Tree, as well as with ensembles of Simple Logistic, Random Forest, and LMT classifiers. These ensembles achieved an accuracy of 97.39%, which outperformed the accuracy obtained with the LMT classifier alone for the same features. A comparison chart of the classification accuracy for 7-ary + Otsu with the best classifiers and ensembles is shown in Figure **??**.

While ensemble learning did not yield significant improvements for features extracted by TSBTC or Otsu, it did demonstrate performance improvements for a fusion of the features extracted through these techniques. It is important to note that the fusion of features obtained through Otsu and TSBTC 7-ary with the aforementioned ensembles achieved the best overall performance compared to all other feature extraction techniques described in the research.

From all the graphs and tables, it can be implied that among TSBTC n-ary features, the features extracted by TSBTC 7-ary performed better than the rest when tested with both individual as well as ensemble of classifiers. Though global features were extracted using TSBTC and Otsu, the features extracted using TSBTC performed better than that of Otsu. When the global features extracted through the aforementioned algorithms were combined, the feature fusion performed better than the rest of the ensemble of classifiers. Though 5-ary + Otsu features with LMT classifier performed better than the rest with individual classifiers, an ensemble of classifiers with feature fusion of TSBTC 7-ary + Otsu bettered it. A comparison of 7-ary, Otsu and 7-ary + Otsu features for different ensembles and best classifiers is shown in figure **??**.

Performance metrics like specificity, sensitivity and f-measure were also considered to investigate the performance further. A graphical plot of the same is shown in Figure **??**.

The feature fusion exhibited the highest precision, Recall, sensitivity, and specificity values, as observed in Figure **??**. In comparison, using individual features of Thepade SBTC 7-ary or Otsu yielded lower values. The chart further reinforces the notion that feature fusion does help in the classification of histopathological images.

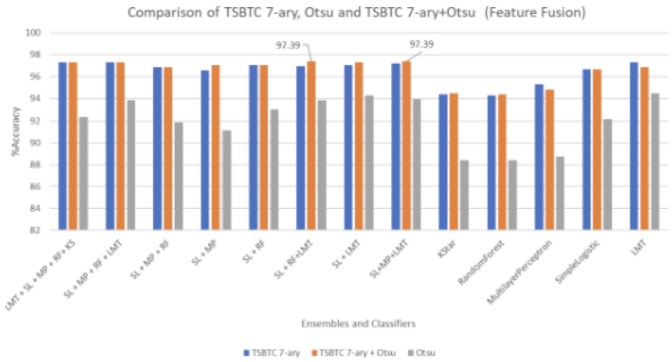

Figure 8: Comparison of TSBTC 7-ary, Otsu and TSBTC 7-ary + Otsu (feature fusion)

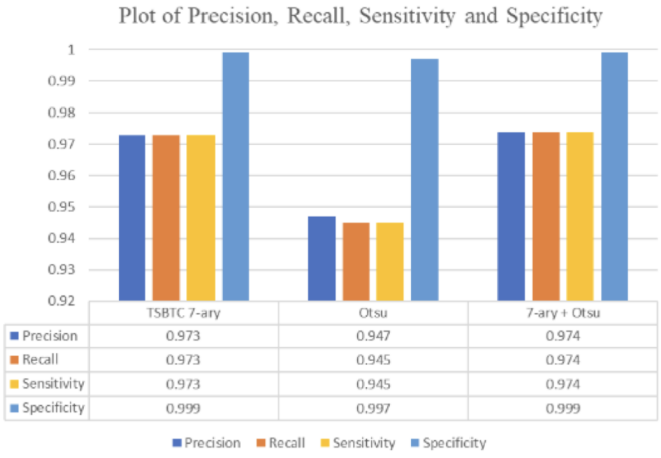

Figure 9: Plot of precision, recall, sensitivity and specificity for TSBTC 7-ary, Otsu and TSBTC 7-ary + Otsu

Table 6: Comparison of all related work on KIMIA path 960 dataset

Authors	Methodology	Dataset	Technique employed	Performance metrics	
Meghna et al. [1]	LBP, BoVW, CNN	KIMIA Path960	BoVW	Accuracy	96.50%
			LBP	Accuracy	90.62%
			Deep features	Accuracy	94.72%
Taha et al. [2]	Deep Features, HOG and LBP	KIMIA Path960	SVM + LBP feature	Accuracy	90.52%
			SVM + deep features	Accuracy	81.14%
			ANN + HOG	Accuracy	34.37%
Ganguly et al. [3]	Optimization Algorithms in Combination with Deep Learning Models	KIMIA Path960	ResNet50 + Radam	Accuracy	99.27%
			ResNet50 + AdaMax	Accuracy	99.79%
			ResNet50 + Adam	Accuracy	99.77%
			ResNet50 + AdamW	Accuracy	99.90%
Anish et al. [4]	Feature Blending	KIMIA Path960	Sorted gray value Mean + GLCM + NN	Recall	0.951
				Precision	0.951
				F1 score	0.951
				AUC	0.999
			Sorted gray value Mean + GLCM + RF	Recall	0.926
				Precision	0.927
				F1 score	0.926
				AUC	0.997
			Sorted gray value Mean+ GLCM + SVM	Recall	0.917
				Precision	0.919
				F1 score	0.916
				AUC	0.998
Proposed Method	Fusion of TSBTC and Otsu features	KIMIA Path960	Ensemble of SL + MP + LMT with TSBTC 7-ary Otsu features	Specificity	0.999
				Sensitivity	0.974
				Accuracy	97.39%
			Ensemble with Thepade SBTC 7-ary features	Specificity	0.999
				Sensitivity	0.973
				Accuracy	97.29%
			LMT with Otsu features	Specificity	0.997
				Sensitivity	0.947
				Accuracy	94.70%

4 Conclusions

Feature extraction is a crucial step in the classification of histopathological images. Literature has given several feature extraction techniques. This paper proposes Thepade SBTC and Otsu Binarization techniques for feature extraction. The fusion of these features is also considered to enhance the classification accuracy of histopathological images. Also, in an attempt to create a more robust model for accurate prediction, ensembles of classifiers were considered. It was observed from the experimentation that almost all classifiers and ensemble combinations gave better performance for the global features extracted using Thepade SBTC in comparison to Otsu. The classification accuracy was improved when the features were combined, and the resultant features were trained and tested using ensemble of classifiers. Better performance is observed by ensembles of Simple Logistics, Multilayer Perceptron, Logistics Model Tree and also Simple Logistics, Random Forest, and LMT classifiers for the fusion of TSBTC 7ary and Otsu features with an accuracy of 97.39% in 10-fold cross-validation scenario. The results emphasize the optimality of feature fusion and ensemble learning in the classification of histopathological images. Additionally, the application of this method to classify histopathological images, particularly in the context of diseases like cancer, presents an exciting opportunity for future investigations.

5 Authors' Contributions

Sudeep T. contributed to the ideation phase, conceptualizing the research framework and generating initial ideas. Implementation, experimental explorations, analysis, and drafting were all equally contributed by both authors, Sudeep T. and Ashwin A. Both authors equally invested in the integrity and quality of the research presented.

6 Competing Interests

The authors declare that they have no competing interests.

References

[1] M Dinesh Kumar, M Babaie, S Zhu, S Kalra, and HR Tizhoosh. A comparative study of cnn, bovw and lbp for classification of histopathological images. In *IEEE Symposium Series on Computational Intelligence (SSCI)*, pages 1–7, 2017.

[2] TJ Alhindi, S Kalra, KH Ng, A Afrin, and HR Tizhoosh. Comparing lbp, hog and deep features for classification of histopathology images. In *International Joint Conference on Neural Networks (IJCNN)*, pages 1–7, 2018.

[3] A Ganguly, R Das, and SK Setua. Histopathological and lymphoma image classification using customized deep learning models and optimization algorithms. In *11th International Conference on Computing, Communication and Networking Technologies (ICCCNT)*, pages 1–7, 2020.

[4] A Anurag, R Das, GK Jha, SD Thepade, N D'Souza, and C Singh. Feature blending approach for efficient categorization of histopathological images for cancer detection. In *IEEE Pune Section International Conference (PuneCon)*, pages 1–6, 2021.

[5] RR Kadhim and MY Kamil. Evaluation of machine learning models for breast cancer diagnosis via histogram of oriented gradients method and histopathology images. *International Journal on Recent and Innovation Trends in Computing and Communication*, (10), 2022.

[6] I Hirra, M Ahmad, A Hussain, MU Ashraf, IA Saeed, SF Qadri, AM Alghamdi, and AS Alfakeeh. Breast cancer classification from histopathological images using patch-based deep learning modelling. *IEEE Access*, 9:24273–24287, 2021.

[7] R Rashmi, K Prasad, and CBK Udupa. Bchisto-net: Breast histopathological image classification by global and local feature aggregation. *Artificial Intelligence in Medicine*, 121:102191, 2021.

[8] S Khairnar, SD Thepade, and S Gite. Effect of image binarization thresholds on breast cancer identification in mammography images using otsu, niblack, burnsen, thepade's sbtc. *Intelligent Systems with Applications*, 2021.

[9] SD Thepade and Y Bafna. Improving the performance of machine learning classifiers for image category identification using feature level fusion of otsu segmentation augmented with thepade's n-ary sorted block truncation coding. In *2018 Fourth International Conference on Computing Communication Control and Automation (ICCUBEA)*, pages 1–6, 2018.

[10] S. D. Thepade and P. R. Chaudhari. Land usage identification with fusion of thepade sbtc and sauvola thresholding features of aerial images using ensemble of machine learning algorithms. *Applied Artificial Intelligence*, 35:154–170, 2020.

[11] N Otsu. A threshold selection method from gray-level histograms. *IEEE Transactions on Systems, Man, and Cybernetics*, 9(1):62–66, 1979.

[12] J Yousefi. Image binarization using otsu thresholding algorithm. 2015.

[13] P Rahim, N Mustafa, H Yazid, TX Jian, S Daud, and K Rahman. Segmentation of tumour region on breast histopathology images to assess glandular formation in breast cancer grading. *Journal of Physics: Conference Series*, 2071:012051, 2021.

[14] MK Slifka and JL Whitton. Clinical implications of dysregulated cytokine production. *J. Mol. Med.*, 78:74–80, 2000.

El Cezeri
Journal of Science and Engineering
ISSN: 2148-3736

Research Article

Microwave-Assisted Pyrolysis and Co-Pyrolysis: Oil, Char, and Gases-A Technological Review

Husam Talib Hamzah[1a], Suhair Abdulhadi Mahdi[2b], Sridevi Veluru[1c] Thamer Adnan Abdullah[3d]

[1] Department of Chemical Engineering, College of Engineering, Andhra University, Visakhapatnam, India
[2] Department of Chemistry, College of Science, Mustansiriyah University, Baghdad, Iraq
[3] Applied Science Department, University of Technology, Baghdad, Iraq

alwatanaliraqi@gmail.com

DOI : 10.31202/ecjse.1386535
Received: 06.10.2023 Accepted: 13.05.2024
How to cite this article:
Husam Talib Hamzah, Suhair Abdulhadi Mahdi, Sridevi Veluru, Thamer Adnan Abdullah, " Microwave-Assisted Pyrolysis and Co-Pyrolysis: Oil, Char, and Gases-A Technological Review", El-Cezeri Journal of Science and Engineering, Vol: 11, Iss:2, (2024), pp.(186-198).
ORCID: [a]0000-0002-6827-2665; [b]0000-0003-0404-5428. [c]0000-0000-0000-0000; [d]0000-0002-9311-3316;

Abstract : Microwave-Assisted Pyrolysis and Co-Pyrolysis: Oil, Char, and Gases is an in-depth exploration of the new field of microwave-assisted pyrolysis. Microwave-assisted pyrolysis allows the extraction of oil, char, and gases from biomass, waste, and other organic components. Microwave-assisted pyrolysis has several advantages compared to conventional pyrolysis, which are discussed in detail in this paper. The article covers various aspects of microwave-assisted pyrotechnics, including fundamentals of pyrolysis, thermal decomposition processes, factors affecting pyrolysis reactions, material distribution and yield, synergistic effects, and process parameter optimization Co- pyrolysis. It also looks at production processes, where multiple raw materials are used to produce multiple value-added products simultaneously through simultaneous co-pyrolysis. This paper is helpful for academics, engineers, and professionals in biomass conversion and renewable energy since the writers explore co-pyrolysis's synergistic effects and prospective applications. With its comprehensive coverage and in-depth analysis, Microwave-Assisted Pyrolysis and Co-Pyrolysis: Oil, Char, and Gases offers a unique perspective on the application of microwave technology in pyrolysis processes. It provides readers with a thorough understanding of the basic principles, experimental methods, and potential applications of MW-assisted pyrolysis and co-pyrolysis.

Keywords : Microwave-assisted Pyrolysis, Co-pyrolysis, Synergistic Effects, Bio-oil, Char

1 Introduction

Rising standards of living combined with a growing human population have resulted in a meteoric rise in garbage output. Untreated garbage poses serious risks to ecosystems and human health if not properly managed [1]. As global energy demand and population expand, fossil fuels are increasingly exploited and progressively consumed, exacerbating the energy crisis and other major environmental challenges. Therefore, more and more people are concentrating on developing long-term strategies for using renewable energy sources [2]. The potential for more effective heating and the production of higher quality fuel and chemical products than are currently attainable using traditional pyrolysis technologies have motivated researchers to examine microwave pyrolysis in recent years. Despite the interest, the mechanisms of microwave pyrolysis are largely unreported for several reasons, including the complexity of the pyrolysis chemistry, the difficulties surrounding bio-oil analysis and quantification, a shortage of knowledge concerning the fundamentals of microwave heating, and the intensity and poorly controlled electric fields that are typical of domestic-type microwave ovens that keep going to see significant usage within scientific research. Microwave heating of biomass presents additional difficulties for precise temperature measurement, as even the most advanced laboratory equipment can only take point readings from the sample's surface rather than a complete temperature distribution [3]. Pyrolysis is the heat degradation of organic molecules that produces oil, char, and gases when oxygen is absent. The possibility of using this technique to recycle biomass, plastic, and rubber has piqued the curiosity of researchers in recent years. The advantages of microwave heating over more conventional heating methods have piqued the public's attention. Microwaves have wavelengths between 0.01 and 1 meter, corresponding to frequencies between 0.3 and 300 gigahertz (GHz) in the electromagnetic spectrum. Most home microwave ovens operate at 2.45 GHz, while 915 MHz is widely used [4]. Pyrolysis is a controlled heating process in which the feedstock is heated to high temperatures, typically (300 to 800) degrees Celsius. Since oxygen isn't present, the organic materials can be heated without catching fire. The end products have several potential uses and can be refined for further uses [5]. Multiple feedstocks can be degraded simultaneously in a co-pyrolysis process. This approach improves individual pyrolysis regarding feedstock efficiency, product yields, and quality.

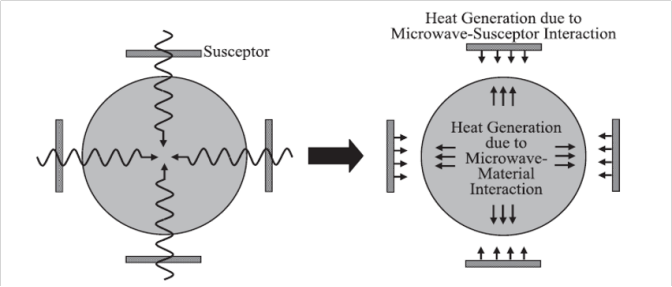

Figure 1: Two-way hybrid microwave heating with susceptors [10].

Plastic and rubber by-products and biomass are among the many organic resources that co-pyrolysis can treat [6]. It is possible to extract beneficial compounds from complex organic materials using pyrolysis and co-pyrolysis. Pyrolysis oil, sometimes called bio-oil, is a thick black liquid containing organic matter. It has many potential applications, such as fuel regeneration after processing [7]. Char, another carbon-rich product, is one of the products of pyrolysis. The high carbon content of char makes it a suitable solid fuel for heating purposes. Because of its adsorption properties, char may also purify water and air. Syngas, a by-product of pyrolysis that includes volatile organic molecules like methane, carbon dioxide, and carbon monoxide, can be utilized for heating and power generation and converted into chemicals. Conventional pyrolysis and microwave-assisted pyrolysis are different. If the former is correct, heating materials with microwaves makes the pyrolysis process go more quickly and evenly. Microwave heating is superior to older heating methods because it is more controlled, uses less energy, and is more efficient overall [5, 6]. Subjecting long-chain polymer molecules to heat and employing a catalyst makes it feasible to synthesize simpler compounds. The hydrocarbon solids (char), liquids, and gases produced during the subsequent breakdown of polymers are of fuel grade because of their petrochemical composition [8]. By utilizing microwave heating systems, pyrolysis, and co-pyrolysis processes can increase product yield, improve product quality, and decrease reaction speed. Product distribution and yield can be enhanced by microwaves controlling the pyrolysis processes. The commercialization of microwave-assisted pyrolysis technology is possible due to its rapid and effective heating capacity. This technology could completely transform pyrolysis by offering a more sustainable and economical option [5].

This review aims to equip researchers with all the necessary information regarding microwave-assisted pyrolysis and co-pyrolysis procedures for producing oil, char, and gas. The study's main objective is to find out how to employ microwave heating technology to make pyrolysis reactions more efficient and selective and then to use those products more effectively. The introduction and description of pyrolysis and co-pyrolysis are essential steps in generating renewable energy and disposing of waste. The basic concepts of pyrolysis are then covered, including how heat breaks down, what variables can influence the results of the reactions, product distribution, and yields.

2 Microwave-assisted pyrolysis Technology

The pyrolysis industry has recently extensively researched and implemented new MAP technology. Renewable energy generation is just one of several applications of microwave technology. Microwaves are electromagnetic waves with wavelengths between 1 millimeter and 1 meter (corresponding frequencies of 0.3 gigahertz GHz and 300 gigahertz GHz). The microwave is a dielectric heating method that may penetrate the biomass raw materials deeply, making it distinct from the conventional exterior heating methods of convection, conduction, and radiation. This type of heating can generate heat through molecules' strong collisions and friction. Thermogravimetric measurements using microwaves revealed that, compared to traditional Pyrolysis, MAP lowered the temperature at which biomass components began to decompose and moved the fastest weightless zone to reduce temperature intervals [9]. The microwave heat was "hybrid," meaning the susceptor helped it along. Two distinct types of heating occur during the lifetime of the susceptor, as depicted in (Fig 1). Surface heating is achieved by the susceptors, as opposed to the inside heating achieved by microwave ovens. Similarly, when compared to heating by direct microwaves, the material is heated more consistently, where the interior is often kept at a higher temperature than the exterior for a prolonged time. Reduced surface heat loss due to the presence of susceptors also aids in maintaining thermal consistency throughout the hybrid heating process [10].

Consequently, MAP has benefits, including a faster heating rate, higher energy utilization rate, quicker reaction time, and higher selectivity. Researchers in pyrolysis have increased the market value of liquid fuel, syngas, and solid carbon by using MAP technology [11, 12]. (Husam Talib Hamzah et al.) It was reported that pyrolysis was used to extract valuable materials from the tea powder. Chemical pre-treatment involved soaking the WTP and TWTP in benzene, acetone, and ethanol solvents. The FWTP was torrefied at 150 °C, resulting in a powder we call torrefied waste tea (TWTP) [5]. Researchers (Zhang et al.) found that microwave-assisted Pyrolysis (MAP) is more effective in turning low-grade lignite into bio-oil than electric heating pyrolysis [13]. Pyrolysis of bituminous coal heated in a microwave oven has been found to involve cyclization and aromatization processes. Changes in the structure of bituminous coal brought on by MAP can lead to the leakage of fluid and the subsequent release of

volatiles and moisture [14]. Improved selectivity towards phenol-rich bio-oil from microwave-assisted pyrolysis of cellulose was achieved by modifying the HZSM-5 catalyst, as reported by (Wang et al.) [15]. To selectively recycle unwanted materials, however, MAPs allow for producing phenolic compounds [16]. Vacuum distillation with membrane adsorption/fractionation (MAP) in succession is a promising method for recovering and recycling used engine oil [17]. More significant molecular weight methyl esters were abundant in the biodiesel-distilled raffinate, and a more considerable recovery rate was achieved by using MAP to extract them [18]. Combustible gas produced by biomass pyrolysis can be heated using microwave technology, which has several benefits. For MAP, high-synthesis gas was prepared with the help of a catalyst comprised of iron (III) ions supported by activated carbon. H2/CO was 1.04, and 81.14 vol% were present [19]. High-value hydrogen-rich syngas can be produced from biomass by MAP and activated carbon reforming [20]. The phenolic chemicals in industrial effluent can be removed using biochar made from MAP biomass [21]. To increase the longevity of activated carbon and make it suitable for use as a fuel adsorbent, (Lam et al.) reported combining MAP technology with chemical impregnation activation to create activated carbon with a high percentage of fixed carbon (83 wt%) and a high BET surface area (1350 m2/g) [22]. Biochar produced via microwave-catalyzed pyrolysis is more porous and has a higher cation exchange capacity than traditional pyrolysis [23].

3 By-product yield calculation

It is useful to determine the bio-oil, biochar, and biogas yields in order to assess the outcomes of a microwave pyrolysis procedure. The values of these constants are given by Equations 1, 2, 3, and 4. The yield factor is defined as the ratio of the weight of the by-products from the conversion process to the weight of the raw biomass input [24].

$$\text{Liquid yield (wt\%)} = 100 \times \frac{\text{weight of condensed liquid}}{\text{weight of raw biomass}} \tag{1}$$

$$\text{Solid yield (wt\%)} = 100 \times \frac{\text{weight of char residue}}{\text{weight of raw biomass}} \tag{2}$$

$$\text{Gas yield (wt\%)} = 100 - (\text{liquid yield} + \text{solid yield}) \tag{3}$$

$$\text{General yield (wt\%)} = 100 \times \frac{\text{biochar weight} + \text{oil} + \text{gas}}{\text{biomass weight}} \tag{4}$$

As an alternative, the yields of by-products can be calculated using Equations 5, 6, and 7. The number connects the biomass's fiber composition and the end product's functionality. Without the fiber analysis, getting an accurate range for the discrepancy between expected and experimental yields is impossible. These aspects assess how the chosen operational parameters affect final product quality [24].

$$Solidyield(wt\%) = -0.167H - 0.239C + 0.007L + 34 \tag{5}$$

$$Liquidyield(wt\%) = 0.185H - 0.076C + 0.272L + 34 \tag{6}$$

$$Gasyield(wt\%) = -0.018H + 0.315C - 0.280L + 31.9 \tag{7}$$

4 Fundamentals of Pyrolysis

In order to start the process, no oxygen should be available for pyrolysis surrounding. Organic matter can be converted into gas, char, and oil. This section covers the basics of thermal decomposition, reactions, product distribution and yield, and pyrolysis [10].

4.1 Thermal Decomposition Mechanisms

In the absence of oxygen, it is a decomposing process that reduces complex organic compounds to simple connecting parts. Knowledge of the mechanisms of thermal degradation is essential to increase product yields from pyrolysis [5]. The production of oil, char, and syngas from organic materials in efficient pyrolysis is a multistep process. This process involves pre-treatment, such as drying through heating. It is important to remove water at low temperatures before starting pyrolysis reactions [25]. During MW pyrolysis, organic matter is heated into hot particles. The high temperature of the reaction causes the chemical degradation of the product. Methane, ethane, hydrogen gas, water, and solids vapures are formed. Pyrolysis produces char as a by-product. When the temperature increases, the solid decomposes, producing char. When pyrolyzed, char is stable and contains a high percentage of fixed carbon [5].

4.1.1 Homolytic and Heterolytic Bond Cleavage

During the initial pyrolysis, the links between feedstock molecules are broken. It is possible to cleave bonds by both homolytic and heterolytic mechanisms. During the process of homolytic bond cleavage, a bond is broken into two radicals by the presence of one electron that is not paired [10]. Microwave radiation or heat is typically the initiating factor in this process. Radicals have the potential to cause bond cleavage and radical generation after they have reacted with other molecules. One way to break an unequal electron distribution is through heterolytic bond breakdown. As a consequence, a cation and an anion are produced. In the presence of catalysts or polar materials, which prevent charged species from becoming unstable, heterolytic bonds are broken more quickly [26].

4.1.2 Primary and Secondary Reactions

Radicals generated by bond breaking can undergo additional reactions. Hydrogen abstraction, beta-scission, and intramolecular rearrangements are primary reactions that immediately convert radicals or charged species into smaller molecules [10, 27]. In the hydrogen abstraction process, a new radical and a hydrogen molecule are formed when a radical combines with a hydrogen atom from another molecule. Since biomass contains a lot of hydrogen, pyrolyzing produces lots of hydrogen-rich by-products; hence, this step is especially crucial in biomass pyrolysis. Two smaller molecules are created when a bond close to the radical site is broken, known as beta-scission. In this process, unsaturated chemicals like alkenes and aromatics are formed, which can be used as chemical feedstocks or fuel precursors. Rearranging the atoms within a molecule to create new isomers or more stable molecules is an example of an intramolecular rearrangement. Because of these shifts, the distribution and yield of pyrolysis products might be substantially changed. After the primary reaction, secondary reactions occur, involving yet more modification of the intermediate products. Some examples of possible reactions are condensation, polymerization, cracking, and gasification. The reaction time, temperature, and catalysts or other reactants all have a role in secondary reactions [5, 24].

4.2 Product Distribution and Yield

Depending on the feedstock utilized, pyrolysis products are dispersed and created differently. The by-products of pyrolysis include bio-oil, char, and gases [5, 25]. A thick fluid containing several organic components, oil made by pyrolysis is called bio-oil. Feedstock and pyrolysis process settings change the characteristics of the product after pyrolysis. Bio-oil can be used as a pollution-free fuel and can be used to generate energy. Char is a by-product after pyrolysis. Although other inorganic compounds and ash exist, carbon is the most important. Char is multipurpose; it can be used as a solid fuel, but it can also enhance soil quality and neutralize contaminants in the environment [28]. Hydrogen, carbon monoxide, methane, and carbon dioxide are all components of the syngas created when microwave-assisted pyrolysis of material starts. Chemicals, liquid fuels, and energy generation can be produced from this gas. During pyrolysis, reaction time, heating rate, and temperature affect products' distribution and yield. Optimizing the pyrolysis process can enhance product yields [29]. Microwave-assisted pyrolysis requires a thorough knowledge of the principles. Prepare to apply this method to oil, char, and gas recovery by examining thermal separation, pyrolysis reaction variables, product distribution, and yield.

4.3 Factors Affecting Pyrolysis Reactions

Several factors affect pyrolysis processes and final product distribution. Temperature, heating rate, reaction time, feedstock composition, and reactor design are all important parameters to consider. When it comes to pyrolysis, heat is important. Higher temperatures produce gas, but lower temperatures are better for bio-oil and char production [10]. Furthermore, pyrolysis processes are influenced by temperature. The heat accelerates the decomposition of the material, increasing the amount of gas produced. Secondary processes can produce high yields of bio-oil and char at low temperatures. One of the important parametars is the residence time of feedstock in a pyrolysis reactor. Longer residence times allow secondary reactions, resulting in higher bio-oil and char yields. The rate of pyrolysis and the distribution of products depend on the composition of the feed. The chemical composition of the waste materials used in the process, such as plastics, rubber, or biomass, can affect the quantity and quality of the product [5, 27]. Pollutants and inorganic contaminants can impact pyrolysis. The reactor layout matters for pyrolysis. The reactor must efficiently heat and maintain feedstock temperature. The reactor design affects residence time, product distribution, and heating uniformity [10].

4.4 Influence of Feed stock Composition

The composition of the feedstock has a significant impact on the pyrolysis approach to heat breakdown. Changes in reactions and products are possible since every feedstock possesses a distinct chemical structure and functional groups. There is a difference in the thermal stability and breakdown temperatures of cellulose, hemicellulose, and lignin found in wood and agricultural waste. The pyrolysis of biomass results in the breakdown of hemicellulose and lignin at high temperatures; Bio-oil, char, and gasses are all obtained through the multistage decomposition process. However, plastic waste feedstocks include polymers like polyethylene, polypropylene, and polystyrene [30, 31]. Plastic polymer chains are broken during pyrolysis, creating smaller hydrocarbon molecules. It is also possible for pyrolysis processes and product yields to be affected by the plastic waste's

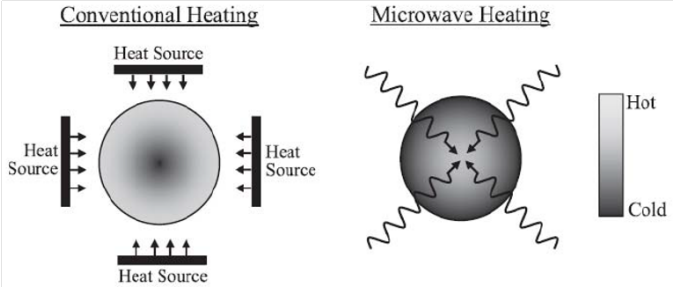

Figure 2: Conventional and Microwave-induced heating patterns [10].

composition, such as adding additives or impurities. Elastomers, found in rubber waste feedstocks like used tires and scrap rubber, have a highly intricate molecular structure. When rubber is heated to high enough temperatures, its polymer chains break down, releasing volatile gasses and leaving behind carbon black and other solid leftovers. During pyrolysis, sulfur in rubber can be converted into sulfur-rich compounds [32, 33]. Some examples of product output from microwave pyrolysis of various biomasses are shortened (Table 1).

Table 1: Microwave pyrolysis of various biomass types and product yield

Biomass	Reactor (g)	Temperature (°C)	Time (min)	Char yield (wt%)	Oil yield (wt%)	Gas yield (wt%)	Reference
Bamboo	Microwave oven	600	15	19	8	73	[34]
Pine	Microwave oven	800	15	18	4	79	[34]
Gumwood	Microwave oven	800	15	15	4	81	[34]
Rosewood	Microwave oven	700	15	22	6	72	[34]
Macroalgae	Microwave oven	750	60	28	35	37	[35]
Sugarcane bagasse	Microwave oven	550	30	62	22	16	[35]
Wood pellets	Microwave oven	800	16	22	26	52	[36]
Rubberwood	Microwave oven	550	16	21	19	60	[36]
Pinewood + lignite coal	Microwave oven	550	-	43	14	43	[37]

4.5 Residence Time

4.6 Temperature and Heating Rate Effects

Thermal degradation mechanisms during pyrolysis are susceptible to temperature and heating rate changes. In most cases, a temperature rise will cause pyrolysis reactions to proceed more quickly, resulting in increased product yields. Gasification is an example of unwanted side reactions that can occur at very high temperatures and diminish the yield of the desired products. In conventional heating, heat is transferred from an external source to an interior space using conduction and convection to transport a heating front from the surface to the interior space. The old-fashioned approach of Heating a sample always results in a higher surface temperature than an inside temperature, as seen in (Fig.2) [10].

The rate at which the temperature is increased (the heating rate) also affects the pyrolysis process. Faster reactions and shorter residence durations are two benefits of increasing the heating rate, especially in large-scale industrial pyrolysis processes. However, partial pyrolysis and the subsequent generation of char or tar residues are also possible outcomes of high heating rates [5]. The ideal temperature and heating rate are context-specific and change with the type of feedstock and the desired outcome. The optimal heating conditions, which optimize product yields while reducing undesired side reactions, can be determined by modeling and experimental research [10, 38].

4.7 Residence Time

A further factor that influences reactions is the residence of feedstock in the pyrolysis reactor. Longer residence times result in the completion of feedstock degradation, producing a greater quantity of gases and char. On the other hand, shorter residency times are more favorable for bio-oil creation. The feedstock's properties, the feedstock particles' size, and the reactor's geometry determine the residence time. Product dispersion and the efficiency of the process depend on the optimization of the residence period [10, 38].

4.8 Catalysts and Additives

Adding catalysts and additives can drastically alter the pyrolysis reactions and product yields. Cracking and reforming reactions can be boosted by catalysts, leading to more gas output and higher quality bio-oil. Pyrolysis has been modified for various uses by employing different catalysts such as zeolites, transition metals, acid catalysts, and Nano-catalysts. The pyrolysis reactions can be affected by additives like alkali metals and alkali earth metals by speeding up biomass degradation or increasing the catalytic activity. Suitable catalysts and additives must be chosen and optimized to get the targeted product yields and boost

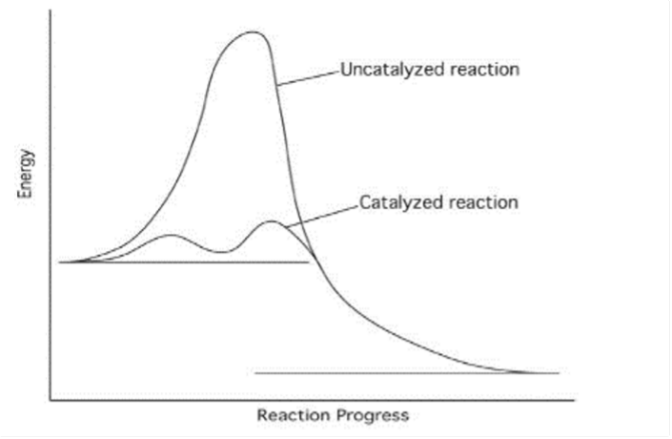

Figure 3: Conventional and Microwave-induced heating patterns.

the overall process efficiency [5]. (Figure 3) depicts catalyzed and uncatalyzed reactions, respectively. The catalytic approach has two steps, and an intermediate species is present [10]. Many catalysts function similarly, as seen in (Fig. 3), reducing the barriers for both phases relative to the uncatalyzed reaction.

4.9 Reactor Design and Configuration

The sensitivity of the pyrolysis reactions to the design and setting of the pyrolysis reactor is well-documented. The methods of heat transfer and the distribution of time of stay in a microwave reactor affect the final product's distribution. The heating uniformity and overall process efficiency can be affected by the reactor's geometry, size, and the arrangement of the heating elements. The reactor's insulation and construction can also affect heat transport and reaction kinetics. It is essential to optimize the reactor design and setup for effective heat transfer and management of the pyrolysis reactions [38, 39].

4.10 Moisture Content

The pyrolysis reactions are sensitive to the feedstock's moisture content. Since moisture is a heat sink, it takes more heat to evaporate before pyrolysis reactions occur. Due to increased moisture content, lower product yields may result from longer residence durations and less efficient heating. In addition, secondary processes such as water-gas shift reactions can be accelerated by moisture and change the chemical composition of the pyrolysis gases. Proper drying or pre-treatment of the feedstock to eliminate excess moisture is necessary to improve the pyrolysis process [10, 40, 41].

4.11 Pressure and Atmosphere

The distribution of products and their qualities are affected by the pressure and environment in which the pyrolysis events occur. Reaction kinetics and the generation of particular products can be affected by operating conditions such as atmospheric pressure, vacuum, or extreme pressures. The pyrolysis reactions can also be affected by the type of environment used (inert, reducing, or oxidizing). For instance, a reducing environment can boost syngas generation, whereas an inert atmosphere can dampen unintended reactions. Customizing the pyrolysis process for proper ends requires careful consideration of pressure and environment [28, 41, 42].

5 Co-pyrolysis Reactions

Pyrolysis of various feedstocks is called co-pyrolysis. This approach can enhance biomass and waste utilization and provide commercially viable products, including bio-oil, char, and gases. Many biomass, plastic, and rubber waste combinations can co-pyrolyze [28, 29]. Co-pyrolysis with LLDPE and HLDPE has also been the subject of substantial research. Pine pyrolysis proved to be expedited by MgCl2 and HZSM-5, while HDPE co-pyrolysis increased aromatic selectivity. Increased yields of aromatics are achieved through a reaction between furfural (made from the catalytic cracking of a pine sawdust/MgCl2 mixture) and short-chain olefins (made from the catalytic cracking of High-density polyethylene HDPE) [42]. Hydrocarbon fuel generation enhanced in waste vegetable oil and HDPE co-pyrolysis. Hydrocarbon fuels, in contrast to biodiesel, are of superior quality due to their reduced viscosity, higher heating value, and improved fluidity [43].

Co-pyrolysis of boxwood and High-density polyethylene (HDPE) synergistically produces aromatics like xylene and toluene. Increased Diels-Alder reaction between furan from biomass pyrolysis and olefins from HDPE pyrolysis accounts for the vast difference between the experimental and theoretical aromatic yields [44]. (Fig.4) shows a flow chart of this paper's subjects. The literature review provides a broad viewpoint for discussing issues and opportunities for conclusions. The findings demonstrate

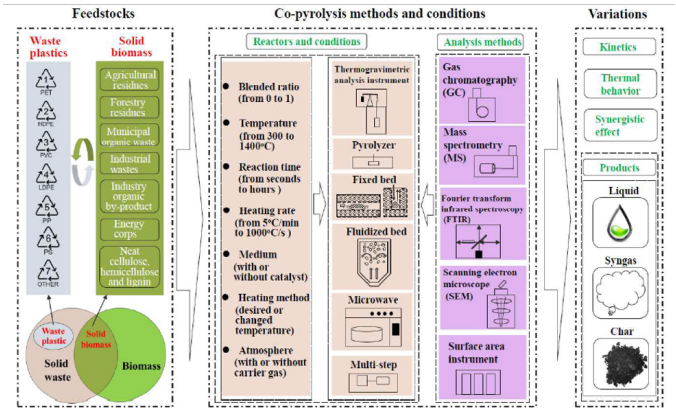

Figure 4: Diagnostic procedures for co-pyrolysis of mixed waste plastic and solid biomass are summarised in a flow diagram for laboratory studies [10].

the significance of co-pyrolysis investigation and suggest further study for sustainable and synergistic waste disposal. Co-pyrolysis has many advantages over separate pyrolysis processes for each feedstock. Synergistic effects between the various components can be realized, resulting in more productivity and better quality in the final product. Second, it allows us to get beyond the drawbacks of specific feedstocks, such as biomass's high oxygen content or plastic waste's poor energy density. The co-pyrolysis technique creates products with a more versatile composition by combining diverse feedstocks [5, 45]. Catalytic co-pyrolysis (CCP) of biomass with hydrogen-rich materials has been studied extensively, and some results are summarized in (Table 2).

Table 2: Microwave pyrolysis of various biomass types and product yield

Biomass	Co-Reactant	Catalyst	Biomass to Co-Reactant Ratio	Temp. (°C)	Reactor	Mainly Compounds	Ref.
Lignin	LDPE	MgO/HZSM-5	1:0	550	Microwave oven	Phenolic compounds	[46]
Lignin	LDPE	MgO/HZSM-5	2:1	550	Microwave oven	Phenolic compounds, aromatics	[46]
Lignin	LDPE	MgO/HZSM-5	1:1	550	Microwave oven	Aromatics, phenolic compounds	[46]
Lignin	LDPE	Zn/lignin-char	-	500	Microwave oven	Hydrocarbons, ketones, phenols	[47]
Lignin	PP	HZSM-5	1:1	200	Microwave reactor	Aromatics, alkenes, cycloalkanes	[48]
Lignin	PP	HZSM-5	1:1	250	Microwave reactor	Cycloalkanes, aromatics, alkenes	[48]
Lignin	PP	HZSM-5	1:1	300	Microwave reactor	Aromatics, cycloalkanes, alkenes	[48]
Lignin	PP	HZSM-5	1:1	350	Microwave reactor	Alkenes, aromatics, cycloalkanes	[48]
Bamboo	PP	HZSM-5	1:0	250	Microwave oven	Oxygen-cont., Aromatics, Oxygen-cont., aliphatics	[49]
Bamboo	PP	HZSM-5	2:1	250	Microwave oven	Aliphatics hydrocarbons, aromatics	[49]
Bamboo	PP	HZSM-5	1:1	250	Microwave oven	Aliphatics hydrocarbons, aromatics	[49]
Bamboo	PP	HZSM-5	1:2	250	Microwave oven	Aliphatics hydrocarbons	[49]
Bamboo	PP	HZSM-5	0:1	250	Microwave oven	Aliphatics hydrocarbons, aromatics	[49]
Rice straw	PP	HZSM-5	1:1	500	Microwave oven	Aliphatic HCs, MAHs	[50]
Bagasse	PP	HZSM-5	1:1	500	Microwave oven	Aliphatic HCs	[50]
Rice straw	PS	HZSM-5	1:1	500	Microwave oven	MAHs	[50]
Bagasse	PS	HZSM-5	1:1	500	Microwave oven	MAHs, PAHs	[50]
Cellulose	PP	HZSM-5	1:1	500	Microwave oven	BTEXs, Light olefins	[51]

In co-pyrolysis, interactions between feedstocks are complicated, resulting in additional molecules and changes in product distribution; it is possible that thermal cracking, radical reactions, or catalysts are the factors responsible for the interactions. Diversity arises because of the effect of the feed on the processes and trends. Feedstock compatibility is essential when using co-pyrolysis [26]. Chemical composition, functional groups, and preferred thermal dissociation determine the compatibility of two materials. When suppliers interact, they streamline processes. Using incompatible materials can lead to unexpected reactions or ingredient changes [27]. The heating rate, residence time, and temperature are all critical variables for co-pyrolysis processes. These variables influence reaction rate, end-product distribution, and breakdown temperature. Optimum operating conditions are necessary to obtain products and properties [24]. Product yield or quality is typically improved due to the efficiency gains offered by co-pyrolysis processes. These synergistic effects can be caused by several factors, such as the enabling effect of one feedstock on the volatility of another feedstock, the low oxygen content of compost and plastic waste, and the increased energy content of the waste [5, 33]. As the feedstock composition and processing parameters are varied, the product distribution in co-pyrolysis also changes. Bio-oil created from a combination of biomass and plastic waste, for instance, has a higher energy density and a lower oxygen content than bio-oil produced from either feedstock separately. Co-pyrolysis of biomass and rubber waste produces a bio-oil with improved stability and heating value [32, 33].

5.1 Synergistic Effects

Synergistic effects, when discussing pyrolysis and co-pyrolysis, refer to the increased output and quality of pyrolysis products that occur when two or more feedstocks are thermally decomposed simultaneously. During co-pyrolysis, multiple feedstocks, such as biomass and plastic waste, biomass, rubber waste, or biomass and yet more biomass, are pyrolyzed all at once [5]. It may be possible to establish that a synergistic effect occurs during the co-pyrolysis of plastic and biomass mixtures by comparing the indices derived from the experimental and calculated values. Calculating the theoretical value requires averaging the individual pyrolysis measurements' weighted proportional values [5, 52]. A positive synergistic impact (Y) from co-pyrolysis would be predicted if the experimental value were greater than the weighted aggregate calculated value, as shown by Equations 8 and 9 [53]:

$$Y_{\text{Calculated}} = a \times Y_{\text{feedstock 1}} + (1 - a) \times Y_{\text{feedstock 2}} \tag{8}$$

$$\Delta Y = \frac{Y_{\text{experimental}} - Y_{\text{calculated}}}{Y_{\text{calculated}}} \times 100 \tag{9}$$

5.2 Enhanced Product Yields

Co-pyrolysis has the potential for higher product yields than pyrolysis of individual feedstocks, which is a significant benefit. Synergistic effects can be achieved by combining diverse feedstocks, leading to increased conversion rates and a more even distribution of products. To illustrate, the presence of plastic trash during co-pyrolysis can operate as a heat transporter, easing the pyrolysis of biomass and increasing the overall conversion efficiency [54]; as a result of this combination, oil production increases while char formation decreases. Similarly, the catalytic impact of rubber on biomass pyrolysis can boost oil output when the two are co-pyrolyzed. Oil extraction and biomass thermal cracking are both enhanced by rubber by-products. Biomass and rubber waste interactions can change the bio-oil's composition and quality, which increases its versatility [55].

5.3 Improved Product Quality

The use of co-pyrolysis improves the quality of the pyrolysis product. The synergistic effects of feedstock chemical composition can alter the specific properties of oil, char, and gas. One example is the production of bio-oil with high heating value and stability by co-pyrolysis of biomass and plastic wastes. Hydrogen supplied from plastic waste can increase the energy content of biooil, reducing its oxygen content [5]. The co-treatment of biomass and rubber waste can improve the bio-oil quality. Bio-oil with improved fuel characteristics can be produced using new and modified biomass and waste rubber chemicals. Rubber degradation reduces the oxygen content of the oil and facilitates the production and use of bio-oil [32, 33].

5.4 Synergistic Catalytic Effects

In co-pyrolysis, when another enhances one feed catalyst, there is a synergistic catalytic effect. The method influences the distribution and composition of the co-pyrolysis products. Chars can work as catalysts and susceptors, produced by pyrolyzing biomass and plastic waste, accelerating secondary reactions, and enhancing methane and hydrogen production. Catalytic chars enhance gas production by decomposing products and breaking them down. The combination of biomass and rubber waste is more effective in co-pyrolysis. By degrading solid biomass components, rubber waste can accelerate biomass pyrolysis and gas production. Catalysts can be formed during the interaction of biomass with rubber waste, which can enhance catalyst activity and dispersion [56].

5.5 Environmental Benefits

Co-pyrolysis is more environmentally friendly than feedstock pyrolysis. Co-incineration of biomass, plastic, and rubber waste can reduce environmental impact and help manage waste. Multi-feedstock co-pyrolysis improves resource efficiency and reduces emissions. Co-pyrolysis produces hydrogen and methane, which can further a sustainable energy system. Industrial activities that use these gasses instead of fossil fuels can lower our carbon footprint and climate impact [57].

5.6 Product Distribution in Co-pyrolysis

The term "co-pyrolysis" describes the practice of pyrolyzing multiple feedstocks at once. Collaborative pyrolysis provides synergistic advantages and new product distributions by thermally degrading several feedstocks [58]. The feedingstock's composition, the pyrolysis process's parameters, and the feedstock's interaction determine the product distribution in co-pyrolysis. Interactions with feedstock can take a cooperative or competitive aspect. Reduced feedstock pyrolysis is a competitive outcome [59]. There may be a decrease in product output as a result. Because biomass particles compete with plastic particles for chemical adhesion, the liquid product yield in biomass-plastic co-pyrolysis may be lower. Chemicals generated from rubber that compete with one another for the surface adsorption of biomass particles in biomass Bio-oil formation are hindered by

rubber co-pyrolysis [60]. Cooperative effects are created when another enhances the pyrolysis of one feedstock. Potentially, this might result in higher product yields. Biomass-plastic co-pyrolysis enhances biomass thermal cracking and increases gaseous product production. Gaseous products are enhanced through improved rubber thermal cracking in biomass-rubber co-pyrolysis. The products' distribution depends on the co-pyrolysis conditions, including temperature, heating rate, and residence time. Optimizing product yields is achieved by modifying these components. Increasing the pyrolysis temperature can enhance the gaseous product output and feedstock thermal cracking. Char, however, can be produced by extremely hot substances [61]. Product distribution in co-pyrolysis is susceptible to feedstock characteristics and composition. The molecular structure and heat stability are two elements that influence how feedstock pyrolysis behaves. Biomass contains abundant cellulose, hemicellulose, and lignin, which, when hydrolyzed, can yield several compounds. Essential plastic components decompose during polymer heating, releasing a cloud of hydrocarbon fumes [5]. New chemicals and products are created when feedstocks interact in co-pyrolysis. A higher-grade bio-oil can be obtained by co-pyrolyzing biomass with plastic, provided that certain aromatic compounds are generated. Compounds of interest are produced by heating rubber and biomass. These molecules can then be transformed into valuable compounds [30, 33]. It is possible to examine the dispersion of co-pyrolysis by-products using GC-MS, FTIR, and NMR. These methods are employed to identify and measure the many products that emerge during co-pyrolysis [5, 61].

6 Advantages and Challenges of Co-pyrolysis

There are a lot of advantages to co-pyrolysis with various feedstocks over single-feedstock pyrolysis. The effect of co-pyrolysis will be discussed here.

6.1 Synergistic Effects

Interactions between pyrolysis components hasten the thermal breakdown and boost the production of valuable by-products, including bio-oil, char, and gases. Through the co-pyrolysis of feedstocks, this interaction can lead to synergistic advantages [5, 59, 61].

6.2 Product Diversification

Compared to pyrolysis using just one feedstock, co-pyrolysis enables the creation of a broader range of products. Combining feedstocks with diverse qualities can change the distribution of a product and increase its value. Many industries and products can benefit from the bio-oil and syngas that are by-products of co-pyrolysis of biomass and waste plastic [41, 62, 63].

6.3 Improved Bio-oil Quality

In conjunction with other feedstocks like plastics or rubber, bio-oil made from biomass is the way to enhance the pyrolysis process of bio-oil; one can incorporate hydrogen by reusing plastics or rubber. Decreasing bio-oil oxygen levels and boosting energy density improves thermal efficiency, adaptability, and reliability [24, 33, 64].

6.4 Waste Valorization

Through co-pyrolysis, it is possible to generate value from hard-to-recycle/unwanted waste. Acquiring the bio-oil, char, and gases from waste and biomass is feasible. In addition to reducing negative environmental impacts, this method can also generate profit from waste [5, 63].

6.5 Process Intensification

Using co-pyrolysis to enhance pyrolysis also shortens the reaction time. Meanwhile, many feedstocks can speed up thermal decomposition, improving conversion efficiency. In contrast to single-feedstock pyrolysis, this method can increase output while decreasing energy use [65, 63, 66].

6.6 Feedstock Compatibility

One of the most challenging issues for co-pyrolysis is to find feedstocks that work well together and are efficient for feedstock pyrolysis, including thermal decomposition temperature and reaction kinetics. Experiments must be conducted and the process optimized to determine which feedstock combinations produce valuable products with a synergistic effect [67].

6.7 Product Distribution Control

Co-pyrolysis can make it harder to control the product yield because of the complicated variety of products. Depending on the feedstock used, pyrolysis pathways and product selectivity can change. Understanding the mechanisms of pyrolysis is necessary so we can adjust the parameters of the process to get products appropriately distributed [68].

6.8 Process Optimization

Feedstock ratios, heating rates, reaction temperatures, and reaction times are some factors that must be optimized in the co-pyrolysis processes. Extensive experimental testing and analysis may be necessary during the optimization process, which can be time- and resource-intensive. Additionally, the ideal conditions for co-pyrolysis may differ from those performed on a single feedstock pyrolysis, adding complexity to the process development [69, 70].

6.9 Scale-up Challenges

The transition from the laboratory scale to the industrial scale of co-pyrolysis systems can be difficult. The compatibility of different feedstocks, process dynamics, and heat transport properties may vary at different scales. During the scaling-up process, important considerations include ensuring the product quality is constant, keeping the process stable, and addressing concerns regarding safety or the environment; because the microwave-assisted pyrolysis reactor with microwave absorbent bed is capable of working continuously and effectively for pyrolysis processes, it has the potential to be scaled up to a larger reactor [71, 72].

7 Conclusion

Bio-oil produced by microwave-assisted pyrolysis shows promise as a marketable result. Bio-oil's oxygen concentration can be lowered through catalytic upgrading, making it a more stable and profitable product. Sustainability, adaptability, and the opportunity to create new products are just a few benefits of using bio-oil. However, issues with its complicated composition and high oxygen content must be resolved to realize bio-oil promise entirely. Synergistic effects, product diversity, enhanced bio-oil quality, waste valorization, and process intensification are just a few of the benefits of co-pyrolysis compared to pyrolysis of a single feedstock. In order to successfully implement co-pyrolysis technologies, it is necessary to address issues such as feedstock compatibility, product distribution management, process optimization, scaling up, and environmental consequences. Co-pyrolysis plays a role in waste management and generates bio-oil, char, and gases, which allows it to overcome these limits and realize its full potential for the recovery of resources and the generation of sustainable energy. Utilizing bio-oil derived from co-pyrolysis can serve as a chemical feedstock and sustainable fuel. Char, being similar to coal, can be burned. Optimize co-pyrolysis and find novel bio-oil and char uses. Syngas production by co-pyrolysis is fascinating.

Hydrogen-rich gases are used in energy generation, chemical and fuel production, and more. Environmental benefits make co-pyrolysis a feasible waste management approach. Feedstock heterogeneity and syngas impurities must be addressed to optimize the process and ensure syngas quality. These impediments must be addressed to maximize co-pyrolysis for syngas production, necessitating more research. Advances in microwave-assisted and co-pyrolysis offer new ways to recycle biomass, plastic, and rubber. Reactor design, catalysts, hybrid processes, process optimization, integration with renewable energy sources, and feedstock conversion improve pyrolysis systems' efficiency, scalability, and environmental impact. These developments benefit pyrolysis's long-term viability and contribute to building a greener, more closed-loop economy. For their many benefits in efficiency, adaptability, and the generation of high-value end products, microwave-assisted pyrolysis and co-pyrolysis technologies are poised for rapid commercialization. Market conditions favor these technologies because eco-friendly waste management options and renewable replacements for traditional fuels are needed. Successful commercialization, however, requires solving problems of scale-up, feedstock variability, and economic viability. MW-assisted pyrolysis and co-pyrolysis can improve sustainability and the circular economy with additional study, development, and teamwork. The product distribution and yield in MW-assisted pyrolysis and co-pyrolysis processes are affected by factors such as feedstock composition, heating rate, temperature, residence duration, and reactor design. Optimizing these factors allows maximizing the intended product outputs and boosting the technology's overall efficiency. Improvements in product distribution and yield can be made by more research and development into the complex interplay between these factors in MW-assisted Pyrolysis and co-pyrolysis.

Competing Interests

The authors declare that they have no competing interests.

References

[1] G. Su, H. C. Ong, I. M. R. Fattah, Y. S. Ok, J. Jang, and C. Wang. State-of-the-art of the pyrolysis and co-pyrolysis of food waste: Progress and challenges. *Science of The Total Environment*, 809:151170, 2022.

[2] J. Liu, Q. Hou, M. Ju, P. Ji, Q. Sun, and W. Li. Biomass pyrolysis technology by catalytic fast pyrolysis, catalytic co-pyrolysis and microwave-assisted pyrolysis: A review. *Catalysts*, 10(7):742, 2020.

[3] J. Robinson, E. Binner, D. B. Vallejo, N. D. Perez, K. Al Mughairi, J. Ryan, B. Shepherd, M. Adam, V. Budarin, J. Fan, M. Gronnow, and F. Peneranda-Foix. Unravelling the mechanisms of microwave pyrolysis of biomass. *Chemical Engineering Journal*, 430:132975, 2022.

[4] J. E. Omoriyekomwan, A. Tahmasebi, J. Dou, R. Wang, and J. Yu. A review on the recent advances in the production of carbon nanotubes and carbon nanofibers via microwave-assisted pyrolysis of biomass. *Fuel Processing Technology*, 214: 106686, 2021.

[5] H. Talib Hamzah, V. Sridevi, M. Seereddi, D. V. Suriapparao, P. Ramesh, C. Sankar Rao, R. Gautam, F. Kaka, and K. Pritam. The role of solvent soaking and pre-treatment temperature in microwave-assisted pyrolysis of waste tea powder: Analysis of products, synergy, pyrolysis index, and reaction mechanism. *Bioresource Technology*, 363:127913, 2022.
[6] H. T. Hamzah, V. Sridevi, and D. V. Surya. Conventional and microwave-assisted acid pre-treatment of tea waste powder: analysis of functional groups using ftir. *Environmental Science and Pollution Research*, 2023.
[7] Z. Wang, K. G. Burra, T. Lei, and A. K. Gupta. Co-pyrolysis of waste plastic and solid biomass for synergistic production of biofuels and chemicals-a review. *Progress in Energy and Combustion Science*, 84:100899, 2021.
[8] A. Pattiya. Catalytic pyrolysis. In *Direct Thermochemical Liquefaction for Energy Applications*, pages 29–64. 2018.
[9] H. Luo, W. Bao, Z. Kong, and H. Sun. Revealing low temperature microwave-assisted pyrolysis kinetic behaviors and dielectric properties of biomass components. *AIChE Journal*, 64(6):2124–2134, 2018.
[10] H. Talib Hamzah, V. Sridevi, H. Mohammed Hasan, H. Yousif Abed, H. Salah Mahdi, N. Abdulqader Hamdullah, M. Tukarambai, V. Rao Poiba, and R. Srikanth. Microwave assisted pyrolysis of biomass feedstock fundamentals and the effect of process parameters - a review. *Journal of Physics: Conference Series*, 2550:012003, 2023.
[11] E. Villota, M. Qian, Z. Yang, E. Villota, Y. Zhang, and G. Yadavalli. Optimizing microwave-assisted pyrolysis of phosphoric acid-activated biomass: impact of concentration on heating rate and carbonization time. *ACS Sustainable Chemistry and Engineering*, 6(1):1318–1326, 2017.
[12] A. M. Parvez, T. Wu, M. T. Afzal, S. Mareta, T. He, and M. Zhai. Conventional and microwave-assisted pyrolysis of gumwood: A comparison study using thermodynamic evaluation and hydrogen production. *Fuel Processing Technology*, 184:1–11, 2019.
[13] Y. Zhang, S. Liu, L. Fan, N. Zhou, M. M. Omar, P. Peng, E. Anderson, M. Addy, Y. Cheng, and Y. Liu. Oil production from microwave-assisted pyrolysis of a low rank american brown coal. *Energy Conversion and Management*, 159:76–84, 2018.
[14] H. Li, S. Shi, B. Lin, J. Lu, Q. Ye, Y. Lu, Z. Wang, Y. Hong, and X. Zhu. Effects of microwave-assisted pyrolysis on the microstructure of bituminous coals. *Energy*, 187, 2019.
[15] W. Wang, M. Wang, J. Huang, N. Tang, Z. Dang, Y. Shi, and M. Zhaohe. Microwave-assisted catalytic pyrolysis of cellulose for phenol-rich bio-oil production. *Journal of the Energy Institute*, 92:1997–2003, 2019.
[16] D. V. Suriapparao, S. Batchu, S. Jayasurya, and R. Vinu. Selective production of phenolics from waste printed circuit boards via microwave assisted pyrolysis. *Journal of Cleaner Production*, 197:525–533, 2018.
[17] X. Li, J. Zhai, H. Li, and X. Gao. An integration recycling process for cascade utilization of waste engine oil by distillation and microwave-assisted pyrolysis. *Fuel Processing Technology*, 199, 2020.
[18] E. Anderson, J. Zhou, L. Fan, S. Liu, N. Zhou, P. Peng, Y. Cheng, P. Chen, and R. Ruan. Microwave-assisted pyrolysis as an alternative to vacuum distillation for methyl ester recovery from biodiesel vacuum distillation bottoms. *ACS Sustainable Chemistry and Engineering*, 6:14348–14355, 2018.
[19] Q. Dong, M. Niu, D. Bi, W. Liu, X. Gu, and C. Lu. Microwave-assisted catalytic pyrolysis of moso bamboo for high syngas production. *Bioresource Technology*, 256:145–151, 2018.
[20] K. Shi, J. Yan, J. Angel Menendez, X. Luo, G. Yang, Y. Chen, E. Lester, and T. Wu. Production of h-2-rich syngas from lignocellulosic biomass using microwave-assisted pyrolysis coupled with activated carbon enabled reforming. *Frontiers in Chemistry*, 8, 2020.
[21] G.S. Dos Reis, M.A. Adebayo, C.H. Sampaio, E.C. Lima, P.S. Thue, I.A.S. de Brum, S.L.P. Dias, and F.A. Pavan. Removal of phenolic compounds from aqueous solutions using sludge-based activated carbons prepared by conventional heating and microwave-assisted pyrolysis. *Water Air Soil Pollution*, 228, 2017.
[22] S.S. Lam, R.K. Liew, Y.M. Wong, P.N.Y. Yek, N.L. Ma, C.L. Lee, and H.A. Chase. Microwave-assisted pyrolysis with chemical activation, an innovative method to convert orange peel into activated carbon with improved properties as dye adsorbent. *Journal of Cleaner Production*, 162:1376–1387, 2017.
[23] B.A. Mohamed, N. Ellis, C.S. Kim, X. Bi, and A.E.-R. Emam. Engineered biochar from microwave-assisted catalytic pyrolysis of switchgrass for increasing water-holding capacity and fertility of sandy soil. *Science of The Total Environment*, 566:387–397, 2016.
[24] S. Allende, G. Brodie, and M.V. Jacob. Breakdown of biomass for energy applications using microwave pyrolysis: A technological review. *Environmental Research*, 226:115619, 2023.
[25] M. Ahmed and B. Hameed. Insight into the co-pyrolysis of different blended feedstocks to biochar for the adsorption of organic and inorganic pollutants: A review. *Journal of Cleaner Production*, 265:121762, 2020.
[26] D. Phakedi, A.U. Ude, and P.O. Oladijo. Co-pyrolysis of polymer waste and carbon-based matter as an alternative for waste management in the developing world. *Journal of Analytical and Applied Pyrolysis*, 155:105077, 2021.
[27] Y. Li, H. Zhao, X. Sui, X. Wang, and H. Ji. Studies on individual pyrolysis and co-pyrolysis of peat–biomass blends: Thermal decomposition behavior, possible synergism, product characteristic evaluations and kinetics. *Fuel*, 310:122280, 2022.

[28] X. Jin, J.H. Lee, and J.W. Choi. Catalytic co-pyrolysis of woody biomass with waste plastics: Effects of hzsm-5 and pyrolysis temperature on producing high-value pyrolytic products and reducing wax formation. *Energy*, 239:121739, 2022.

[29] W.A. Wan Mahari, E. Azwar, S.Y. Foong, A. Ahmed, W. Peng, M. Tabatabaei, M. Aghbashlo, Y. Park, C. Sonne, and S.S. Lam. Valorization of municipal wastes using co-pyrolysis for green energy production, energy security, and environmental sustainability: A review. *Chemical Engineering Journal*, 421:129749, 2021.

[30] P.H.M. Putra, S. Rozali, M.F.A. Patah, and A. Idris. A review of microwave pyrolysis as a sustainable plastic waste management technique. *Journal of Environmental Management*, 303:114240, 2022.

[31] N. Zhou, L. Dai, Y. Lv, H. Li, W. Deng, F. Guo, P. Chen, H. Lei, and R. Ruan. Catalytic pyrolysis of plastic wastes in a continuous microwave assisted pyrolysis system for fuel production. *Chemical Engineering Journal*, 418:129412, 2021.

[32] Y. Pan, X. Du, C. Zhu, J. Wang, J. Xu, Y. Zhou, and Q. Huang. Degradation of rubber waste into hydrogen enriched syngas via microwave-induced catalytic pyrolysis. *International Journal of Hydrogen Energy*, 47(80):33966–33978, 2022.

[33] Z. Song, Y. Hu, Y. Han, S. Chen, X. Zhao, J. Sun, Y. Mao, X. Wang, and W. Wang. Effect of swelling pre-treatment by coal tar on the microwave pyrolysis of waste tires. *Journal of Environmental Chemical Engineering*, 11(5):110781, 2023.

[34] K. Shi, J. Yan, J.A. Menéndez, X. Luo, G. Yang, Y. Chen, E. Lester, and T. Wu. Production of h2-rich syngas from lignocellulosic biomass using microwave-assisted pyrolysis coupled with activated carbon enabled reforming. *Frontiers in Chemistry*, 8:511935, 2020.

[35] N. Ferrera-Lorenzo, E. Fuente, J. Bermúdez, I. Suárez-Ruiz, and B. Ruiz. Conventional and microwave pyrolysis of a macroalgae waste from the agar–agar industry. prospects for bio-fuel production. *Bioresource Technology*, 151:199–206, 2013.

[36] S.A. Halim and J. Swithenbank. Characterisation of malaysian wood pellets and rubberwood using slow pyrolysis and microwave technology. *Journal of Analytical and Applied Pyrolysis*, 122:64–75, 2016.

[37] V. Abdelsayed, C. Ellison, A. Trubetskaya, M.W. Smith, and D. Shekhawat. Effect of microwave and thermal co-pyrolysis of low-rank coal and pine wood on product distributions and char structure. *Energy & Fuels*, 33(8):7069–7082, 2019.

[38] S. Mutsengerere, C. Chihobo, D. Musademba, and I. Nhapi. A review of operating parameters affecting bio-oil yield in microwave pyrolysis of lignocellulosic biomass. *Renewable and Sustainable Energy Reviews*, 104:328–336, 2019.

[39] S. Wu, Y. Song, X. Wang, J. Xu, B. Xiao, and K. Qiao. Simulation and optimization of heating rate and thermal uniformity of microwave reactor for biomass pyrolysis. *Chemical Engineering Science*, 250:117386, 2022.

[40] H.T. Hamzah, N.M. Alawi, H.M. Hasan, H.Y. Abed, S. Veluru, N.A. Hamdullah, A.A. Ibrahim, M. Tukarambai, V.R. Poiba, and R. Srikanth. Effect of acids and alkaline pre-treatment of used tea waste powder under microwave-assisted pre-treatment. *Key Engineering Materials*, 960:149–160, 2023.

[41] D.V. Suriapparao, R. Gautam, and L. Rao Jeeru. Analysis of pyrolysis index and reaction mechanism in microwave-assisted ex-situ catalytic co-pyrolysis of agro-residual and plastic wastes. *Bioresource Technology*, 357:127357, 2022.

[42] H. Hassan, J.K. Lim, and B.H. Hameed. Catalytic co-pyrolysis of sugarcane bagasse and waste high-density polyethylene over faujasite-type zeolite. *Bioresource Technology*, 284:406–414, 2019.

[43] C.A. Mullen, C. Dorado, and A.A. Boateng. Catalytic co-pyrolysis of switchgrass and polyethylene over hzsm-5: Catalyst deactivation and coke formation. *Journal of Analytical and Applied Pyrolysis*, 129:195–203, 2018.

[44] D. Duan, Y. Wang, L. Dai, R. Ruan, Y. Zhao, L. Fan, M. Tayier, and Y. Liu. Ex-situ catalytic co-pyrolysis of lignin and polypropylene to upgrade bio-oil quality by microwave heating. *Bioresource Technology*, 241:207–213, 2017.

[45] M. Bartoli, M. Frediani, C. Briens, F. Berruti, and L. Rosi. An overview of temperature issues in microwave-assisted pyrolysis. *Processes*, 7(10):658, 2019.

[46] L. Fan, P. Chen, Y. Zhang, S. Liu, Y. Liu, Y. Wang, L. Dai, and R. Ruan. Fast microwave-assisted catalytic co-pyrolysis of lignin and low-density polyethylene with hzsm-5 and mgo for improved bio-oil yield and quality. *Bioresource Technology*, 225:199–205, 2017.

[47] O. Sanahuja-Parejo, A. Veses, J.M. Lopez, R. Murillo, M. Soledad Callen, and T. Garcia. Ca-based catalysts for the production of high-quality bio-oils from the catalytic co-pyrolysis of grape seeds and waste tyres. *Catalysts*, 19:992, 2019.

[48] M.U. Garba, A. Inalegwu, U. Musa, A.A. Aboje, A.S. Kovo, and D.O. Adeniyi. Thermogravimetric characteristic and kinetic of catalytic co-pyrolysis of biomass with low- and high-density polyethylenes. *Biomass Conversion and Biorefinery*, 8:143–150, 2018.

[49] X. Xue, Z. Pan, C. Zhang, D. Wang, Y. Xie, and R. Zhang. Segmented catalytic co-pyrolysis of biomass and high-density polyethylene for aromatics production with mgcl2 and hzsm-5. *Journal of Analytical and Applied Pyrolysis*, 134:209–217, 2018.

[50] Y.-M. Kim, J. Jae, B.-S. Kim, Y. Hong, S.-C. Jung, and Y.-K. Park. Catalytic co-pyrolysis of torrefied yellow poplar and high-density polyethylene using microporous hzsm-5 and mesoporous al-mcm-41 catalysts. *Energy Conversion and Management*, 149:966–973, 2017.

[51] P. Chang Qi, G. Wang, H. Zhang, X. Guo, and Q. Production of aromatic hydrocarbons by catalytic co-pyrolysis of microalgae and polypropylene using hzsm-5. *Journal of Analytical and Applied Pyrolysis*, 136:178–185, 2018.
[52] B.L.F. Chin, S. Yusup, A. Al Shoaibi, P. Kannan, C. Srinivasakannan, and S.A. Sulaiman. Kinetic studies of co-pyrolysis of rubber seed shell with high density polyethylene. *Energy Conversion and Management*, 87:746–753, 2014.
[53] W. Chen, S. Shi, J. Zhang, M. Chen, and X. Zhou. Co-pyrolysis of waste newspaper with high-density polyethylene: Synergistic effect and oil characterization. *Energy Conversion and Management*, 112:41–48, 2016.
[54] A.E.F. Abomohra, H.M. Sheikh, A.H. El-Naggar, and Q. Wang. Microwave vacuum co-pyrolysis of waste plastic and seaweeds for enhanced crude bio-oil recovery: Experimental and feasibility study towards industrialization. *Renewable and Sustainable Energy Reviews*, 149:111335, 2021.
[55] R. Potnuri, C.S. Rao, D.V. Surya, A. Kumar, and T. Basak. Utilizing support vector regression modeling to predict pyro product yields from microwave-assisted catalytic co-pyrolysis of biomass and waste plastics. *Energy Conversion and Management*, 292:117387, 2023.
[56] M.H. Ahmed, N. Batalha, H.M. Mahmudul, G. Perkins, and M. Konarova. A review on advanced catalytic co-pyrolysis of biomass and hydrogen-rich feedstock: Insights into synergistic effect, catalyst development and reaction mechanism. *Bioresource Technology*, 310:123457, 2020.
[57] W.A. Wan Mahari, S. Awang, N.A.Z. Zahariman, W. Peng, M. Man, Y. Park, J. Lee, C. Sonne, and S.S. Lam. Microwave co-pyrolysis for simultaneous disposal of environmentally hazardous hospital plastic waste, lignocellulosic, and triglyceride biowaste. *Journal of Hazardous Materials*, 423:127096, 2022.
[58] C. Chen, J. Zhao, D. Fan, Q. Qi, T. Zeng, and Y. Bi. Microwave-assisted co-pyrolysis of chlorella vulgaris and polypropylene: Characteristic and product distribution analyses. *Bioresource Technology*, 344:126279, 2021.
[59] S. Gu, Z. Xu, Y. Ren, Y. Tu, D. Lu, and H. Wang. Microwave co-pyrolysis of lignite with direct coal liquefaction residue: Synergistic effects and product combustion characteristics. *Journal of Cleaner Production*, 325:129293, 2021.
[60] H. Yu, J. Qu, Y. Liu, H. Yun, X. Li, C. Zhou, Y. Jin, C. Zhang, J. Dai, and X. Bi. Co-pyrolysis of biomass and polyvinyl chloride under microwave irradiation: Distribution of chlorine. *Science of The Total Environment*, 806:150903, 2022.
[61] Z. Zhao, S.M.A. Abdo, X. Wang, H. Li, X. Li, and X. Gao. Process intensification on co-pyrolysis of polyethylene terephthalate wastes and biomass via microwave energy: Synergetic effect and roles of microwave susceptor. *Journal of Analytical and Applied Pyrolysis*, 158:105239, 2021.
[62] G. Su, H.C. Ong, M.Y. Cheah, W. Chen, S.S. Lam, and Y. Huang. Microwave-assisted pyrolysis technology for bioenergy recovery: Mechanism, performance, and prospect. *Fuel*, 326:124983, 2022.
[63] H.T. Hamzah, V. Sridevi, D.V. Surya, P. Ramesh, C.S. Rao, S. Palla, and T.A. Abdullah. Synergistic effects and product yields in microwave-assisted in-situ co-pyrolysis of rice straw and paraffin wax. *Process Safety and Environmental Protection*, 182:45–55, 2024.
[64] Q. Wu, Y. Wang, L. Jiang, Q. Yang, L. Ke, Y. Peng, S. Yang, L. Dai, Y. Liu, and R. Ruan. Microwave-assisted catalytic upgrading of co-pyrolysis vapor using hzsm-5 and mcm-41 for bio-oil production: Co-feeding of soapstock and straw in a downdraft reactor. *Bioresource Technology*, 299:122611, 2020.
[65] Y. Zhang, S. Fan, T. Liu, M.M. Omar, and B. Li. Perspectives into intensification for aviation oil production from microwave pyrolysis of organic wastes. *Chemical Engineering and Processing - Process Intensification*, 176:108939, 2022.
[66] I. Muhammad and G. Manos. Intensification of co-pyrolysis of plastic with biomass via pre-treatment. *Process Safety and Environmental Protection*, 146:586–598, 2021.
[67] X. Ren, M. Shanb Ghazani, H. Zhu, W. Ao, H. Zhang, E. Moreside, J. Zhu, P. Yang, N. Zhong, and X. Bi. Challenges and opportunities in microwave-assisted catalytic pyrolysis of biomass: A review. *Applied Energy*, 315:118970, 2022.
[68] Y. Zeng, Y. Wang, Y. Liu, L. Dai, Q. Wu, M. Xia, S. Zhang, L. Ke, R. Zou, and R. Ruan. Microwave catalytic co-pyrolysis of waste cooking oil and low-density polyethylene to produce monocyclic aromatic hydrocarbons: Effect of different catalysts and pyrolysis parameters. *Science of The Total Environment*, 809:152182, 2022.
[69] S. Neha and N. Remya. Optimization of bio-oil production from microwave co-pyrolysis of food waste and low-density polyethylene with response surface methodology. *Journal of Environmental Management*, 297:113345, 2021.
[70] B. Wang, N. Liu, S. Wang, X. Li, R. Li, and Y. Wu. Study on co-pyrolysis of coal and biomass and process simulation optimization. *Sustainability*, 15(21):15412, 2022.
[71] M. Singh, S.A. Salaudeen, and B.H. Gilroyed. A review on co-pyrolysis of biomass with plastics and tires: Recent progress, catalyst development, and scaling up potential. *Biomass Conversion and Biorefinery*, 13:8747–8771, 2023.
[72] Y. Duan, P. Yuan, S. Huang, L. Wang, J. Deng, S. Yu, Q. Xie, and Y. Nie. Experimental study on reactor scale-up for microwave-assisted pyrolysis of methyl ricinoleate. *Chemical Engineering and Processing - Process Intensification*, 184: 109293, 2023.

El Cezeri
Journal of Science and Engineering
ISSN: 2148-3736

Research Article

Optimization of Electro-Blown PVDF Nanofibrous Mats for Air Filter Applications

Ali Toptaş[1,2a], Mehmet Durmuş Çalışır[1,3b], Ali Kılıç[1,4c]
[1] TEMAG Labs, Faculty of Textile Tech and Design, Istanbul Technical University, Istanbul, Türkiye
[2] Safranbolu Vocational School, Karabuk University, Karabuk, Türkiye
[3] Faculty of Engineering and Architecture, Recep Tayyip Erdogan University, Rize, Türkiye
[4] Areka Group LLC, Istanbul, Türkiye

aalikilic@itu.edu.tr

DOI : 10.31202/ecjse.1391754
Received: 16.10.2023 Accepted: 12.02.2024
How to cite this article:
Ali Toptaş, Mehmet Durmuş Çalışır, Ali Kılıç, " Optimization of Electro-Blown PVDF Nanofibrous Mats for Air Filter Applications", El-Cezeri Journal of Science and Engineering, Vol: 11, Iss:2, (2024), pp.(199-206).
ORCID: [a]0000-0002-1176-0844; [b]0000-0002-5916-9666. [c]0000-0001-5915-8732;

Abstract : Particles with diameters smaller than 2.5 µm (PM2.5) have the capability to penetrate into respiratory system, thereby exerting adverse effects on human health. High-efficiency nanofiber mats present a viable and efficient solution for the purification of ambient air contaminated with such particulate matter. In this study, PVDF based electret nanofiber mats were optimized via electro-blowing technique. The experimental parameters were systematically devised utilizing a Taguchi three-level L9 orthogonal design, and the results were subsequently analyzed using ANOVA. In this context, among the examined parameters (solution concentration, air pressure, and electrical field), the most significant factors influencing fiber diameters were identified as solution concentration and electric field strength. While an increase in air pressure exhibited a negligible influence on fiber diameters, it was observed to mitigate undesired droplet density. The optimal parameters yielding the thinnest fiber (124 ± 71 nm) were determined as 9 wt.% solution concentration, 2 bar air pressure, and 30 kV electrical voltage. Furthermore, the application of corona discharge treatment to the specimens resulted in a remarkable enhancement of quality factors by over 70%.

Keywords : Nanofiber, Electro-Blowing Technique, Corona Discharge, Air filter

1 Introduction

In today's world, air pollution has reached critical levels due to the increasing number of fires, rapidly growing population, and industrial activities [1]. Air pollutants are classified based on their physical states as particulate matter and gaseous pollutants, while microorganisms like viruses and bacteria, metal ions, and fine/coarse particles constitute particulate matter and are further classified according to particle size [2]. Air filtration is an effective method to mitigate the problems arising from air pollution and provide clean and healthy air [3]. For this purpose, various types of air filters such as paper, membranes, woven or non-woven fabrics, etc., have been developed [4]. The primary goal in development efforts is to produce filters with high particle capture efficiency at an expense of low pressure drop (ΔP). Existing commercial high-efficiency particulate air filters (HEPA) have a filtration efficiency of at least 99.97% for aerosols and particles of $0.3\mu m$ and above [5, 6]. These filters are made from meltblown or glass fibers and there is a need for filters with fiber diameters in the range of 50nm to$1\mu m$ to effectively filter finer aerosols [6]. Filters with low pore size and high porosity layers can be produced using nanofibers with a high surface area-to-volume ratio [7]. However, this can lead to high ΔP in the filter media.

Electrospinning is one of the most common methods to produce nanofibers [8, 9, 10, 11, 12]. This method, where the driving force is an electrostatic field, enables the production of fine fibers with minimal defects (beads, droplets, etc.). However, it has the disadvantage of low solution feed rate and production rate [13]. Recently, the solution blowing method has been developed as an alternative, in which fibers are produced by the aerodynamic forces created by pressurized air acting on a polymer solution [14]. This system can achieve production speeds up to 20-50 times higher than electrospinning [15, 16, 17]. However, the solution blowing system suffers from irregularities in the produced fibers. The fibers tend to intertwine and form bundles due to the turbulence created by the pressurized air, leading to an increase in pore size [18]. The electro-blowing (EB) method combines the positive aspects of both electrospinning and solution blowing in a single configuration. In this method, there are two main forces acting on the polymer jet: electrical and air drag forces [19, 20, 21, 22, 23]. Compared to electrospinning, limited research has been conducted on nanofibrous air filter mats produced using the EB method [19, 20, 21].

Adding quasi-permanent electret properties to filter mats enhances filtration efficiency without increasing ΔP. Electret properties can be imparted to filters by using electret additives or electret fibers in the media, or by methods such as corona

discharge, triboelectrification, and liquid contact charging [24]. In this context, poly (vinylidene fluoride) (PVDF) polymer was investigated as an alternative material for the production of filter mats due to its thermal, chemical, and mechanical properties, as well as its effective electret properties [25]. Among all crystal phases of PVDF, only the β phase exhibits electret properties due to its net dipole moment [26]. The high electric forces used in electrospinning and electroblowing methods align the dipole moments of PVDF and promote crystallization in the β phase [19]. In a recent study, electrospun PVDF nanofiber membrane with an average fiber diameter (AFD) of 70 nm achieved which exhibited a high PM0.3 filtration efficiency of 97.40% with a low ΔP of 51 Pa at an air velocity of 5.3 cm/s [27]. Another study investigated the performance of electrospun PVDF nanofibers with different diameters (84–525 nm) against various aerosols after applying corona discharge. Filter efficiency against 100 nm NaCl aerosols increased from 30% to 61.9% with corona charging for filters composed of 84 nm fibers [28]. Electrospun PVDF nanofiber mat with ultra-thin nanonet structures achieved a filtration efficiency of 99.999% and a ΔP of 124.2 Pa [5].

In engineering and scientific fields, experimental design and parameter optimization are of critical importance for the effective analysis and improvement of processes and systems. In this regard, statistical techniques such as "Design of Experiments" (DOE) and the "Taguchi Method" play a significant role [29]. The Taguchi Method enables the acquisition of information about the entire parameter space with a small experimental unit through a specially designed orthogonal pattern. The advantage of the method lies in its ability to analyze multiple components simultaneously and consider uncontrollable noise factors [30].

Upon examining research aimed at optimizing nanofibers through the Taguchi method, it becomes apparent that investigations have been carried out with electrospinning method on a variety of polymers, including poly(acrylamide), poly (acrylic acid), and poly (vinyl alcohol) [31], PVP [32], PVDF [33, 34]. Conversely, Akgul et. al. [35] employed the centrifugal spinning method along with Taguchi to find the optimum parameters in the production of thermoplastic polyurethane nanofibers for air filter applications. A literature search on studies related to electro-blowing and Taguchi reveals only that Saraç [36] utilized the Taguchi method to determine the process parameters for the thinnest polysulfone (PSU) nanofibers with the minimum defects, reporting the optimal conditions as 13 wt% PSU, 3 bar, and 7.5 kV. Notably, no study incorporating the combination of PVDF with electro-blowing and Taguchi has been identified in the literature.

In this study, the material and process parameters of electro-blown PVDF nanofiber filter mats were optimized using the Taguchi experimental design approach. The system parameters (electric field and air pressure), and the material parameter (solution concentration), were considered and three levels (low, moderate, high) were defined for each of parameters. Additionally, samples obtained under the optimum condition were reproduced without applying an electric field to investigate the influence of the electric field on fiber diameter and filtration characteristics. Changes in filtration performance of samples treated with corona discharge were also compared.

2 Experimental Methods

2.1 Materials

Polyvinylidene fluoride (PVDF) with a molecular weight of 477,000 g/mol (Kynar Flex 2801-00) was purchased from Arkema (France). Dimethyl sulfoxide (DMSO) of 99.8% purity (Merck), and acetone of 99.5% purity from ISOLab, were chosen as the solvents. The solutions were prepared by adding the PVDF powders into DMSO and acetone mixture (70/30 wt/wt) to obtain final polymer concentrations of 9%, 12%, and 15% by weight and mixing at a temperature of 70°C using a magnetic stirrer for a duration of 8 hours.

2.2 Nanofiber Production

Fiber production was carried out using the electro-blowing system AeroSpinner L1.0 (Areka Group Ltd.) that is schematically shown in Figure 1. Parameters used during fiber production in the EB system can be grouped into material (solution concentration, solution type, viscosity, etc.), process (air pressure, electrical field, feeding rate, collector distance, etc.), and environmental parameters (humidity, temperature).

In the experimental design, the three most important parameters (concentration, air pressure, and electrical voltage) were used as Taguchi design factors, and a three-level L9 orthogonal design was created as shown in Table 1.

Table 1: Design of experiment produced with Taguchi

Sample IDs	Solution concentration (%)	Air Pressure (bar)	Electric Voltage (kV)	AFD (nm)
1	9	1	10	209.5 $\pm$ 46.3
2	9	2	20	172.4 $\pm$ 46.2
3	9	3	30	154.7 $\pm$ 54.6
4	12	1	20	259.1 $\pm$ 63.1
5	12	2	30	217.6 $\pm$ 72.0
6	12	3	10	266.5 $\pm$ 107.2
7	15	1	30	324.3 $\pm$ 86.5
8	15	2	10	381.5 $\pm$ 74.0
9	15	3	20	368.5 $\pm$118.2

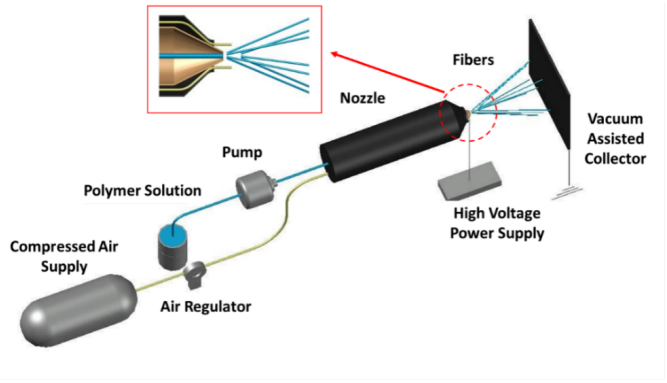

Figure 1: Schematic presentation of the electro-blowing setup

For all experiments, feeding rate, collector distance, collector rotation speed and production time were kept constant as 10 mL/h, 30 cm, 40 rpm, and 20 minutes, respectively. The produced fibers were collected onto spunbond fabrics with an average fiber diameter (AFD) of $14 \pm 2.1\ \mu m$.

2.3 Characterization

The viscosities of the PVDF solutions were measured using a rotational viscometer (Fungilab, α Series) immediately before fiber production, and they were determined as 356.5, 487.3, and 654.2 mPa·S for solution concentrations of 9, 12, and 15 wt.%, respectively. The morphological analyses of the produced fibers were conducted using a TESCAN VEGA3 Scanning Electron Microscope (SEM). SEM images were taken at 5kx magnification, and the average fiber diameters and distributions, along with standard deviation values, were calculated using 100 measurements for each sample on the Image J program.

Signal-to-noise (S/N) ratios and Analysis of Variance (ANOVA) were performed for each level of the parameter to determine the optimum parameter levels using Minitab 18 Software. In the Taguchi method, the S/N ratio can be defined with three approaches: Smaller-the-better, larger-the-better, and nominal-the-best [37]. In this study, the S/N ratio is calculated using the smaller-the-better approach with Eq 1 [38]. Here, y_i represents the value of the average fiber diameter of the ith experiment at the lower level of each factor, and n is the number of experiments conducted for this factor and level. Air permeability related to the thickness and porosity of the fibrous mat is an important factor used to determine filter performance.

$$\frac{s}{N} = -10 \log \left(\frac{1}{n} \sum_{i=1}^{n} y_i^2 \right) \tag{1}$$

Air permeability testing device (Airtest II, Prowhite) was employed in accordance with ASTM D737 standards. The test conditions encompassed a sample diameter of 38 cm^2, air pressure of 125 Pa, and an ambient temperature maintained at 22 ± 2 °C. The ΔP and filtration efficiency values of the produced samples were determined using an automated filter tester (8130A, TSI Inc.). Sodium chloride (NaCl) aerosols in the range of $0.26 \pm 0.07\ \mu m$ were generated from a NaCl solution with a wt. concentration of 2%. Filter samples with an effective area of 100 cm^2 were tested against aerosols produced at a face velocity of 15.83 cm/s. Corona charging was performed using a negative corona discharger (Chargemaster 5, Simco Ion). For corona application, the device's electrode was positioned approximately 4 cm above a rotating drum. Nanofiber samples were placed on the drum and charged for 5 minutes under a charging voltage of -20 kV while rotating at 23 rpm.

3 Results and Discussion

3.1 Fiber Morphology

The SEM images of the samples are presented in Figure 2. Accordingly, the impacts of solution concentration on both fiber production and morphology are evident. Irrespective of the other parameters, augmenting the solution concentration exhibited a favorable influence on fiber formation across all samples. The quantity of droplets within the samples (samples 1-6) diminished as the solution concentration increased, and no droplets were discernible within samples derived from a 15 wt.% solution. In addition, the increase in both the air pressure and the electric field in for the production from 9-wt. % solution also decreased the density of droplets on the mat. While the mean fiber diameters for all specimens were sub-micron, the augmentation of solution concentration yielded thicker fibers.

Samples produced using a 9 wt.% solution (1-3) manifested the thinnest fibers. The increase of air pressure and electric field induced an additional reduction in fiber diameter. The synergy of these two driving forces caused the low-viscosity solution jet to attenuate, enabling the production of fibers with diameters below 250 nm. Elevating the solution concentration from 9% to 12% yielded an increment in fiber diameter. On the other hand, the simultaneous increase of air pressure and electric field

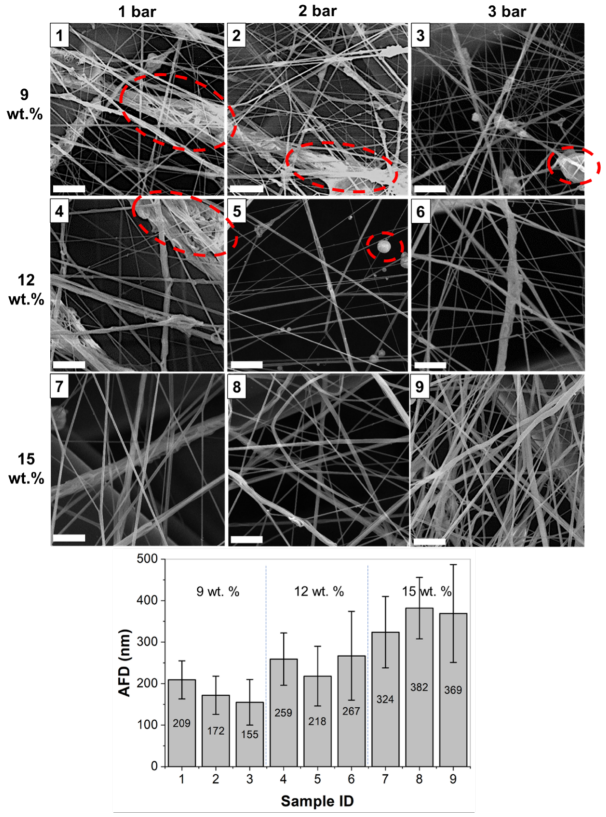

Figure 2: SEM images of the samples produced according to the Table 1 (scale bars are 5 μm) and their AFDs

decreased the mean fiber diameter from 257 nm (sample 4) to 220 nm (sample 5). In sample 6, despite application of the highest air pressure (3 bar), diminishing the electric field to 10 kV led to reduction of fiber diameter to 265 nm. Among the samples produced from the 12 wt.% solution, sample 6 produced with the lowest electric field showed the highest fiber diameter. This underscores the preeminence of the electric field in influencing fiber diameter compared to air pressure.

The coarsest fibers were derived from a 15 wt.% solution. Analogously, the increasing of air pressure coupled with the reduction of the electric field yielded thicker fibers for samples 7 and 8. This reaffirms the preeminence of the electric field over air pressure in terms of influencing fiber diameter. Conversely, in samples 8 and 9, the simultaneous escalation of both propulsive forces led to a diminution in fiber diameter.

In conclusion, lower solution concentration correlates with a reduction in average fiber diameters and a concurrent increment in droplet density. In other words, higher solution concentration results in lower droplet density, accompanied by an increment in fiber diameters. Moreover, the influence of the electric field on fiber diameters is less pronounced than that of solution concentration, yet more pronounced than air pressure.

3.2 Determination of Optimum Conditions

As the signal increases, variance is expected to decrease, making the maximization of the Signal-to-Noise (S/N) ratio the goal of the study for determining optimal parameters. The S/N ratios calculated based on the mean fiber diameters of the design factors are presented in Table 2. Here, "Level 1" corresponds to the S/N ratios of the first level of each design factor, while "Level 2" and "Level 3" correspond to the second and third levels, respectively. Additionally, delta represents the maximum difference among the S/N ratios calculated for each factor at the three levels, whereas rank signifies the efficacy value of the factors for obtaining the lowest fiber diameter. Accordingly, rank is 1 for the highest delta value, and 3 for the lowest delta value. The factor with rank 1 exerts the most significant influence on fiber diameters. In Table 2, the solution concentration of 9 wt.% yielding the maximum S/N ratios, along with 2 bar air pressure and 30 kV electric field, is recommended as the optimal condition for achieving the thinnest fiber. These conditions represent the optimal configuration for achieving the lowest fiber diameter among all possible conditions (27 experiments). This scenario can be further elucidated through analysis of variance (ANOVA).

ANOVA is utilized to examine and assess statistical differences among distinct groups, probing the determination of whether the variance between these groups arises haphazardly or possesses statistical significance. Initially, through computation of the collective between-group and within-group variances, the adjusted sum of squares (Adjusted SS) is ascertained between the groups. This Adjusted SS is divided by the degrees of freedom to yield the Adjusted MS. The F-value conveys the proportion

Table 2: S/N ratios of the design factors for "Smaller is better"

	Solution concentration (%)	Air Pressure (bar)	Electric Voltage (kV)
Level 1	-44.99	-48.26	-48.86
Level 2	-47.84	-47.72	-48.08
Level 3	-51.06	-47.90	-46.95
Delta	6.07	0.53	1.91
Rank	1	3	2

of between-group variance relative to within-group variance. Consequently, the detection of substantial differences between groups signifies the origination of these differences stem from expected causes. A high F-value indicates a significant difference between groups, while a low F-value implies the insignificance of differences between groups. On the other hand, the p-value serves to determine the import of statistical test outcomes and embodies the probability correspondent to the derived F-value. This value is employed to determine whether the observed difference is statistically significant or occurred by chance and a p-value typically less than 0.05 is considered statistically significant.

As per the ANOVA outcomes outlined in Table 3, the levels applied to polymer solution concentration exhibit statistical significance, substantiated by a p-value of 0.008. Since the largest contribution to the total Adj SS ratio (90.1%) comes from solution concentration, the concentration has been identified as the most effective parameter using the "smaller is better" approach for the average fiber diameter. On the other hand, the p-value of the electric field can be interpreted as statistically significant with a value of 0.08, while the p-value for air pressure is far from statistical significance at 0.867. Similarly, the contribution of the electric field in the total Adj SS ratio is 8.2%, while the contribution of air pressure is 0.001%. Furthermore, due to interactions among factors, the ANOVA results exhibit an error rate of 0.007%.

Considering these findings, increasing air pressure did not manifest a noteworthy impact on fiber diameter for electro-blown fibrous mats from PVDF/DMSO-Acetone solution while it caused the reduction of the droplet density. However, it is noteworthy that Yusuf et al. [39], in their experimental and modeling-based study utilizing the solution-blowing methodology, disclosed that elevating air pressure from 1 bar to 3 bar engenders a reduction in fiber diameters while further escalation from 3 bar to 6 bar resulted in thicker fiber in diameter. This underscores there is a critical threshold for air pressure within the solution-blowing method to achieve thinner fiber. Over this critical value fibers get stacked to form a bundled structure because of air turbulence. As per our study, in the EB approach, the presence of an electric field near the air drag forces implies producing additional force to attenuate the polymer jet, therefore there is no observed critical threshold for reducing fiber diameter between 1 - 3 bar. This critical threshold may occur at lower air pressures, thus, an exploration of lower air pressure levels (0.5, 1, 1.5 bar) is advisable.

Table 3: Analysis of Variance for means

Source	DF	Adj SS	Adj MS	F-Value	P-Value
Solution concentration	2	49150.9	24575.4	127.04	0.008
Air Pressure	2	59.6	29.8	0.15	0.867
Electric Voltage	2	4422.9	2211.4	11.03	0.080
Error	2	386.9	193.4		
Total	8	54020.2			

3.3 Confirmation Test

The estimated average fiber diameter $(\mathrm{AFD_{est}})$ of the fibers to be produced under the specified optimal conditions of 9 wt.% concentration, 2 bar air pressure, and 30 kV electric voltage can be calculated using the following formula (Equation 2).

$$AFD_{est} = \bar{X} + (\bar{C}1 - \bar{X}) + (\bar{P}2 - \bar{X}) + (\bar{V}3 - \bar{X}) \tag{2}$$

Here, $\overline{X}$ represents the AFD of 9 samples produced according to the Taguchi design. $(\bar{C}1)$ corresponds to the AFD of all samples produced from 9 wt.% solution (samples 1 – 3), similarly $(\bar{P}2)$ represents the AFD of samples produced with 2 bar air pressure (samples 2, 5, 8), and $(\bar{V}3)$ represents the AFD of samples produced with 30 kV electrical voltage (samples 3, 5, 7). Accordingly, the $(\mathrm{AFD_{est}})$ is calculated as 143 nm. Under these optimal conditions, sample 10 was produced and its SEM image and AFD graphs are provided in Figure 3. This sample has the smallest fiber diameter among all samples produced, with a size of 124 $\pm$ 71 nm. To observe the effect of the electric field on this sample, sample 11 was produced without an electric field. According to the SEM image in Figure 3, the absence of an electric field has increased the fiber diameter (206 $\pm$ 148 nm) and increased the droplet size in the structure (> 5 μm).

3.4 Filtration Performance

The filtration efficiency and ΔP values before and after corona treatment for all samples are presented in Figure 4. The highest filtration efficiency (91.87%) was achieved from sample 10, which was produced at the optimum parameters obtained from the ANOVA analysis and had the thinnest fiber diameter. On the other hand, the lowest filtration value (80.55%) was obtained from sample 8, which had the thickest fibers with an AFD value of 382 nm. According to the ANOVA results, solution concentration is

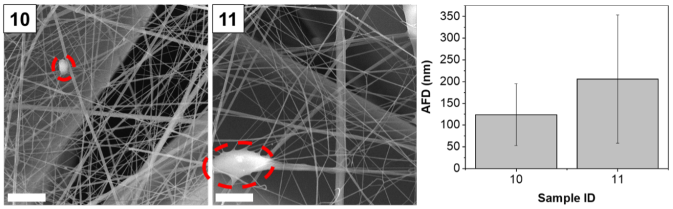

Figure 3: SEM images (scale bars are 5 μm) and AFD of samples 10 and 11

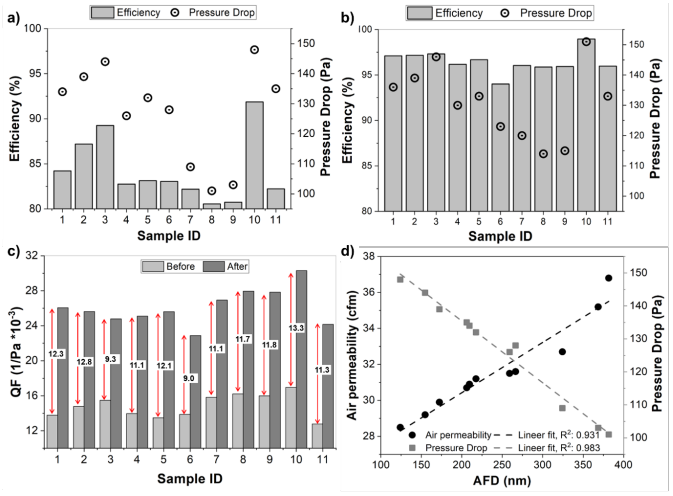

Figure 4: Filtration efficiency and ΔP of the samples a) before, b) after corona treatment. c) QF values, and d) air permeability and ΔP of the samples against AFDs

the most influential parameter on fiber diameters. This observation is similarly reflected in the filtration results. Lower solution concentration values result in finer fibers and consequently higher filtration efficiency (samples 1-3), while higher solution concentration solutions lead to thicker fibers and lower filtration efficiency (samples 7-9).

A similar trend is observed in the ΔP values, as shown in Fig. 4a. The highest and lowest ΔP values of 148 Pa and 101 Pa were obtained from the fine fibrous mat (sample 10) and thickest fibrous mat (sample 8), respectively. This is attributed to the restricted airflow due to the small pores created by fine nanofibers. When comparing samples 1 and 11, which have a similar fiber diameter, it is noted that the ΔP are nearly the same (134 and 135 Pa), but sample 1 exhibits better filtration performance because of the applied electrical voltage. This difference in filtration efficiency highlights the contribution of the electret effect demonstrated by PVDF nanofibers produced in the presence of an electrical field to the filtration mechanism. An enhancement in filtration efficiency was observed in all samples with the Corona Discharge treatment (Figure 4b). The increase in filtration efficiency is consistent with the initial performance of the samples. The highest filtration efficiency of 98.97% was achieved in the optimum sample (sample 10). After corona treatment, the lowest filtration performance increased to a value of 94.01% from 80.55%.

The quality factor (QF) values, which represent one of the most crucial parameters determining filter performance, are presented in Fig. 4c. Before corona treatment, the highest QF value (0.0170) was observed from sample 10. An inverse relationship between fiber diameter and QF values is evident. Corona treatment has notably enhanced the QF values across all samples. The most substantial enhancement, with a significant increase of 78.7%, was achieved in sample 10. This can be attributed to the heightened efficacy of the Corona Discharge treatment on sample 10 because of the finer fibrous structure that provided a higher surface area. The air permeability test results for the samples are depicted in Fig. 4d, in accordance with the AFD values. It is evidently observed that a linear relationship exists between fiber diameters and air permeability, whereby an increase in AFD corresponds to elevated air permeability values. This correlation is further reflected in the ΔP results and found similar with the other reported studies [40]. The sample with the highest air permeability also exhibited the lowest ΔP value. The calculated determination coefficients of the linear fit at 0.93 and above, signify the reliability of the explanation above.

4 Conclusion

In this study, PVDF nanofiber air filter production was optimized using novel electro-blowing technique. Based on the three-level L9 orthogonal Taguchi design, the effects of solution concentration, air pressure, and electric field on fiber diameter were systematically investigated. The significance of these parameters was also analyzed with ANOVA. According to the results,

solution concentration and applied electrical field value were found as the main factors affecting the fiber diameters. Although air pressure variations have a limited impact on diameters, they influenced droplet density, resulting in higher air pressure leading to lower droplet density. The optimum levels for the finest fiber diameter were found as 9% by weight solution concentration, 2 bar air pressure, and 30 kV electrical voltage. In addition, the corona discharge process increased the filtration performance to 98.97% in the best sample, resulting in a 78.7% improvement in the QF. This study highlights the potential of the electro-blowing method in the processing of high-efficiency PVDF nanofibers for air filtration.

Acknowledgements

This work was supported by Scientific Research Projects Coordination Unit of Istanbul Technical University (ITU BAP Grant Number MGA-2023-44749). The authors gratefully acknowledge AREKA Advanced Technology Ltd. Comp., (www.arekananofiber.com) for the electro-blowing system.

Authors' Contributions

AT conducted the experiments and fabricated the samples. All authors performed the theoretical calculations, contributed to the writing of the article, and reviewed and approved the final manuscript.

Competing Interests

The authors declare that they have no competing interests.

References

[1] A. Valavanidis, K. Fiotakis, and T. Vlachogianni. Airborne particulate matter and human health: Toxicological assessment and importance of size and composition of particles for oxidative damage and carcinogenic mechanisms. *Journal of Environmental Science and Health, Part C*, 26(4):339–362, 2008.

[2] M. He, T. Ichinose, M. Kobayashi, K. Arashidani, S. Yoshida, M. Nishikawa, H. Takano, G. Sun, and T. Shibamoto. Differences in allergic inflammatory responses between urban pm2.5 and fine particle derived from desert-dust in murine lungs. *Toxicology and Applied Pharmacology*, 297:41–55, 2016.

[3] R. Zhang, C. Liu, P. Hsu, C. Zhang, N. Liu, J. Zhang, H. R. Lee, Y. Lu, Y. Qiu, S. Chu, and Y. Cui. Nanofiber air filters with high-temperature stability for efficient pm2.5 removal from the pollution sources. *Nano Letters*, 16(6):3642–3649, 2016.

[4] J. Liu, D. Y. H. Pui, and J. Wang. Removal of airborne nanoparticles by membrane coated filters. *Science of The Total Environment*, 409(22):4868–4874, 2011.

[5] Z. Li, W. Kang, H. Zhao, M. Hu, J. Ju, N. Deng, and B. Cheng. Fabrication of polyvinylidene fluoride tree-like nanofiber web for ultra high performance air filtration. *Material Design*, 92:95–101, 2016.

[6] J. L. Davis, H. J. Walls, L. Han, T. A. Walker, J. A. Tufts, A. Andrady, and D. Ensor. Use of nanofibers in high-efficiency solid-state lighting. In *Seventh International Conference on Solid State Lighting*, pages 248–256. SPIE, 2007.

[7] A. Kilic, S. Selcuk, A. Toptas, and A. Seyhan. *Nonelectro nanofiber spinning techniques*, chapter 10, pages 267–293. Elsevier, 2023.

[8] M. Aliabadi. Effect of electrospinning parameters on the air filtration performance using electrospun polyamide-6 nanofibers. *Chemical Industry and Chemical Engineering Quarterly*, 23(4):441–446, 2017.

[9] P.-Y. Chen and S.-H. Tung. One-step electrospinning to produce nonsolvent-induced macroporous fibers with ultrahigh oil adsorption capability. *Macromolecules*, 50(6):2528–2534, 2017.

[10] X. Ding, Y. Li, Y. Si, X. Yin, J. Yu, and B. Ding. Electrospun polyvinylidene fluoride/sio2 nanofibrous membranes with enhanced electret property for efficient air filtration. *Composites Communications*, 13:57–62, 2019.

[11] T. Tanski, P. Jarka, and W. Matysiak. *Electrospinning Method Used to Create Functional Nanocomposites Films*. InTech, 2018. . URL `http://dx.doi.org/10.5772/intechopen.70984`.

[12] M. Ekrem. Mechanical properties of mwcnt reinforced polyvinyl alcohol nanofiber mats by electrospinnig method. *El-Cezeri*, 4(2), 2017.

[13] M. Xia, Q. Liu, Z. Zhou, Y. Tao, M. F. Li, K. Liu, Z. Wu, and D. Wang. A novel hierarchically structured and highly hydrophilic poly(vinyl alcohol-co-ethylene)/poly(ethylene terephthalate) nanoporous membrane for lithium-ion battery separator. *Journal of Power Sources*, 266:29–35, 2014.

[14] Y. Polat, E. S. Pampal, E. Stojanovska, R. Simsek, A. Hassanin, A. Kilic, A. Demir, and S. Yilmaz. Solution blowing of thermoplastic polyurethane nanofibers: A facile method to produce flexible porous materials. *Journal of Applied Polymer Science*, 133(9), 2016.

[15] H. Lou, W. Han, and X. Wang. Numerical study on the solution blowing annular jet and its correlation with fiber morphology. *Industrial & Engineering Chemistry Research*, 53(7):2830–2838, 2014.

[16] M. Gungor, S. Selcuk, A. Toptas, and A. Kilic. Aerosol filtration performance of solution blown pa6 webs with bimodal fiber distribution. *ACS Omega*, 7(50):46602–46612, 2022.
[17] M. Gungor, M. D. Calişir, and A. Kilic. Solution-blown pa6- and pvdf-based nanofibrous composite mats for aerosol filtration. *Fibers and Polymers*, 24(5):1603–1612, 2023.
[18] L. Shi, X. Zhuang, X. Tao, B. Cheng, and W. Kang. Solution blowing nylon 6 nanofiber mats for air filtration. *Fibers and Polymers*, 14(9):1485–1490, 2013.
[19] A. Al Rai, E. Stojanovska, G. Fidan, E. Yetgin, Y. Polat, A. Kilic, A. Demir, and S. Yilmaz. Structure and performance of electroblown pvdf-based nanofibrous electret filters. *Polymer Engineering and Science*, 60(6):1186–1193, 2020.
[20] A. Eticha, A. Toptaş, Y. Akgül, and A. Kilic. Electrically assisted solution blow spinning of pvdf/tpu nanofibrous mats for air filtration applications. *Turkish Journal of Chemistry*, 47(1):47–53, 2023.
[21] M. Gungor, A. Toptas, M. D. Calisir, and A. Kilic. Aerosol filtration performance of nanofibrous mats produced via electrically assisted industrial-scale solution blowing. *Polymer Engineering and Science*, 61(10):2557–2566, 2021.
[22] L. Cao, Q. Liu, J. Ren, W. Chen, Y. Pei, D. L. Kaplan, and S. Ling. Electro-blown spun silk/graphene nanoionotronic skin for multifunctional fire protection and alarm. *Advanced Materials*, 33(38):2102500, 2021.
[23] Y. Liu, C. Jia, H. Zhang, H. Wang, P. Li, L. Jia, F. Wang, P. Zhu, H. Wang, L. Yu, F. Wang, L. Wang, X. Zhang, Y. Sun, and B. Li. Free-standing ultrafine nanofiber papers with high pm0.3 mechanical filtration efficiency by scalable blow and electro-blow spinning. *ACS Applied Materials and Interfaces*, 13(29):34773–34781, 2021.
[24] A. Kilic, S. Russell, E. Shim, and B. Pourdeyhimi. *The charging and stability of electret filters*, chapter 4, pages 95–121. Woodhead Publishing Series in Textiles. Woodhead Publishing, 2017.
[25] D. Lolla, M. Lolla, A. Abutaleb, H. U. Shin, D. H. Reneker, and G. G. Chase. Fabrication, polarization of electrospun polyvinylidene fluoride electret fibers and effect on capturing nanoscale solid aerosols. *Materials*, 9(8), 2016.
[26] A. J. Lovinger. Ferroelectric polymers. *Science*, 220(4602):1115–1121, 1983.
[27] T. T. Bui, M. K. Shin, S. Y. Jee, D. X. Long, J. Hong, and M. G. Kim. Ferroelectric pvdf nanofiber membrane for high-efficiency pm0.3 air filtration with low air flow resistance. *Colloids and Surfaces A: Physicochemical and Engineering Aspects*, 640:128418, 2022.
[28] W. W. F. Leung and Q. Sun. Electrostatic charged nanofiber filter for filtering airborne novel coronavirus (covid-19) and nano-aerosols. *Separation and Purification Technology*, 250:116886, 2020.
[29] H. M. Khanlou, B. C. Ang, S. Talebian, A. M. Afifi, and A. Andriyana. Electrospinning of polymethyl methacrylate nanofibers: optimization of processing parameters using the taguchi design of experiments. *Textile Research Journal*, 85 (4):356–368, 2015.
[30] J. Stufken and G. S. Peace. Taguchi methods: A hands-on approach. *Technometrics*, 36(1):121, 1994.
[31] T. S. Sorkhabi, M. F. Samberan, K. A. Ostrowski, P. Zajdel, A. Stempkowska, and T. Gawenda. Electrospinning of poly (acrylamide), poly (acrylic acid) and poly (vinyl alcohol) nanofibers: Characterization and optimization study on the effect of different parameters on mean diameter using taguchi design of experiment method. *Materials*, 15(17), 2022.
[32] A. Pinarbasi and F. C. Callioglu. Electrospinning of pvp nanofibers and optimization with taguchi experimental design. *Süleyman Demirel University Faculty of Arts and Science Journal of Science*, 17(2), 2022.
[33] A. Tariq, A. H. Behravesh, Utkarsh, and G. Rizvi. Statistical modeling and optimization of electrospinning for improved morphology and enhanced β-phase in polyvinylidene fluoride nanofibers. *Polymers*, 15(22), 2023.
[34] S. Gee, B. Johnson, and A. L. Smith. Optimizing electrospinning parameters for piezoelectric pvdf nanofiber membranes. *Journal of Membrane Science*, 563:804–812, 2018.
[35] N. A. S. Gundogdu, Y. Akgul, and A. Kilic. Optimization of centrifugally spun thermoplastic polyurethane nanofibers for air filtration applications. *Aerosol Science and Technology*, 52(5):515–523, 2018.
[36] Z. Sarac, A. Kilic, and C. Tasdelen-Yucedag. Optimization of electro-blown polysulfone nanofiber mats for air filtration applications. *Polymer Engineering and Science*, 63(3):723–737, 2023.
[37] H. Oktem, T. Erzurumlu, and I. Uzman. Application of taguchi optimization technique in determining plastic injection molding process parameters for a thin-shell part. *Materials and Design*, 28(4):1271–1278, 2007.
[38] H.-L. Lin and C.-P. Chou. Optimization of the gta welding process using combination of the taguchi method and a neural-genetic approach. *Materials and Manufacturing Processes*, 25(7):631–636, 2010.
[39] Y. Polat, M. Yangaz, M. D. Calisir, M. Z. Gül, A. Demir, B. Ekici, and A. Kilic. Çözeltiden üfleme ile nanolif üretim yönteminde hava basıncının nanolif üretimine etkisi. *Journal of the Faculty of Engineering and Architecture of Gazi University*, 35(4), 2020.
[40] A. Toptaş, M. D. Çalışır, and A. Kılıç. Production of ultrafine pvdf nanofiber-/nanonet-based air filters via the electroblowing technique by employing peg as a pore-forming agent. *ACS Omega*, 2023.

El Cezeri
Journal of Science and Engineering
ISSN: 2148-3736

Research Article

Synthesis and Characterization of Carbon Papers

Yakup Kaan Yanılmaz[1a]
[1] Green Hope High School, North Carolina
yyanilmaz@students.wcpss.net

DOI : 10.31202/ecjse.1415880
Received: 07.01.2024 Accepted: 26.02.2024
How to cite this article:
Yakup Kaan Yanılmaz,“ Synthesis and Characterization of Carbon Papers", El-Cezeri Journal of Science and Engineering, Vol: 11, Iss:2, (2024), pp.(207-211).
ORCID: [a]0009-0001-7620-614X;

Abstract : Porous carbons are promising for various applications from sensors to CO2 capture. This work aims to report a facile approach to synthesizing porous carbons by using cheap and sustainable materials. Porous carbons are also treated to tune the chemical and physical structure. SEM images, FTIR spectra, Raman spectra, and XRD patterns are examined to characterize the porous carbons. The treated carbon fibers showed a highly disordered structure with a large interlayer spacing. Results show that porous carbons could be applicable for different applications.

Keywords : Carbons, Filter, Structure, Characterization

1 Introduction

With the development of the technology, material scientists explore new materials for the emerging fields. Carbon materials have been widely investigated owing to their advantages. A large surface area, high robustness, high and tunable porosity, high electrical conductivity, exceptional flexibility, and easy recyclability have made carbon materials promising for many applications [1, 2, 3]. Cai et al. [2] used carbon fiber-based cloth for water decontamination and reported effective purification. Cheng et al. [4] reported efficient oxygen electrocatalysis by using carbon fibers. Shi et al. [5] reported high-performance supercapacitor electrodes by using carbon cloth. Ma et al. [6] synthesized porous carbon fibers and porous carbons with fibrous structures and showed promising results in CO_2 capture. Li et al. [7] designed a carbon-based electrochemical sensor. Yang et al. [8] prepared carbon biosensors.

Heteroatom doping including nitrogen doping is an effective strategy to increase the properties of carbon materials. Many studies reported enhanced performance after doping for various applications including but not limited to supercapacitors, adsorbents, batteries, and electrocatalysis. Nitrogen doping could tailor their electron-donor properties and provide extra active sites for pseudocapacitive interaction, thus improving supercapacitors' capacitance. Moreover, doping also changes the crystal structure and thus electrical conductivity [6, 9, 10, 11, 12]. Very few studies reported N-doped carbons by using melamine. Ozturk et al used carbon black and melamine to synthesize N-doped carbons and investigated the effect of N doping at different temperatures [13]. Tjandra et al. used graphene oxide and melamine foam [14].

Considering global warming and climate change, reducing the usage of petroleum-based materials is crucial. Moreover, there is a huge demand for low-cost and sustainable precursors for carbon materials [15, 16]. Many biomass has been used as a carbon source however cellulose is one of the most abundant in the earth [17]. In this study, cellulose paper was used as a carbon source, and free-standing carbon paper was synthesized via calcination. Melamine was used as a nitrogen source and the as-prepared carbon paper was characterized by using SEM, FTIR, XRD, and Raman spectroscopy.

2 Experimental Methods

Cellulose filter paper was used as a carbon precursor. Melamine was purchased from Merck and used as a nitrogen source. Calcination was applied in the nitrogen atmosphere at 800 ^{o}C for 2 h. Melamine was dissolved in water and applied to cellulose filter papers to tune the chemical composition as well. The free-standing carbon papers were obtained after calcination and several structural characterization techniques were used to study the porous carbon materials.

Scanning electron microscopy with EDX equipment was used to study the morphology and elemental composition of the prepared samples. Fourier transform infrared spectroscopy, Raman spectroscopy, and XRD analysis were also employed to study the chemical composition of the samples.

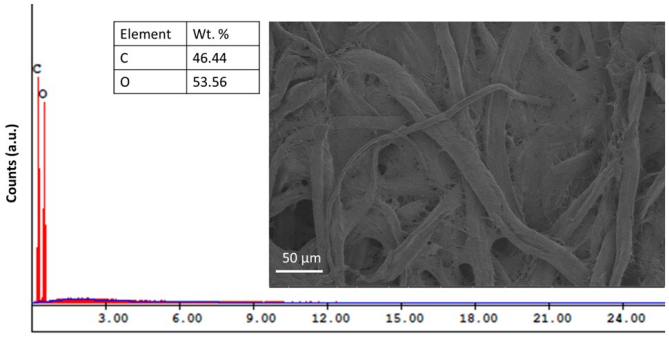

Figure 1: SEM image of the filter paper with the EDX spectra

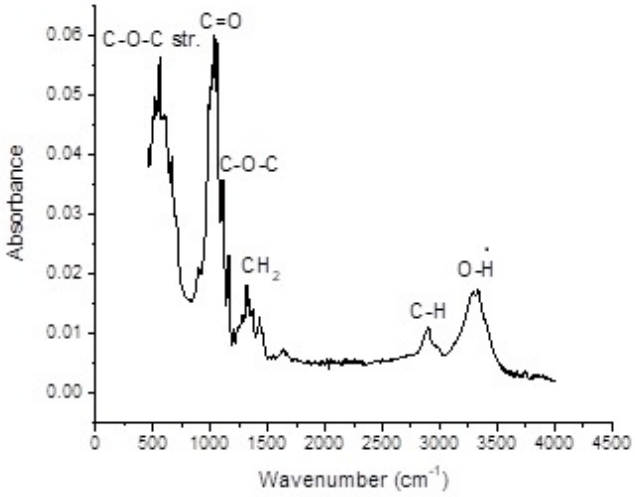

Figure 2: FTIR spectrum of the filter paper

3 Results and Discussion

Figure 1 shows the SEM image of the filter paper with the EDX spectra. A highly fibrous structure is observed which is beneficial for many applications including filtration and sensors. EDX spectra also confirm the chemical structure of cellulose.

FTIR spectrum of the filter paper is shown in Figure 2. A broad peak between 3500 and 3200 cm^{-1} corresponds to stretching vibrations of O-H presented in cellulose. The peaks approximately at 2900 and 1020 cm^{-1} are attributed to C-H and C-O stretching, respectively. The peak around 1730 cm^{-1} corresponds to C=O stretching vibrations. The peak at 1312 cm^{-1} corresponds to C-H_2 rocking vibration while the peak at 1158 cm^{-1} is ascribed to the C-O-C asymmetric valence vibration. The peak approximately at 660 cm^{-1} is attributed to C-O-C stretching related to glycosidic linkage between glucose units in cellulose [15, 18].

After successfully characterizing the structure of the cellulose filter paper, the calcination was applied to synthesize carbon paper. Figure 3 displays the SEM images of carbon paper and melamine-treated carbon papers. The fibrous structure is preserved after calcination at high temperatures and a highly porous structure was observed. Conductive and porous carbon structures are promising for sensors, supercapacitors, and filters [5, 19]. High porosity leads to rapid mass transport of species, a larger amount of electrolyte infiltration of electrolyte onto the electrode, proper electrode-electrolyte interfaces, large surface area, many active catalytic sites, continuous electron transport pathways, shorter distances for mass and ion transport, many available active surfaces, and free spaces to accommodate changes in volume [17].

The SEM image of melamine-treated carbon paper was also seen in Figure 3. Melamine treatment did not change the morphology significantly. Moreover, EDX spectra reveal that melamine-treated carbon papers have nitrogen atoms in the structure. Nitrogen in the carbon structures improves the physical and chemical properties and thus improves the performance for many applications [20].

Figure 4 shows the FTIR spectra of the carbon and treated carbon papers. The peak at around 1600 cm^{-1} corresponds to the C=C/N=C stretching vibration indicating the presence of a sp^2 hybridized honeycomb lattice, and the peak at around 1446 cm^{-1} is ascribed to the characteristic C-N stretching vibrations [21]. The results indicate that nitrogen-containing functional groups are introduced efficiently which is proved by EDX spectra, Raman analysis, and XRD pattern as well.

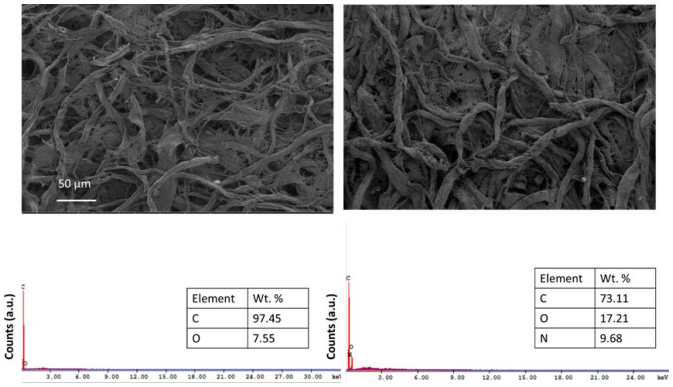

Figure 3: SEM images of the carbon paper and the treated carbon paper with the EDX spectra

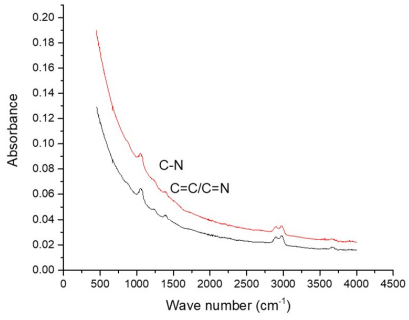

Figure 4: FTIR spectra of the carbon paper and the treated carbon paper

Raman spectra of the carbon and treated carbon are seen in Figure 5. Two peaks of D band (1366 cm^{-1}) and G band (1610 cm^{-1}) suggest that carbon paper and treated carbon paper are graphitic dominating material with disordered structure. The intensity ratio of D and G bands (I_D/I_G) is used to evaluate the degree of the disorder [10]. The intensity ratio of the D and G bands is calculated to be 0.8 and 1.0, respectively, for the carbon and treated carbon papers, indicating that melamine treatment increased the degree of disorder which is beneficial for many applications. Increased disorder level was also reported as a result of N doping by Chen et al. [22]. The increase in intensity of the D band could be ascribed to the increase of surface defects [23, 24] as a result of melamine treatment which is consistent with the EDX spectra of the treated carbon paper.

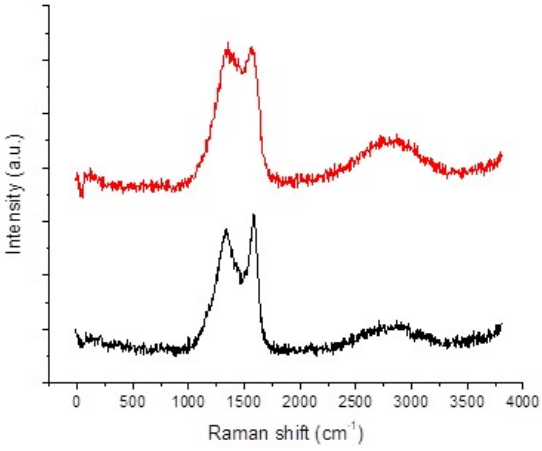

Figure 5: XRD pattern of the carbon paper and the treated carbon paper

4 Conclusion

In summary, porous carbons were synthesized by using calcination and melamine treatment. The prepared materials were characterized by using SEM, Raman spectroscopy, XRD, and FTIR analysis. The effect of the treatment on the chemical structure was shown. The degree of disorder increased after the treatment. This study shows that the chemical structure and physical properties of carbons could be easily tuned via simple and low-cost treatment to improve performance for specific applications.

Competing of Interest

The authors declare that they have no competing interests.

References

[1] M. Ayçiçek, N. Ayçiçek, N. Özsoy, M. Özsoy, and A. Akinci. Comparison of tribological behaviours of nano sio2 and zro2 reinforced polyester matrix composite materials. *El-Cezeri Journal of Science and Engineering*, 10:464–474, 2023.

[2] M. Cai, Y. Liu, K. Dong, X. Chen, and S. Li. Floatable s-scheme bi2wo6/c3n4/carbon fiber cloth composite photocatalyst for efficient water decontamination. *Chinese Journal of Catalysis*, 52:239–251, 2023.

[3] G. Jia, Y. Yu, X. Wang, C. Jia, Z. Hu, S. Yu, H. Xiang, and M. Zhu. Highly conductive and porous lignin-derived carbon fibers. *Materials Horizons*, 10:5847–5858, 2023.

[4] W. Cheng, X. F. Lu, D. Luan, and X. W. Lou. Nimn-based bimetal–organic framework nanosheets supported on multi-channel carbon fibers for efficient oxygen electrocatalysis. *Angewandte Chemie International Edition*, 59:18234–18239, 2020.

[5] L. Shi, J. Ye, H. Lu, G. Wang, J. Lv, and G. Ning. Flexible all-solid-state supercapacitors based on boron and nitrogen-doped carbon network anchored on carbon fiber cloth. *Chemical Engineering Journal*, 410:128365, 2021.

[6] C. Ma, J. Bai, X. Hu, Z. Jiang, and L. Wang. Nitrogen-doped porous carbons from polyacrylonitrile fiber as effective co2 adsorbents. *Journal of Environmental Sciences*, 125:533–543, 2023.

[7] L. Li, D. Liu, K. Wang, H. Mao, and T. You. Quantitative detection of nitrite with n-doped graphene quantum dots decorated n-doped carbon nanofibers composite-based electrochemical sensor. *Sensors and Actuators B: Chemical*, 252: 17–23, 2017.

[8] R. Yang, X. Yan, Y. Li, X. Zhang, and J. Chen. Nitrogen-doped porous carbon-zno nanopolyhedra derived from zif-8: new materials for photoelectrochemical biosensors. *ACS Applied Materials & Interfaces*, 9(49):42482–42491, 2017.

[9] G. Ni, F. Qin, Z. Guo, J. Wang, and W. Shen. Nitrogen-doped asphaltene-based porous carbon fibers as supercapacitor electrode material with high specific capacitance. *Electrochimica Acta*, 330:135270, 2020.

[10] Y. Yang, Y.-X. Liu, Y. Li, B.-W. Deng, B. Yin, and M.-B. Yang. Design of compressible and elastic n-doped porous carbon nanofiber aerogels as binder-free supercapacitor electrodes. *Journal of Materials Chemistry A*, 8:17257–17265, 2020.

[11] F. Liu, J. Meng, F. Xia, Z. Liu, H. Peng, C. Sun, L. Xu, G. Van Tendeloo, L. Mai, and J. Wu. Origin of the extra capacity in nitrogen-doped porous carbon nanofibers for high-performance potassium ion batteries. *Journal of Materials Chemistry A*, 8:18079–18086, 2020.

[12] Z.-Y. Wang, S.-D. Jiang, C.-Q. Duan, D. Wang, S.-H. Luo, and Y.-G. Liu. In situ synthesis of co 3 o 4 nanoparticles confined in 3d nitrogen-doped porous carbon as an efficient bifunctional oxygen electrocatalyst. *Rare Metals*, 39:1383–1394, 2020.

[13] A. Öztürk and A.B. Yurtcan. Preparation and characterization of melamine-led nitrogen-doped carbon blacks at different pyrolysis temperatures. *Journal of Solid State Chemistry*, 296:121972, 2021.

[14] R. Tjandra, R.W. Liu, L. Lim, and A. Yu. Melamine based, n-doped carbon/reduced graphene oxide composite foam for li-ion hybrid supercapacitors. *Carbon*, 129:152–158, 2018.

[15] T. Kumar, M. Chandrasekar, K. Senthilkumar, R. Ilyas, S. Sapuan, N. Hariram, A.V. Rajulu, N. Rajini, and S. Siengchin. Characterization, thermal and antimicrobial properties of hybrid cellulose nanocomposite films with in-situ generated copper nanoparticles in tamarindus indica nut powder. *Journal of Polymers and the Environment*, 29:1134–1142, 2021.

[16] S. Sun, Y. Xu, J.-L. Wen, T.-Q. Yuan, and R.-C. Sun. Recent advances in lignin-based carbon fibers (lcfs): precursors, fabrications, properties, and applications. *Green Chemistry*, 24:5709–5738, 2022.

[17] S.S. Sekhon and J.-S. Park. Biomass-derived n-doped porous carbon nanosheets for energy technologies. *Chemical Engineering Journal*, 425:129017, 2021.

[18] D. Das, P. Prakash, P.K. Rout, and S. Bhaladhare. Synthesis and characterization of superabsorbent cellulose-based hydrogel for agriculture application. *Starch-Stärke*, 73:1900284, 2021.

[19] C. Chen, J. Guan, N.W. Li, Y. Lu, D. Luan, C.H. Zhang, G. Cheng, L. Yu, and X.W. Lou. Lotus-root-like carbon fibers embedded with ni–co nanoparticles for dendrite-free lithium metal anodes. *Advanced Materials*, 33:2100608, 2021.

[20] J. Liu, S. Muhammad, Z. Wei, J. Zhu, and X. Duan. Hierarchical n-doping germanium/carbon nanofibers as anode for high-performance lithium-ion and sodium-ion batteries. *Nanotechnology*, 31:015402, 2019.

[21] D. He, L. Wu, Y. Yao, J. Zhang, Z.-H. Huang, and M.-X. Wang. A facile route to high nitrogen-containing porous carbon fiber sheets from biomass-flax for high-performance flexible supercapacitors. *Applied Surface Science*, 507:145108, 2020.
[22] L. Chen, Z. Wen, L. Chen, W. Wang, Q. Ai, G. Hou, Y. Li, J. Lou, and L. Ci. Nitrogen and sulfur co-doped porous carbon fibers film for flexible symmetric all-solid-state supercapacitors. *Carbon*, 158:456–464, 2020.
[23] T.P. Mofokeng, Z.N. Tetana, and K.I. Ozoemena. Defective 3d nitrogen-doped carbon nanotube-carbon fibre networks for high-performance supercapacitor: Transformative role of nitrogen-doping from surface-confined to diffusive kinetics. *Carbon*, 169:312–326, 2020.
[24] Y. Zhao, G. Luo, L. Zhang, L. Gao, D. Zhang, and Z. Fan. Nitrogen-doped porous carbon tubes composites derived from metal-organic framework for highly efficient capacitive deionization. *Electrochimica Acta*, 331:135420, 2020.